Evaluation of wide-area landslide hazard using depth-integrated particle method and GIS

March 2016

ALESSANDRA MAYUMI NAKATA

Evaluation of wide-area landslide hazard using depth-integrated particle method and GIS

Graduate School of Systems and Information Engineering

University of Tsukuba

March 2016

ALESSANDRA MAYUMI NAKATA

ABSTRACT

Over the past decades, there has been a dramatic increase in deadly landslides. According to Brabb (1993), around 90% of losses suffered by landslides can be avoided if the problem is recognized before the event. Therefore, improving the evaluation of landslide risk is an important issue for the entire world (e.g. Pastor et al, 2014). Landslides caused by heavy rain have been the worst natural disaster in Brazil. To mitigate losses, a landslide simulation has been studied to be possible to predict its occurrence (Hoang et al., 2009, Nakata et al., 2012, Zhang et al, 2013). This research aims to predict landslides damage area in a wide region using a depth-integrated particle method. The start point is the generation of a stereoscopic image (depth illusion generated from two images taken from slightly different angles) through images acquired by ALOS satellite.

We simplified the SPH method (Lucy; Gingold; Monaghan, 1977) considering a pair-wise interaction between the macro computational particles and optimal material parameters for the whole area. Also, we limited the number of material parameters as small as possible, which are density of the soil ρ, Manning coefficient n, critical slope of deposition $i_d$and the initial critical slope angle for failure i_f. According to this interaction, gravitational force and the bottom shear force controlled by the Manning coefficient and the critical slope inclination, a group of particles flow down a steep slope and are deposited in a plain field. Therefore, it is necessary to assess not only the slope failure hazard, but also the affected area due to soil mass flowage.

One of the most difficult in predicting the occurrences of landslides lies in the variation of the composition of the soil. It is well known that the geo-materials are very heterogeneous and their properties differ in different places. One of the purposes of this study is to try to identify the optimal material parameters by using a numerical simulation. By analyzing the entire region of interest with various parameters and comparing the case histories, we can construct the optimal material parameter model in the region. This kind of analysis concedes us to detect which phenomenon are susceptible to be a reflection of the behavior of the parameters and so on.

The accuracy of the simulation plays an important deal to validate the proposed method. To do so, a statistical analysis of the proposed method was conducted by comparing the damaged area with the simulated results. The simulation's accuracy was characterized by the ratio of overlapped area to the union of the two areas. We found the scheme is 35.62% effective in predicting the damage area. This analysis was handled to a real case happened in 2011, Nova Friburgo in the state of Rio de Janeiro, Brazil. The parameters that best suits the region of Nova Friburgo are 32 (deg), 0 (deg) and 0.1 for i_f, i_d and n, respectively. The critical slope for failure corresponds to 0.56m of the groundwater table height for the most fragile soil (i.e. slope colluvium).

Hofu city, located in Yamaguchi Prefecture, Japan, was also chosen as a case study. However, the accuracy found was 31.72% for the prediction of landslides. The recommended parameters for use in Hofu city are 24 (deg), 0 (deg) and 0.04 for i_f, i_d and n, respectively. The difference between the accuracy found in Nova Friburgo's case study and Hofu's case study can be explained by the weathering and seismic waves that are particular characteristics of the Japanese territory. Earthquakes may change the characteristics of the soil which can be felt in the reduction of friction and cohesion (Hack et al, 2007). Also can be explained by the difference between the two areas chosen as a case study in Hofu city: area No.1 is formed by Granite (Gr) that proved to be more fragile, causing a greater number of small landslides. Area No. 2 is steeper than Area No. 1, plus is formed by Granodiorite (Gd) that had smaller number of landslides, however, the size was larger. Taking into consideration these inequalities and performing both areas separately we got 45.12% of accuracy for flow simulation for i_f=20 (deg) (represents 1.8 m of the groundwater table height) in Area No. 1 and 24.72% for i_f=30 (deg) (indicates 1.65 m of the groundwater table height) in Area No.2. Therefore, the average between the two areas turns to 34.92%.

In certain occasions, the key performance chosen to evaluate the efficiency of the flow simulation a_c needed a complementary analysis. Therefore, we define another key performance, called damage area ratio, which is defined as the damaged area divided by the total area. According to this new index, simulations with i_f<25 (deg) over-estimate the damage

area, while simulations with i_f>30 (deg) under-estimate the damage area in Hofu - Area No. 1. The same analysis was performed in Hofu - Area No. 2. Under the results obtained, simulations with i_f>20 (deg) over-estimate the damage area. It turns out a tendency that the simulation over-estimates the damage, especially in low-damaged areas. The Nova Friburgo's satellite image suffered with some influence of clouds, shadows and old landslide scars that interfered in the results of the simulation of landslides; therefore the analysis of the damage area ratio may carry to erroneous conclusion and will not be explored here.

A grid size study approach was used to allow a deeper insight into its effect on the simulation. The correlation between increases in the velocity of the flow associated with the increase of the grid size was reported. This result further support the idea of a grid with a bigger size has a lower detailed topography, which implying a minor disturbance of the flow. Moreover, the size of particles is set to equal the DEM grid size, which means the greater the grid size, the greater the particles size will be, however, with smaller number of particles to interact, which can reduce the shear stress in the bottom. The accuracy of the flow simulation was also affected by the grid size study: grids with larger size dispense the details in the topography. In some cases, it is essential to consider all topographic information to have a landslide simulation close to the real situation.

To validate the proposed method, a flow simulation was performed according to the equation of motion in a one-dimensional slope named V-shape first proposed by Zhang et. al (2015).

It is apparent from this study that very few parameters resulted in a landslide simulation with a reasonable accuracy. Also, none of these values was needed to obtain by in-situ tests. Our methodology allowed us to investigate the sensibility of those parameters by using a numerical simulation. The simulation proved to me more sensitive to Manning coefficient n, whereas it showed no significant variation to $i_d < 5$.

Key words: flow-like landslide, depth-integrated particle method, smoothed particle hydrodynamics, wide area, accuracy of the flow simulation, grid size.

ACKNOLEDGMENT

I would like to express my deepest admiration and gratitude to my supervisor Professor Takashi Matsushima for giving me a wonderful guideline for assignment throughout consultations with plenty didactic and patience. I have been extremely lucky to have a supervisor who cares about not only my work, but also my quality of life in Japan. I also would like to thank you Professor Yasuo Yamada and Assistant Professor Kyosuke Yamamoto for the all encouragement words and advices during my journey in the Geotechnical Engineering Laboratory. In addition, a thank you to my committee members, Associate Professor Gaku Shoji from the Research group on earthquake and Tsunami engineering for lifeline system resiliency of University of Tsukuba, and Assistant Professor Tsuyoshi Hattanji from the Department of Faculty of life and Environmental Sciences of University of Tsukuba, whose advices were deeply appreciated and used in this research. I would also like to show my gratitude to Mr. Hattanji for sharing important information and data from Yamaguchi Prefecture that valuable contributed in this study (Chapter 5).

Furthermore I would like to acknowledge with much appreciation the students from Geotechnical Engineering Laboratory who have extended me a hand when I needed. Since 2010, the year that I started as a researcher, I have met wonderful people that I would like to express my gratitude. All of them contributed strongly to make easy my life in Japan. I am indebted to them for their help.

A very special thanks goes to my lovely ones in Brazil and Japan, who have supported me throughout the entire process, both by keeping me balanced and helping me placing parts together. I thank my parents, Koji and Akemi, for their sacrifices to ensure that my sisters and I had an excellent education. For this and for their always support, I dedicate this dissertation for my parents. Also, I must express my gratitude to my husband, Jun, for his daily encouragement and continuous support during this process.

Last but not least, I also want to thank to Nippon Foundation for their financial support granted through this research and Kaigai Nikkeijin Kyoukai for their assistance.

SUMMARY

LIST OF FIGURES

LIST OF TABLES

1. INTRODUCTION

1.1. Research Background

Landslides are in only one category of the so-called “mass movements”: this process involves the detachment and transportation of soil and/or rock material. Landslides, as well as other mass movements, are part of the natural dynamics of transportation and formation of Earth’s crust and also related to natural phenomena such as gravity and climatic variation.

Landslides can be triggered by natural phenomena, such as rain, and/or human actions, such as an irregular occupation. In both cases, the landslide rupture mechanism is the same: when driving forces overcome resisting forces. The driving forces (shear stress) are influenced by slope angles, gravity, climate, saturation of the soil and soil type. Opposing the mentioned forces are the resisting forces (shear strength) that are affected by the cohesion and internal friction.

The steeper the slope is, the greater is the possibility to occur landslides, however other factors are also important and need to be considered. In tropical climates, like in Brazil, the precipitation rate is generally high which causes the soil to become soggy and facilitating the mass movements. At this point the presence of vegetation is critical because it reduces the impact of rain on the ground avoiding compression and some types of plants have root system that improves soil aggregation. Another important factor is the chemical weathering that causes changes in the composition of soil or rock materials because of the complex reactions with oxygen, water and other substances.

We would like to emphasize the influence of the rain precipitation in the landslides triggering. When it rains, the water from the rain infiltrates into the soil taking the air space in the pore space. Merely this replacement changes the weight of the soil, since the weight of water is greater than the weight of air. Other reason is that the water changes the angle of repose. Therefore, when the soil is saturated the angle of repose decrease to small amounts and the soil acquires physical characteristics as a fluid. From the previous concept, it is important several studies related to the landslides caused by rain. Furthermore, due to climate change,

the number of landslides is increasing year by year. Experts predicted it10 years ago during a conference in Tokyo (UNU, 2005). It is necessary to emphasize not only the causes but mainly the consequences.

It turns out that when these movements happen in places where there is human settlement, the consequences can be disastrous. On a sliding situation, entire houses, roads and everything that it is in their way can be taken downhill or end up buried.

In 2008, in the State of Santa Catarina (Brazil) an event of landslides killed around 130 people and displaced other 80,000 (Brooks, 2010). Hofu city suffered with an intensive rainfall on July 2009, causing destructive debris flow. Although, Japan has an efficient warning system, 6 people died under the mass of soil (BBC, 2009). It was during the New Year celebration on January 1st 2010 that heavy rain triggered mudslides on Ilha Grande, near Rio de Janeiro (Brazil). The number of people buried reached 26 (BBC, 2010). The state of Rio de Janeiro has accumulated 907 deaths related to the landslide's disaster during the summer season on 2011 (OGLOBO, 2011).

A recently case, what they called a "Mega-Landslide" happened in California on October 2015. It was triggered by thunderstorms and buried a hundreds of cars. Other massive landslide took place in Guatemala on October 2015, where 271 people died and dozen still missing (USGS, 2015)

This sort of natural disaster generally starts from the top of the slope carrying everything in its path; the fluidized soil-water mixture sometimes travels over several kilometers down and attacks the downstream residential area. Therefore, it is essential to evaluate not only slope failure risk but also the affected area due to soil mass flowage. Indirect impact on society includes loss of property value, lifeline systems that can be destroyed or damaged and so on. Direct impact, and most important one, causes high mortality and injuries. Actions to mitigate these impacts are a concern worldwide. According to Brabb (1993), around 90% of losses suffered by landslides can be avoided, if the problem is recognized before the event.

Figure 1.1 Region of Nova Friburgo in Rio de Janeiro (Brazil) after the occurrences of several landslides

Figure 1.2 A catastrophic landslide on Ilha Grande

Figure 1.3 Several landslides took place in Hofu city, Japan

Over the past decades, there has been a dramatic increase in deadly landslides. Therefore, improving the evaluation of landslide risk is an important issue for the entire world.

One important research project nominated SafeLand works towards risk associated with

landslides in Europe and sharing with the entire world the results and data collected. This group was funded by the The Seventh Framework Programme for research and technological development (FP7) of the European Commission. Up to now, several simulation models have been proposed to predict the occurrence of landslides in this group. One of its goals is to improve the knowledge, methodologies and integration strategies for managing the risk of landslide in Europe. However, all data and works are available and accessible to people all over the world. USGS (United States Geological Survey) has a program called "Landslide Hazards Program" with the mission to monitor landslide hazard areas, prediction of new landslides, engages in activities related to the mitigation of the consequences of this natural phenomena. Figure 1.4 shows an example of real-time information provided by USGS; places highlighted are in monitoring state and data such as rainfall, groundwater data from pressure sensors, movement data from displacement sensors and ground vibration from geophones, can be obtained by clicking in one of the pointed places. Japan founded a group in 1963 called "The Japan Landslide Society" with the principal purpose is studying about landslide and its prevention.

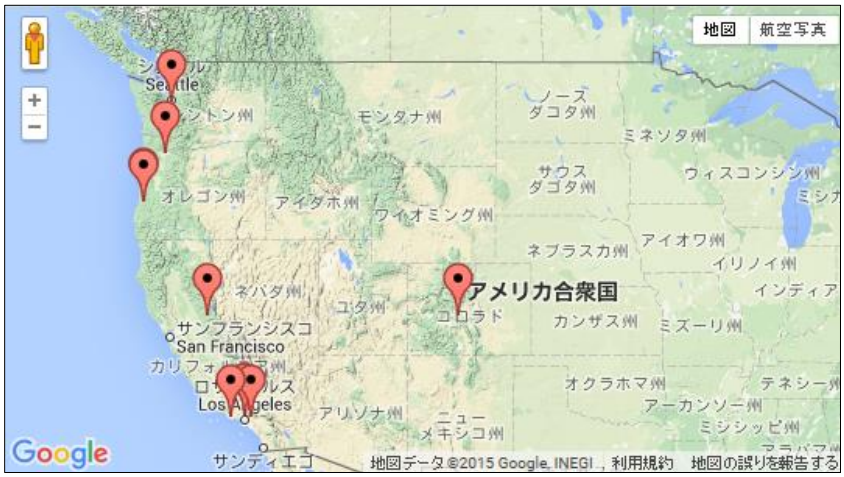

Figure 1.4 Places that are in monitoring state in United States provided by USGS

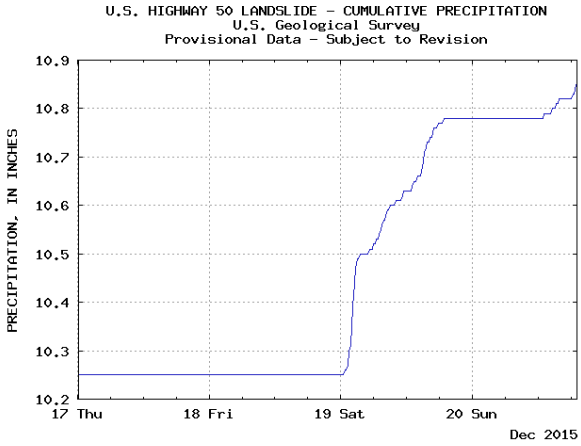

Figure 1.5 Example of the rainfall data provided by USGC

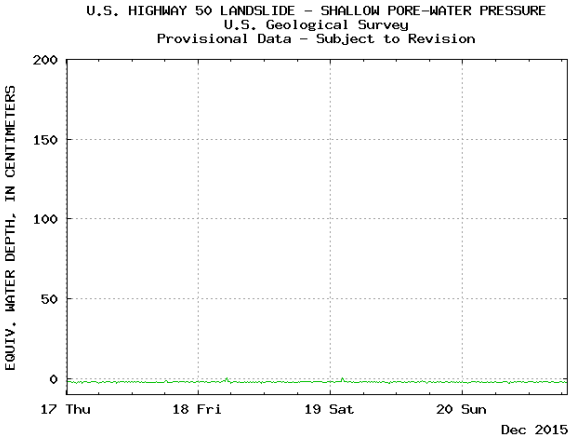

Figure 1.6 Example of groundwater data provided by USGC

The groups mentioned above are just a few examples of attitudes to mitigate the consequences of the "Killer Landslides".

1.2. Actual landslide warning system in Rio de Janeiro

Since 1996, Rio de Janeiro started the Landslide Warning System of Rio de Janeiro called "Alerta Rio". This is a real-time system to warn the possibilities of occurrences of mass movement due to rain that is managed by the GEO-RIO foundation. This system emits forecast heavy rain that can generate flood and/or geotechnical accidents such as landslides. Alerta Rio has a network system composed by 33 rain gauges spread within all regions of the Municipality of Rio de Janeiro (see Table 1.1). These rain gauges send data in real time, every 15 minutes to the central office. The Alerta Rio equip consists of meteorologists, engineers, geologists and technicians who monitoring the weather condition and maintenance of the network equipment during 24 hours a day, 7 days a week.

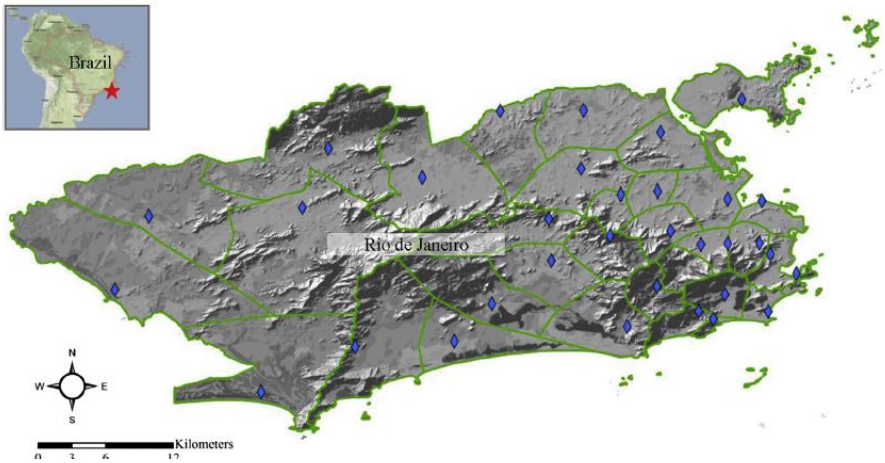

Figure 1.7 Location of the rain gauges in Rio de Janeiro

Table 1.1 Location of the 33 rain gauges spread within all regions of the Municipality of Rio de Janeiro

Location					UTM (SAD69 Zona 23)	
N°	Rain gauges	Latitude	Longitude	Quota (m)	X	Y
1	Vidigal	-22,99250°	-43,23306°	85	681138,532	7456241,298
2	Urca	-22,95583°	-43,16667°	90	688004,213	7460236,157
3	Rocinha	-22,98583°	-43,24500°	160	679831,802	7457041,035
4	Tijuca	-22,93194°	-43,22167°	340	682358,108	7462941,416
5	Santa Teresa	-22,93167°	-43,19639°	170	684951,792	7462971,838
6	Copacabana	-22,98639°	-43,18944°	90	685675,030	7456902,449
7	Grajaú	-22,92222°	-43,26750°	80	677639,269	7463809,403
8	Ilha do Governador	-22,81806°	-43,21028°	0	683708,659	7475959,609
9	Penha	-22,84444°	-43,27528°	111	677059,917	7472757,104
10	Madureira	-22,87333°	-43,33889°	45	670409,679	7469665,020
11	Irajá	-22,82694°	-43,33694°	20	670692,602	7474733,927
12	Bangu	-22,88028°	-43,46583°	15	657403,761	7468956,662
13	Piedade	-22,89182°	-43,31005°	50	673344,642	7467452,646
14	Jacarepaguá/Tanque	-22,91250°	-43,36472°	73	667541,219	7465482,186
15	Saúde	-22,89606°	-43,18786°	15	685875,072	7466833,239
16	Jardim Botânico	-22,97278°	-43,22389°	0	682133,530	7458453,116
17	Barra/Barrinha	-23,00849°	-43,29965°	7	674262,081	7454520,709

18	Jacarepaguá/Cidade de Deus	-22,94556°	-43,36278°	15	667928,198	7461632,847
19	Barra/Riocentro	-22,98129°	-43,40508°	0	662819,045	7458366,675
20	Guaratiba	-23,05028°	-43,59472°	0	646759,839	7560709,033
21	Est. Grajaú/Jacarepaguá	-22,92556°	-43,31583°	105	672722,551	7463726,025
22	Santa Cruz	-22,90944°	-43,68444°	15	634915,936	7465594,315
23	Grande Méier	-22,89056°	-43,27806°	25	676628,743	7467665,546
24	Anchieta	-22,82694°	-43,40333°	50	663886,431	7474809,856
25	Grota Funda	-23,01444°	-43,52139°	11	651526,394	7454108,412
26	Campo Grande	-22,90361°	-43,56194°	30	647538,728	7466493,819
27	Sepetiba	-22,96889°	-43,71167°	62	632068,601	7459406,612
28	Alto da Boa Vista	-22,96583°	-43,27833°	355	676494,085	7459222,483
29	Av. Brasil/Mendanha	-22,85694°	-43,54111°	30	649669,378	7471561,078
30	Recreio dos Bandeirantes	-23,01000°	-43,44056°	10	662606,110	7565320,204
31	Laranjeiras	-22,94056°	-43,18750°	60	685883,625	7462252,656
32	São Cristóvão	-22,89667°	-43,22167°	25	682404,960	7466817,174
33	Tijuca/Muda	-22,93278°	-43,24333°	31	680136,137	7462851,843

This system is formed by the comparison between the rainfall measured by the rain gauges and rainfall thresholds, and landslides occurrences based on 800 past events (d' Orsi et. al.) and rainfall data from a set of five rain gauges. Then, a rainfall threshold was adopted to define the first set of landslide warning levels: R1 or R2 or R2 and R3 (Table 1.2). Furthermore, the second set of alerts defines the density of landslides (Table 1.3) that is divided as follow:

1) Low: indicates the mass movement not triggered by rainfall;
2) Medium: indicates occasional occurrences of landslides caused by rainfall, located in artificial slopes;
3) High: for spreads landslides due to heavy rains on natural and artificial slopes;
4) Very high: for wide-spread occurrences of landslides caused by heavy rain on natural and artificial slopes, especially on roads cuts.

Table 1.2 Rainfall threshold and Landslide warning levels

Warning level	R1 [mm/h]	R2 [mm/24h]	R2 and R3 [mm/24h and mm/96h]
Medium	25-50	85-140	25-50 and 140-220
High	50-80	140-220	50-100 and 220-300
Very high	>80	>220	>100 and >300

Table 1.3 Correlation between warning level, landslide density and main operation procedures

Warning level	Landslide density	Main operation procedures
Low	Landslides not related to rainfall	Website update (every 6 hours)
Medium	Occasional landslides may occur	Website update. Communication to municipal departments
High	Diffuse land sliding may occur	Website update. Communication to municipal departments. Warning bulletin to TV and radio stations
Very high	Widespread land sliding may occur	Website update. Communication to municipal departments. Warning bulletin to TV and radio stations

In short, the databases necessary to conduct this warning system are: rainfall amount and its duration; location, typology and date of occurrences of landslides; level and duration of warnings. The system is powered by a software which sends the last rainfall report every 15 minutes to the team in charge. Facing one of the established requirements, the team is able to emit a warning bulletin on TV, radio and Internet.

Probability of landslides:
Green – Low
Yellow – Medium
Red – High
Black – Very high

Figure 1.8 Example of online monitoring system provided by Alerta Rio

Calvello et. al. (2014) conducted a series of analysis to validate the performance of this warning system. The target of this study was 4 alert zones during the four-years 2010-2013. The result showed 714 landslides in which 502 were during alert phase. One of the concerns of this method is the false alert emissions. False alert is defined by the transmission of the alert in which do not occur late landslides. A little mistake in the rainfall threshold is pointed to be the reason of the false alert emissions.

1.3. Early warning system in Japan

Since 30 August 2013, the Japan Meteorological Agency (JMA) began the Emergency Warning System to alert people to the risk of catastrophes in association with natural phenomena. In case of risk of sediment disasters caused by heavy rain, JMA issues various warnings to alert people living in the dangerous area. The risk of sediment disaster is shown for every 5 km grid square. The types of warnings are divided in 5 levels: equivalent to sediment disaster alert (based on observed rainfall), equivalent to sediment disaster alert (based on forecast rainfall), equivalent to heavy rain warning, equivalent to heavy rain advisory and below level of heavy rain advisory. Figure 1.9 presents a warning sample emitted by JMA on 9 February 2016 at 18:20, in which there was no risk of imminent disaster.

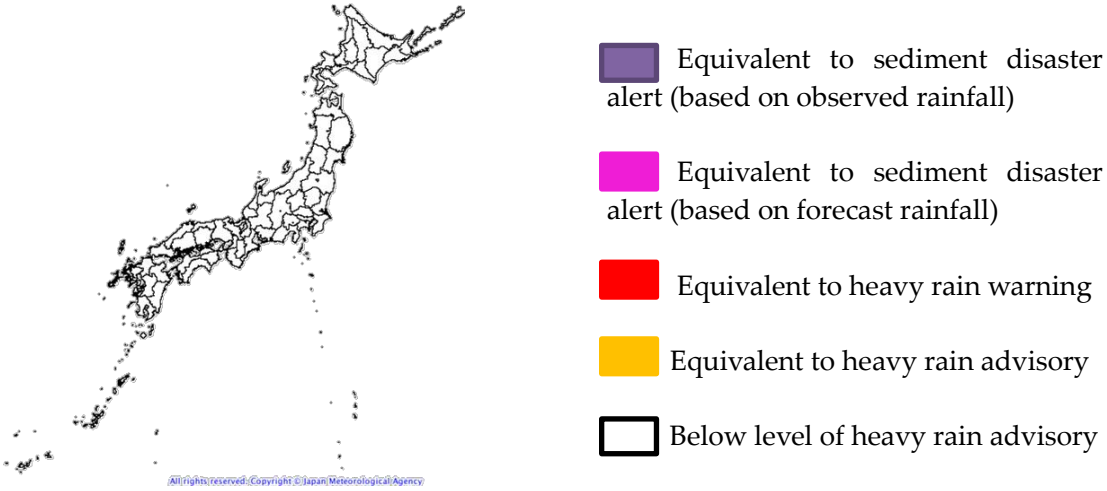

Figure 1.9 Warning map provided by JMA

In accordance with the recent increase of sudden rainstorms and mudslides, the government of Japan started to work together with universities and other institutions to construct an early warning system to mitigate the negative impacts of these natural phenomena on society (Japan Times, 2014) with estimated date to start the prediction of mudslides by around 2030. The National research Institute for Earth science and Disaster prevention (NIED) is in charge of this mission.

1.4. Structure and perspective of this study

The development of methodologies to predict the occurrences of landslides is assuming an important role in geomorphological and geotechnical literature. They are based on field study, laboratory experiments and/or numerical simulations. Here, we will focus on the method using numerical simulation.

Many researches have utilized the numerical simulation as an important tool to simulate the behavior of landslides. Numerical simulation provides a way to validate new theories, analyze new phenomena, and help on the interpretation of an experiment and so on. Researches are preferring the numerical simulation instead of the experiment in laboratories or on sites due to its not expensive cost, safety and time-consuming. It is noteworthy, that numerical simulations can be formulated in three types of domain discretization: grid-based methods, meshfree methods and meshfree particle methods.

The grid-based methods are established on frames for describing the physical governing equations. However, this method has founded a major obstacle in reproducing a complex geometry or irregular grid by the construction of a regular grid using the Eulerian grid method. In order to reproduce reasonable results, it is required to add complex mathematical transformation in which can turn to a very expensive money problem. This method also it is not recommendable to simulate large deformations, moving material interfaces, free surfaces, deformable boundaries and situations where the principal concern is a set of discrete physical particles rather than a continuum.

The idea behind the meshfree methods is to eliminate the unviable aspects caused by generation of frames on the grid-based methods, while maintaining the accuracy and the

stability of the system.The meshless methods available can be classified based on formulation procedure: particle methods, weak form formulations and strong form formulations. Strong form method presents a simple algorithm and very computational efficiency. However, it is less accurate and unstable. Weak formulation methods are very good stable and exhibits excellent accuracy. However, it is necessary to solve the numerical integration that turns to a very computational expensive problem.

We would like to give a special attention to the meshfree particle method that uses a set of finite number of discrete particles to perform a case of a system and to study the movement of the system. The first research involving this method is dated in 1949 presented by Metropolis and Ulam, named by The Monte Carlo Method. Then, a model called Molecular dynamics was developed to study a typical atomistic was developed by Alder and Wainright in 1957. Many other examples could be mentioned, however a method called Smoothed Particle Hydrodynamics (SPH) deserves a particular space in this chapter.

Here, we will present an important timetable (Figure 1.10) to the development of our research. Lucy, Gingold and Monaghan started to study the interaction of stars in astrophysics using a macrospopic meshfree particle method in 1977. For this purpose, the SPH was used to model compressible fluids at elevated Reynolds number. In 1994, Monaghan provided a SPH method applied in a simulation of incompressible fluids, where he showed that the boundaries could be easily incorporated. Morris et. al. (1997) proposed a modification in the SPH method to be able to perform a simulation of incompressible fluids for low Reynolds numbers, which provided accurate estimates of velocity. Cleary et al. (2001) described the inclusion of head transfer and solidification through the temperature-dependent viscosity. Then, in 2002, Cleary et al. applied into elasto-plastic solid. More recently, Pastor et al. (2014) analyzed an application of a SPH into a depth-integrated model to verify the landslides behavior.

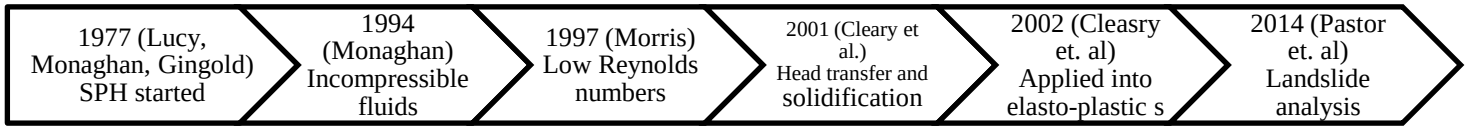

Figure 1.10 Important timetable to the development of our research

The solution proposed in our research is a simplification of a SPH depth-integrated method. The problem domain is represented by generated particles unconnected in which interact with the neighboring particles by a pair-wise model. To avoid numerical problems such as the tensile instability, we decided not to consider the weighted average of variables that is connected to the second order derivative of the smoothing function.

1.4.1. Overview

The present evaluation method is composed of several techniques. First, we prepare a DSM (Digital Surface Model) of a region of interest, which is constructed by stereo-photogrammetric method. We use the two photogrammetric images taken by the PRISM sensor mounted in ALOS satellite (ALOS project report 2011). The data cover the entire surface of the earth, and the resolution of the obtained DSM is about several meters depending on the atmospheric condition. Next we adopt the conventional linear stability analysis for each DSM pixel. We consider the physical and mechanical properties of surface soil at rest, including the water saturation, and determine the area of initial slope failure. Finally, the flow simulation is carried out for the entire area to obtain the affected area due to the slope failure and the subsequent flow. The simulation result is compared with the actual damage area in a quantitative manner, which is described in the following sections.

The heart of the present study is the comprehensive parametric study in the flow simulation. As mentioned above, it is difficult to evaluate the mechanical parameters of surface soil during flow regime from in-situ testing. Therefore, the result of the parametric study provides useful information for the numerical simulations.

The flowchart of the present evaluation method is shown in Fig.1.9.

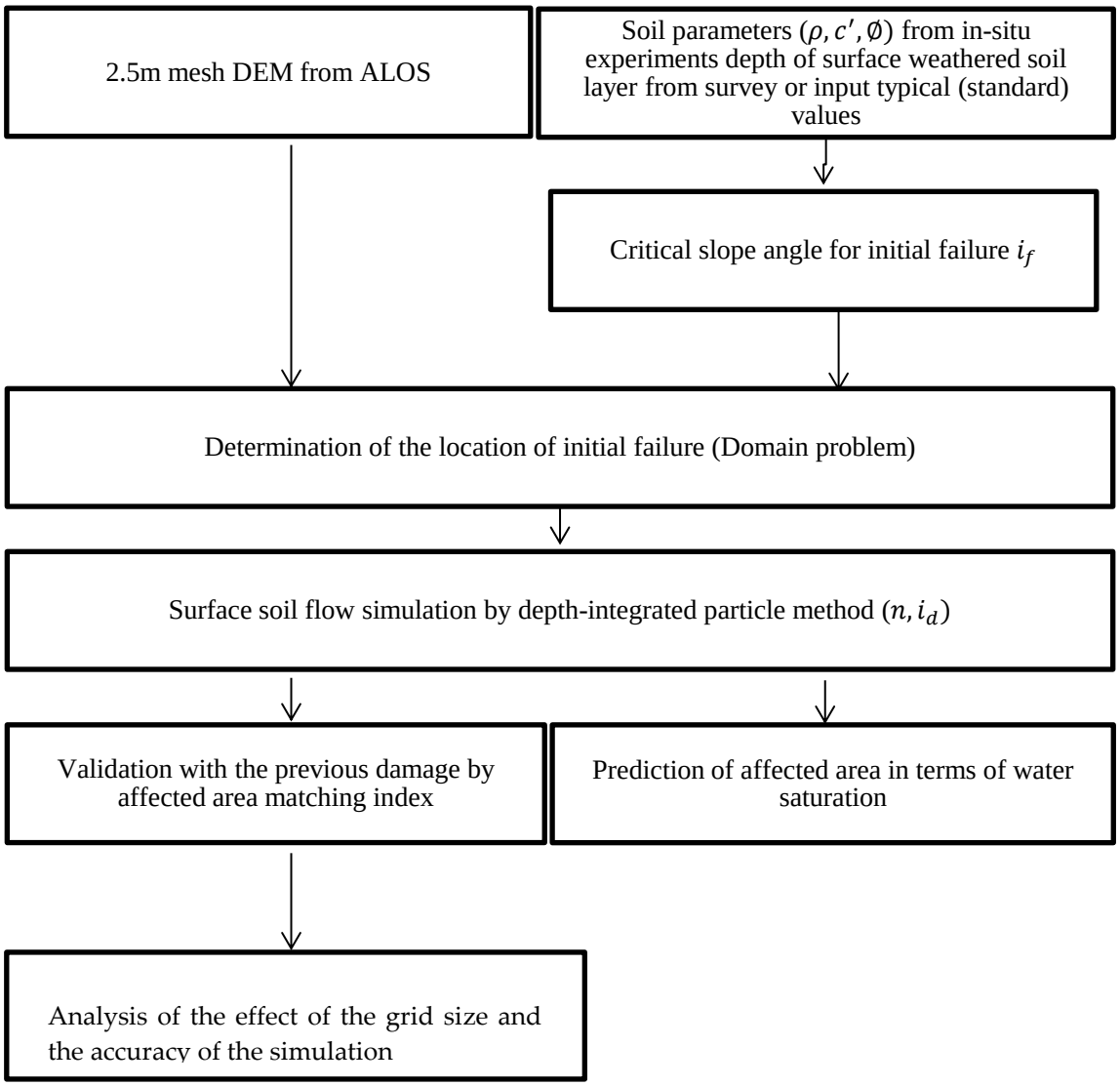

Figure 1.11 Flowchart of the evaluation procedure

1.4.2. 1D Slope stability analysis for the prediction of slope failure area

The equation of safety of factor was developed in order to analyze the slope stability. This process involves determining and comparing the shear stress carried over the rupture surface with the shear strength of the soil (Eq. 1.1). When the F_s is equal to 1, the slope is in an imminent risk of rupture. While, values for $F_s > 1$ are designed for showing the stability of the slope. Values $F_s < 1$ represent unstable slopes. The safety of factor can vary with time, since a slope can pass year without slipping and at a certain time, can have its stability altered due to new factors conditions.

We adopt the conventional linear stability analysis for each pixel of the DEM. Usually, the safety of factor F_s is defined as:

$$F_s = \frac{shear\ strength\ of\ the\ soil}{shear\ stress} = \frac{\tau_f}{\tau} \tag{1.1}$$

The shear strength of the soil can be represented as:

$$\tau_{f=c'+\sigma_v' tan\emptyset'} \tag{1.2}$$

Where, the effective normal stress σ_v'b is given by:

$$\sigma_v' = \sigma_v - \gamma_w h_2 cosi_f \text{ and } \sigma_v = (\gamma_t h_1 + \gamma_{sat} h_2) cosi_f \tag{1.3}$$

The shear stress τ is:

$$\tau = \sigma_v sini_f \tag{1.4}$$

Substituting the mentioned relationships, we obtain:

$$F_s = \frac{c' + \{\gamma_t h_1 + (\gamma_{sat} - \gamma_w) h_2\} cos^2 i_f\ tan\emptyset'}{(\gamma_t h_1 + \gamma_{sat} h_2) sini_f\ cosi_f} \tag{1.5}$$

Where i_f is the critical slope angle for failure, $h_1$and $h_2$are the non-saturated and saturated soil

heights, respectively, $\gamma_t$and $\gamma_{sat}$are the unsaturated and saturated unit weight of the surface soil, γ_w is the unit weight of water, and c´and ∅´ are the cohesion and the internal friction angle of surface soil, respectively, in terms of effective stress.

We assume that the depth of the slope failure can be roughly evaluated as a weathered soil depth by in-situ survey in the case of shallow slope failure.

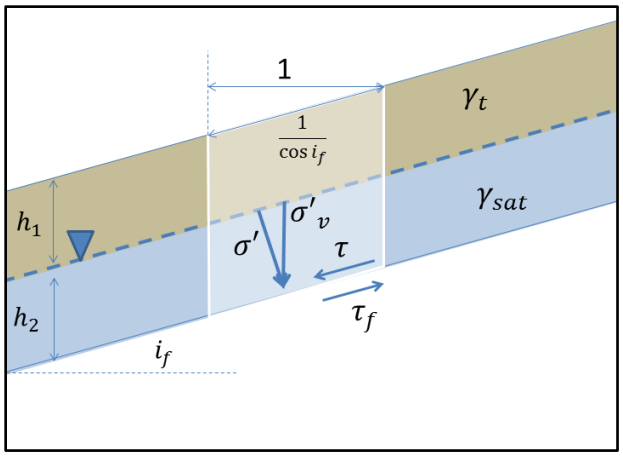

Figure 1.12 Stability analysis of infinite one-dimensional slope

1.4.3. Flow simulation

This research proposes a methodology to determine areas susceptible to landslides from satellite images. Once a surface soil mass begins to slip, its flow behavior cannot be described by its mechanical parameters before failure, because the soil mass is mixed up during the flowing process and even behaves like a complex fluid when the water content is large. Therefore, most of the simulations so far have been applied either slope failure regime or post-failure flow regime. The attempts to fill this gap and to construct the unified constitutive relation have been made extensively in granular physics fields and soil mechanics field. However, considering the difficulty in obtaining the flow parameters of surface soils site by site, it is reasonable to divide the whole behavior into the pre-failure and post-failure regimes and apply rather simple constitutive equation for each of them.

We have developed an efficient flow simulation method that is a kind of depth-integrated particle method. This simplified depth-integrated particle-based model enables us

to carry out stable flow simulation with relatively small number of particles. This feature leads to the drastic reduction of computational cost, which is essential to carry out a comprehensive parametric study for wide area landslide simulation presented in the subsequent section. It is based on the commonly-used shallow water equation (item 3.2) formulated in Lagrangian frame.

Numerous studies have attempted to explain the behavior of landslides through numerical simulation. Some similarities with Hungr's (1995) techniques (e.g. lagrangian solution of the equation of motion and a homogeneous "apparent fluid" assumed) resemble also in two of the purposes of the models: The prediction of the mass movement and a definition of a typical values for the mechanical parameters. However, due to DAN (Dynamic Analysis proposed by Hungr in 1995) simplified reduction of a complex and heterogeneous three dimensional problem into a two dimensional numerical solution (including the insertion of the width of propagation as part of the input data), causes a major limitation to predict the occurrences of mass movement. Hungr's model offers a satisfactory result to define values for the mechanical parameters of the soil by doing back analysis in a set of case histories of literature. Similarly, our technique determines the parameters of surface soil on the statistical basis. Moreover, our methodology by using a precise topographic data can predict the occurrences of landslides with a satisfactory accuracy. Whereas, our numerical model is represented in lagrangian frame in horizontal Cartesian space using a simplified SPH scheme. Alike, Hungr's model we ventured to mold the slide mass as several columns represented by particles, that keeps the volume constant throughout the path. The pressure between the particles is discretized by the difference of the height between the neighboring particles that it is calculated from the hydraulic gradient. Also, in our method a DSM (Digital Surface Model) plays an important part in the accuracy of the simulation.

Hungrs, as many other researches, considered a single flow (per evaluation time), while we are able to conduct the evaluation in several landslides in a wide-area.

2. REMOTE SENSING METHODS

2.1 Geographical Information Service – GIS

From 2010, the Geotechnical Engineering Laboratory of the University of Tsukuba has developed a software for storage and manipulation of a wide-area database that cover the Japanese territory. The system, roughly translated as "Slope collapse and risk assessment support system" offers data collection that includes topographical information, geological, geomorphological, hydrological, etc. Iwamoto et al. (2011) outlined the first efforts to integrate this feature with the simulation method proposed in this research.

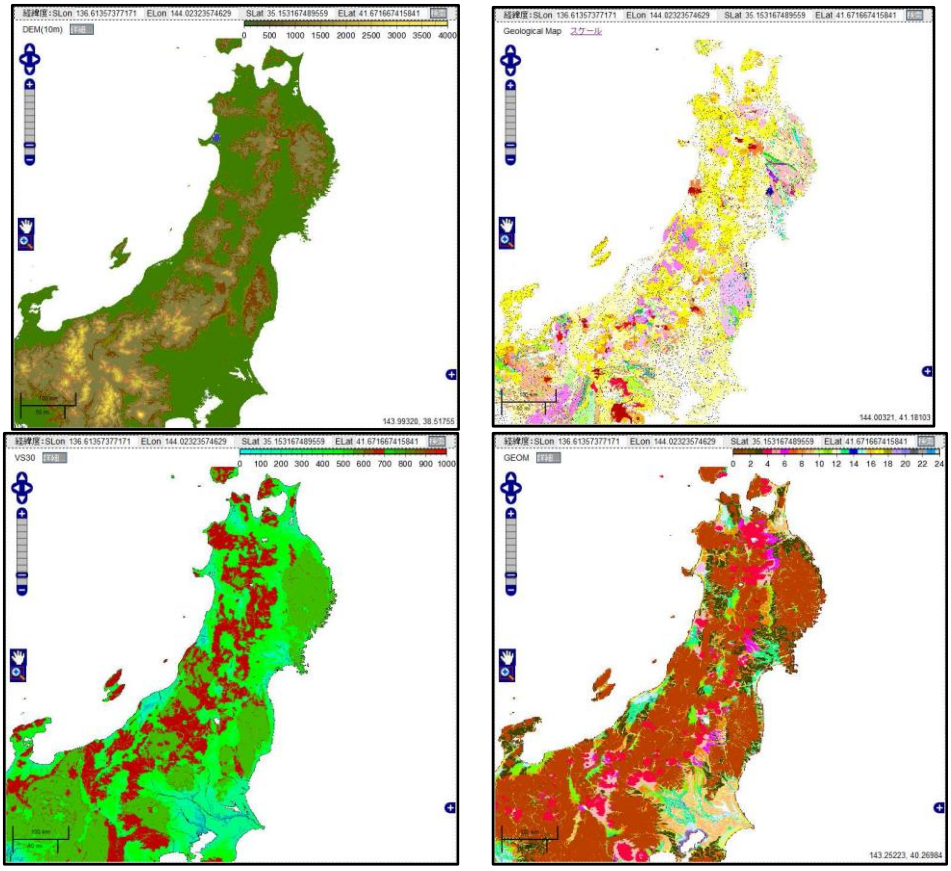

Figure 2.1 Map collection provided by the "Slope collapse and risk assessment support system"

The first step in this process is to select the desired location. The output data provides

information about utm coordinates, latitude and longitude, elevation, Vs30, GEMO, SWI, road and landslide.

Table 2.1 Example of information provided by the System

UTM (E)	UTM (N)	Longitude	Latitude	DEM	Vs30	GEMO	Swi
741838.3262	3.77E+06	131.62088	34.07957	382	1	775	253.7089
741848.1846	3.77E+06	131.62099	34.07957	388	1	775	253.7089
741858.0431	3.77E+06	131.62109	34.07957	394	1	775	253.7089
741869.3099	3.77E+06	131.62122	34.07957	402	1	775	253.7089
741879.1684	3.77E+06	131.62132	34.07957	412	1	775	253.7089
741889.0269	3.77E+06	131.62143	34.07957	417	1	775	253.7089
741898.8854	3.77E+06	131.62154	34.07957	423	1	775	253.7089
741910.1522	3.77E+06	131.62166	34.07957	430	1	775	253.7089
741920.0107	3.77E+06	131.62177	34.07957	437	1	775	253.7089
741929.8691	3.77E+06	131.62187	34.07957	444	1	775	253.7089
741941.136	3.77E+06	131.62199	34.07957	450	1	775	253.7089
741950.9944	3.77E+06	131.6221	34.07957	455	1	775	253.7089
741960.8529	3.77E+06	131.62221	34.07957	460	1	775	253.7089
741970.7114	3.77E+06	131.62231	34.07957	467	1	775	253.7089
741981.9782	3.77E+06	131.62244	34.07957	473	1	775	253.7089

Vs30 is the average shear-wave velocities down to 30 m. Vs30 depends on the velocities and thickness of each existing layer in the first 30 m above the ground and allows a soil classification. Two set of coefficients are developed for deriving Vs30: one for places where there is no movement in the tectonic plates and changes in topography are more overpowered, and one for active tectonic regions which have dynamic topographic relief.

SWI is a short term to Soil Water Index set by JMA (Japan Meteorological Agency) as an important index to represent the quantity of water in the soil. JMA made a relationship between the slope failure and its current SWI with the SWI when a slope failure occurred in the past. This study set out with the aim of assessing the slope failure risk. To calculate the SWI, Ishihara and Kobatake (1979) proposed a method using three stage serial connected tank models. The final value for SWI is demonstrated as a sum of the total height of three tanks. Prior to analyzing the proposed method, a sketch of the three tanks is shown in Figure 2.2.

Where L_1, L_2, L_3 and L_4 are height of the outlet of the side walls, α_1, α_2, α_3 and α_4 are coefficient of discharge and $\beta_1, \beta_2, \beta_3$ and β_4 are coefficient of permeability.

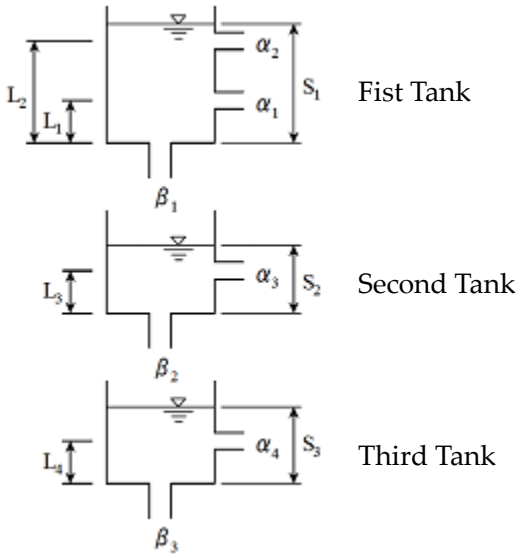

Figure 2.2 Sketch extracted from Japan Meteorological Agency

Table 8.2 shows the parameters found by Ishihara and Kobatake (1979) to use in the tank model.

Table 2.2 Parameters for the tank Model (Ishihara and Kobataka, 1979)

	First stage	Second stage	Third Stage
Height of the outlet of the side walls (mm)	$L_1 = 15$	$L_3 = 15$	$L_4 = 15$
	$L_2 = 60$		
Coefficient of discharge (1/hr)	$\alpha_1 = 0.10$	$\alpha_3 = 0.05$	$\alpha_4 = 0.01$
	$\alpha_2 = 0.15$		
Coefficient of permeability (1/h)	$\beta_1 = 0.12$	$\beta_2 = 0.05$	$\beta_3 = 0.01$

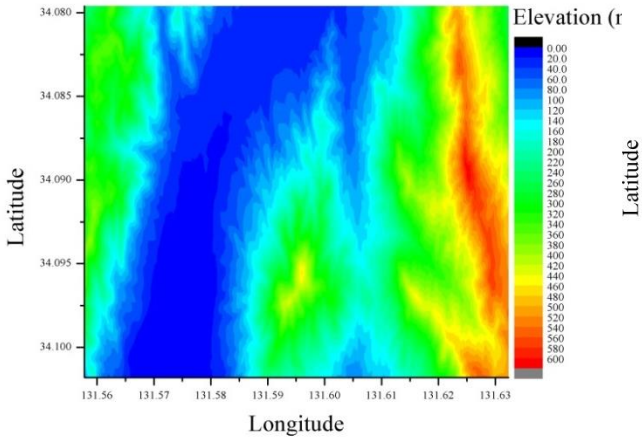

Figure 2.3 Example of the elevation provided by the System

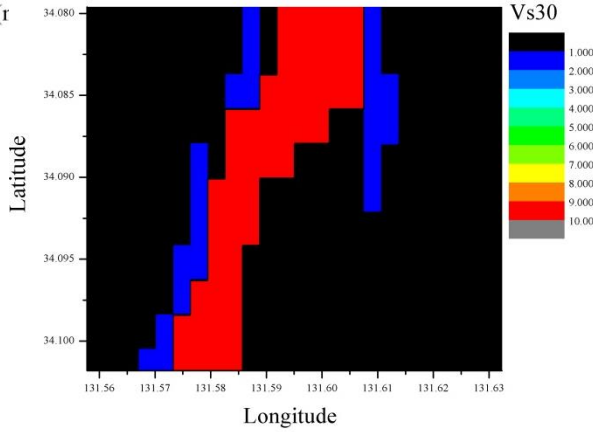

Figure 2.4 Example of the Vs30 provided by the System

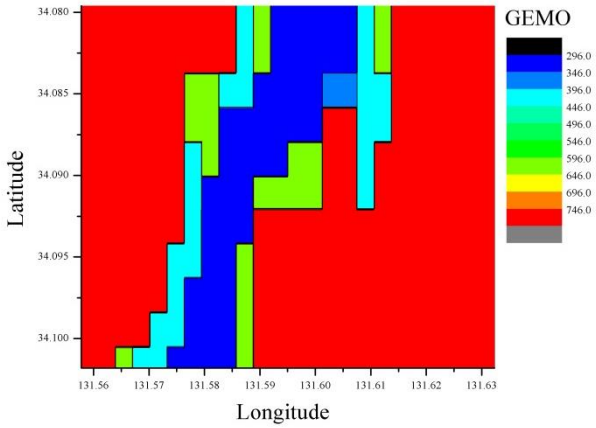

Figure 2.5 Example of the geomorphological data provided by the System

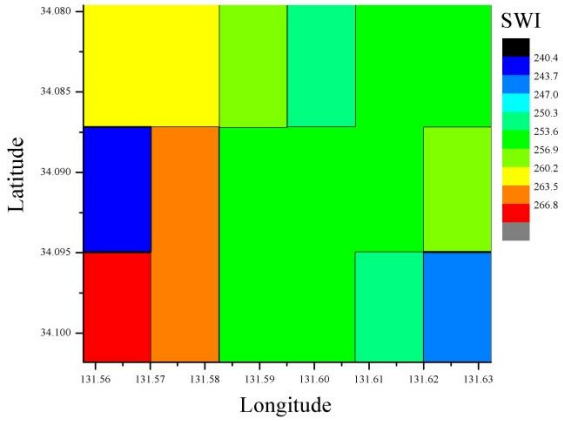

Figure 2.6 Example of the hydrological data provided by the System

2.2 Advanced Land Observing Satellite - ALOS

The chosen remote sensing method for this research uses images from ALOS satellite. ALOS (Advanced Land Observing Satellite) was a remote-sensing equipment that had permitted rigorous land coverage and collected data for mapping on a scale of 25,000 to 1. This satellite was launched on January 24, 2006 by the Japan Aerospace Exploration Agency (JAXA), in the Space Center located in Tanegashima (Japan). The operation phase of providing data to the public started in October 24, 2006.

The Japanese program of Earth observation consists of two series: the satellites used mainly for atmospheric observation and marine, and satellite mainly used for earth observation. ALOS satellite has being used for mapping, disaster monitoring and survey of natural sources.

The ALOS satellite is derived from the technology developed by his predecessors: ADEOS and JERS-1. To ALOS was added a high speed, data handling capacity and advanced precision in determining their spatial location. ALOS had a control of orbit system based on dual frequency of GPS.

Until May 2011, the satellite covered all the territory of Japan and others countries including Brazil. Successors of ALOS are ALOS-2, launched on Saturday 24May 2014, and ALOS-3 scheduled to be launched during 2015. Attractive feature from ALOS-3 is the optical sensor called PRISM-2 with high resolution equal to 0.8 m, whereas the former PRISM had 2.5m of resolution.

ALOS had three remote sensing instruments: PRISM (Panchromatic Remote- sensing Instrument for Stereo Mapping) abled to acquire three-dimensional images of Earth's surface, AVNIR-2 (Advanced Visible and Near Infrared Radiometer type 2) for land cover needs, and PALSAR (Phased Array type L-band Synthetic Aperture Radar) abled to get daytime and nighttime imagens without interference of cloudiness. Depending on the function there is a sensor suitable for the desired purpose. A summary of the three sensors related to respective purposes can be seen on Table 2.3.

Table 2.3 Advanced Land Observing Satellite's technical features

	PRISM	AVNIR-2	PALSAR
Purpose	Had three independent optical systems, produ-cing stereoscopic image to provide an accurate digital surface elevation data with 2.5 meter spatial resolution.	Infrared radiometer to obtain data on land use and vegetation with 10 meter spatial resolution.	Detect changes in to-pography and geology. Useful for monito-ring the earth surface chan-ges.

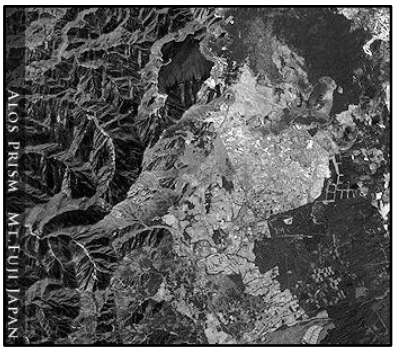

Figure 2.7 ALOS satellite image using PRISM sensor sample showing Mt. Fuji (JAXA)

Figure 2.8 ALOS satellite image acquired by AVNIR-2. (JAXA)

Figure 2.9 ALOS satellite image using PALSAR sample showing Mt. Fuji (JAXA)

The PRISM sensor operates in the visible light range, with a panchromatic band and spatial resolution of 2.5 m. Able to acquire images to generate digital surface models (DSM) with great accuracy, it has three independent optical systems for viewing nadir with targeted, front (forward) and rear (backward), producing images in stereoscopy along the orbit. Each telescope consists of three mirrors and several CCD detectors, and the telescope aimed at the nadir covers a range of 70 km, while the other two overlying a range of 35 km each. The PRISM provides data with high accuracy (1 meter) for the development of digital surface models and surveys to scale up to 1: 25,000.

The forward and backward telescopes are inclined 24 and -24 nadir, thereby obtaining a base / height ratio of 1.0, ideal for stereoscopy. Thus, the field of view (FOV) of PRISM, is able to acquire three images with full stereo coverage (Triplet) covering 35 km without any mechanical drive or satellite slope. Major characteristics can be founded in Table 2.4.

Table 2.4 Major characteristics of PRISM sensor

Number of Bands	1 (Panchromatic)
Wavelength	0.52 to 0.77 micrometers
Number of Optics	3 (Nadir; Forward; Backward)
Base-to-Height ratio	1.0 (between Forward and Backward view)
Spatial Resolution	2.5m (at Nadir)
Swath Width	70km (Nadir only) / 35km (Triplet mode)
S/N	>70

MTF	>0.2
Number of Detectors	28000 / band (Swath Width 70km) 14000 / band (Swath Width 35km)
Pointing Angle	-1.5 to +1.5 degrees(Triplet Mode, Cross-track direction)
Bit Length	8 bits

Table 2.5 Observation modes

Mode 1	Triplet observation mode using Forward, Nadir, and Backward views (Swath width is 35km)
Mode 2	Nadir (70km) + Backward (35km)
Mode 3	Nadir (70km)
Mode 4	Nadir (35km) + Forward (35km)
Mode 5	Nadir (35km) + Backward (35km)
Mode 6	Forward (35km) + Backward (35km)
Mode 7	Nadir (35km)
Mode 8	Forward (35km)
Mode 9	Backward (35km)

In order to evaluate the accuracy of the simulation of the prediction of landslides proposed by this study, the chosen satellite images were acquired before the actual disaster date. The best satellite images (i.e., images with the lowest percentage of clouds) for the places chosen as case studies and their parameters are shown in Figure 2.10 and Figure 2.11.

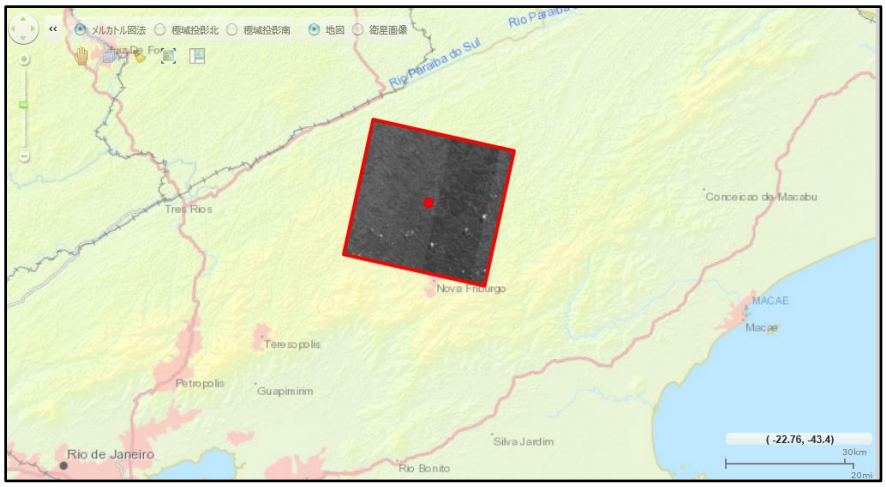

Figure 2.10 Location of the acquired satellite image in Nova Friburgo

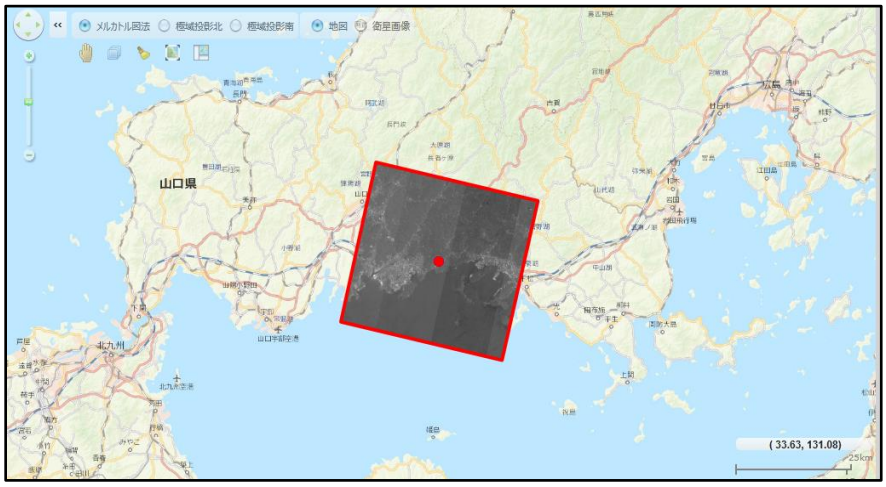

Figure 2.11 Satellite image location for Hofu's case study

2.2.1 Satellite Image Processing

After que acquisition of the two photogrammetric images taken by ALOS satellite using PRISM sensor, it was necessary to evaluate as a stereo-pairs to construct a Digital Elevation Model (DEM) whose minimum grid size is 2.5m horizontally and 1.0m vertically. To do so, a web service provided by the department of Grid Technology Research Center in the National Institute of Advanced Industrial Science and Technology (AIST) was used. The name of this service was GEO (Global Earth Observation) Grid. While GEO grid was based on many IT components (e.g., OGSA-DAI, VOMS, GAMA, Gridsphere, etc) developed by world-wide grid communities including the cooperation of Japan. The idea was to accelerate GEO sciences based on the idea that necessary data and computational resources were virtually integrated with an ease-of-use interface, which was enabling by a set of grid and web service technologies. Unfortunately, this service had the operation discontinued in 2011.

To well understand the conversion method adopted it is necessary to clarify that each pixel represents an area on the Earth's surface. As mentioned beforehand, each pixel has 2.5 m in this study. The CRISP (Centre of Remote Imaging, Sensing and Processing) described the method as the interpretation of each pixel based on its intensity, where the intensity value performs the measured physical quantity (e.g. solar radiance in a given wavelength band

reflected from the ground, emitted infrared radiation or backscattered radar intensity).

An alternative method for processing the satellite image into a DEM was used by Ni Zhang (2015). The first step of this process is the acquisition of commercial software, named Map Matrix. Then, at least, 5 control points for a pair of images are needed to georeferenced the satellite images. The location of the control points can be finding in Google Earth, for example.

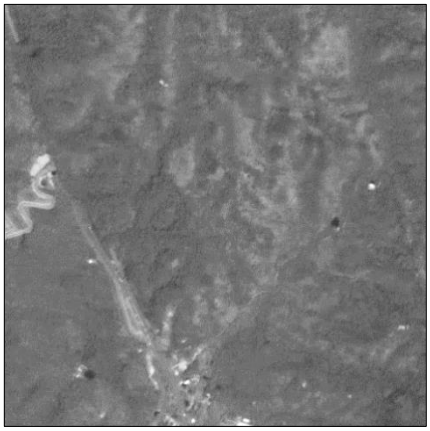

Figure 2.12 Example of ALOS Satellite image

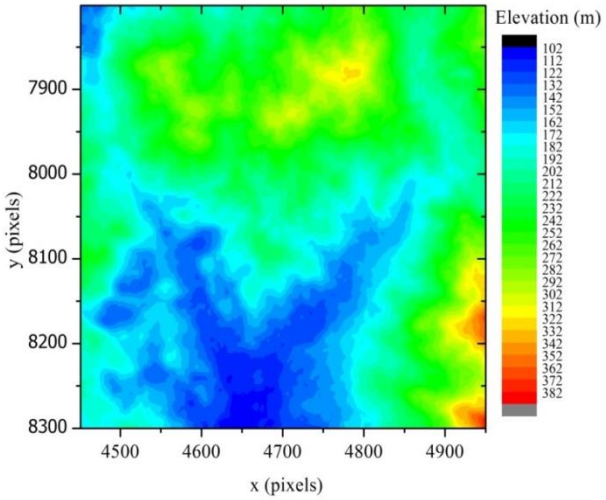

Figure 2.13 Example of a DEM converted image

2.2.2 Accuracy of DEM provided by Satellite Image

There is evidence that a well-represented DEM image plays a crucial role to perform a landslide simulation near to the real case. Therefore, a DEM image with a reasonable accuracy is an important component in our study.

For this study, the generated DEM was compared with an official map provided by the Geospatial Information Authority of Japan (GIS) in the case of Hofu city. For the case in Nova Friburgo, Brazil, Google Earth was used. The technique to analyze the accuracy of the generated DEM is similar to both case studies. Therefore, to illustration purposes, a small area in Hofu city will be shown below:

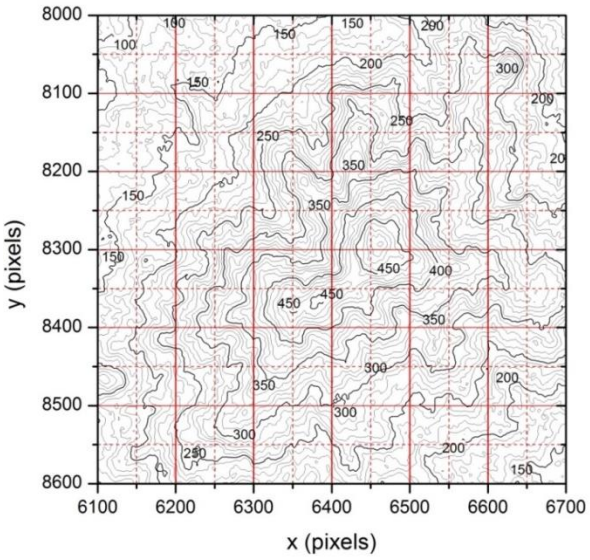

Figure 2.14 Generated DEM image

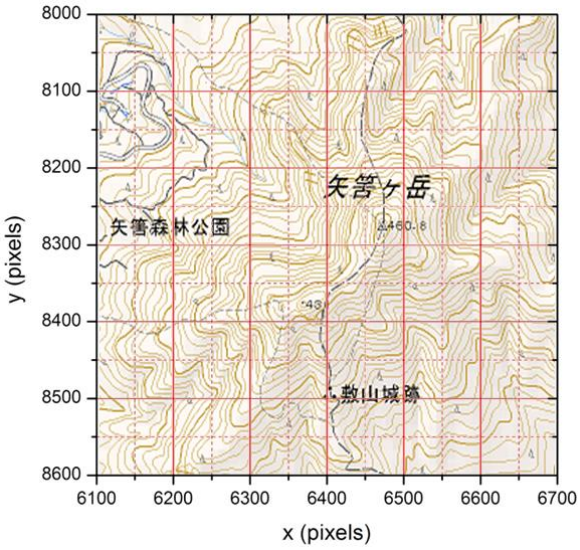

Figure 2.15 Map provided by Geospatial Information Authority of Japan (GIS)

The process consists of overlapping the generated DEM image with an official map and analyzes the differences found. In case of the differences are insignificant and not affect the simulation result (Figures 2.14 and 2.15), the generated DEM is considered useful. In general, the DEM images showed good matching and could be used for the purpose of this study.

Prior to analyzing better the accuracy of the generated image, we also exhibit a small area in Nova Friburgo, as well as its profile. Figure 2.16 shows a map acquired by Google Earth measuring 1125 m by 1680 m. B'-B indicates the location chosen to examine and compare the profile generated using Google Earth. Figure 2.17 provides a A'-A location of the profile for the same purpose mentioned previously, however this image was generated by the imaging process described in item 2.2.1, where two satellite images were assessed as a stereo-pairs to construct a DEM image.

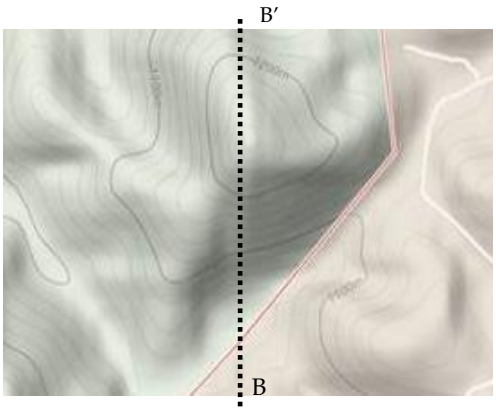

Figure 2.16 Map provided by Google Earth with quote elevations

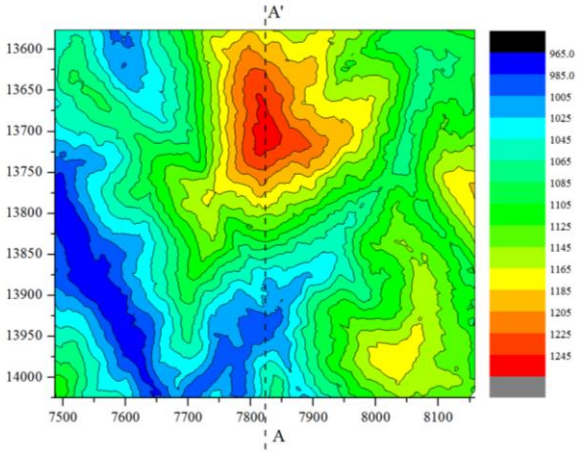

Figure 2.17 DEM processed image

Figure 2.18 compares the profiles when the source was Google Earth (red line) and DEM image processing (black line). It is apparent that the profiles are not perfect overlapped. However, this result is considered reasonable and give us a good estimation of the landscape representation.

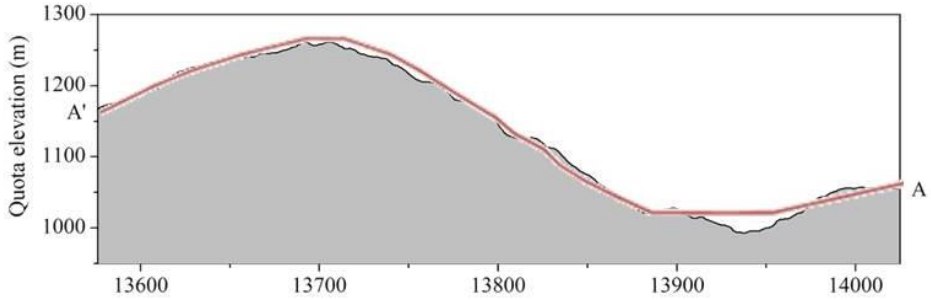

Figure 2.18 A'-A indicates a profile generated using a DEM processed image. B'-B indicates a profile of the same location acquired using Google Earth

One important point that should be mentioned is that some parts of the satellite image could not be used due to large interference on the accuracy of the DEM image (Fig. 2.20). The discrepancy is attributed to clouds and their shadows (Fig. 2.19) that cover some parts of the region of interest, which turns the choosing of a good satellite image a difficult step of this research because it is unlikely to find a totally free clouds satellite image.

Clouds have been recorded by NASA (National Aeronautics and Space Administration) over decades of satellite observations and astronaut photographs. King et al. (2013) find's indicates that about 67 % of Earth's surface is covered by clouds. The most affected area is over the ocean, where only 10% of the sky is completely clear of clouds at any one time. Overland, this number increase to 30% of completely cloud free. Therefore, finding an area completely cloudless is very difficult. The disturbance that a cloud can cause in a DEM image owes to the fact that a satellite image is a two dimensional array of pixels, where each pixel has a value of intensity and it is located by an address characterized in columns (x direction) and lines (y direction). Each pixel should represent an area on the Earth's surface; however, as we mentioned beforehand it is very common to find some interference (e.g. clouds, shadows) on satellite images. In this case, it is not easy to interpret the data from the earth's surface up to now. Thus, we attempt to acquire an area with fewer interruptions as possible.

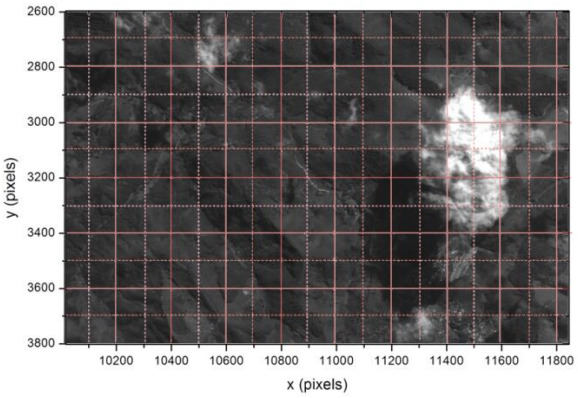

Figure 2.19 Example of a ALOS satellite image with clouds

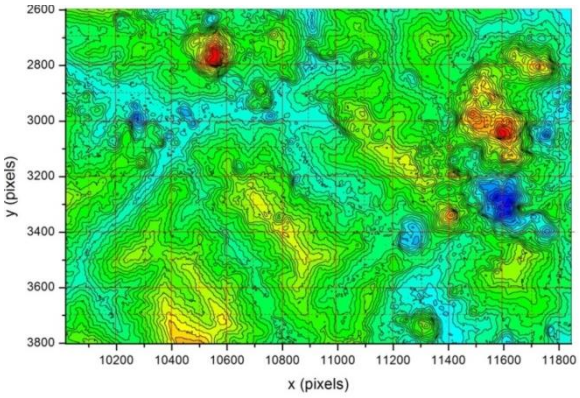

Figure 2.20 DEM image generated with the interference of clouds

2.3 Laser scanning process

In recent years, it has intensified the development of new technologies to be applied to aircraft. A technique called LiDAR (Light Detection and Ranging) was used to acquire images with a spatial resolution equal to 1.0 m in Hofu city – Yamaguchi Prefecture, Japan. Basically, in this remote sensing method the distance is measured by illuminating an area with a laser and examining the light reflected for producing different types of mapping with great accuracy

and quickness.

The purposes are diverse as follow:

- Mapping of corridors (e.g. roads, railways, waterways, pipelines, electrical transmission network);
- Mapping of urban (e.g. cadastral bases);
- Engineering projects;
- Planning and environmental monitoring.

Prior to analyzing the difference between a contour map generated from a 1.0 m grid size (Figure 2.21) and a 2.5 m grid size (Figure 2.22), the process of generation of DEM images were carried out for different remote sensing methods (i.e. Laser Scanning Process and Satellite Image). The next step of this research will evaluate the behavior of the flow simulation under a landscape with a better spatial resolution (i.e. 1.0 m) and analyze it in the perspective of the accuracy of the flow simulation.

Figure 2.21 Contour map generated from the laser scanning process

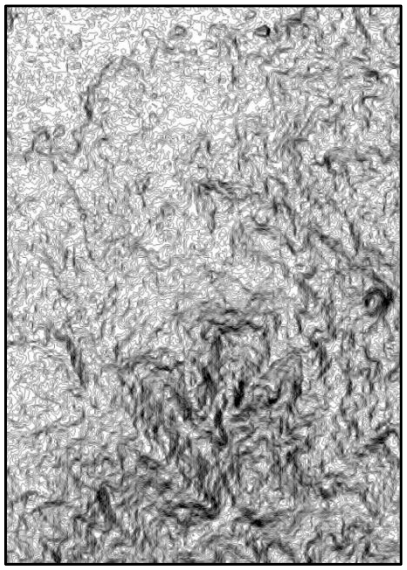

Figure 2.22 Contour map generated from ALOS satellite image

3. DEPTH-INTEGRATED PARTICLE METHOD

3.1 Meshless method

Finite Element Method (FEM) is a conventional grid-based model frequently used to model groundwater flow with a satisfactory accuracy and ability to handle irregular boundaries. The problem domain boundaries are represented by mesh in proper sizes and good shape in order to avoid inaccurate results. Therefore, the construction of an adequate mesh plays an important role in the FEM accuracy. Depending on the difficulty of the problem to be represented, it is necessary more complicated boundaries, turning the construction of the meshes further tough which limit their applications to many problems. To surpass such trouble, meshless methods have been studied. The idea of the meshless method is to represent desired situations with an accurate result and stable numerical solution for integral equations without a construction of any mesh.

The meshless methods available can be classified based on formulation procedure: particle methods, weak form formulations and strong form formulations. Strong form method presents a simple algorithm and very computational efficiency. However, it is less accurate and unstable. Weak formulation methods are very good stable and exhibits excellent accuracy. However, it is necessary to solve the numerical integration that turns to a very computational expensive problem. The particle method employs a group of finite number of discrete particles to represent the domain problem and the movement of the system. There are various meshless particle method; one of the most studied is the Smoothed Particle Hydrodynamics (SPH) method created by Lucy, Gingold and Monaghan in 1977 to model the phenomena of astrophysical. Posteriorly, the SPH method application was extended to different types of problems of continuum solid and fluid mechanics. Therefore, researchers have been doing modifications to better fit the required purposes.

The meshless particle method proposed in this study is a simplification of the SPH (Smoothed Particle Hydrodynamics) method. The problem domain is represented by generated particles unconnected in which interact with the neighboring particles by a pair-

wise model (item 3.3). To avoid numerical problems such as the tensile instability, we decided not to consider the weighted average of variables that is connected to the second order derivative of the smoothing function. In case where the number of particles to represent the problem domain is too large it is possible to increase the grid size in order to discard some details in the topography. It could reduce CPU time and still present satisfactory results. The proposed method proved to perform suitable simulations of landslides in wide-areas.

In essence, the depth-Integrated model is a two dimensional model achieved by integrating variables along z direction in general three dimensional model using Leibniz's rule as follow:

$$\int_a^b \frac{\partial}{\partial s} F(r,s)dr = \frac{\partial}{\partial s}\left(\int_a^b F(r,s)dr\right) - F(b,s)\frac{\partial b}{\partial s} + F(a,s)\frac{\partial a}{\partial s} \tag{3.0}$$

3.2 Shallow water equation

The governing equation chosen to perform the flow simulation efficiently is the commonly used shallow water equations. The constitution of shallow water equations is formed by hyperbolic partial differential equations that describe the motion of a fluid below a pressure surface. The shallow water equations are used in studies on the wave movements and movement of fluids whose horizontal dimensions are much larger than the depth (z direction). Many researches use the shallow water equations to describe the flow simulation (e.g. Hagen et al., 2005; Miller, 1990).

Bonet (2005) presented a method based on particles to simulate the flow on land that incorporates its physical characteristics. This method is a variation of the Smoothed Particle Hydrodynamic (SPH) to handle with the Shallow water equations that represents with precision the phenomenon of the flow on lands.

Recently we have developed an efficient flow simulation method that is a kind of depth-integrated particle method (Hoang et al., 2009, Nakata et al., 2012, Zhang et al, 2013). It is suitable for the simulation of long-distance debris flow or the entire geo-hazard evaluation of

very wide area (e.g, 10 km by 10 km) with the detailed topographic information. Another feature of the method is that only two flow parameters are introduced, i.e., Manning coefficient, n, and the critical slope for deposition,i_d.

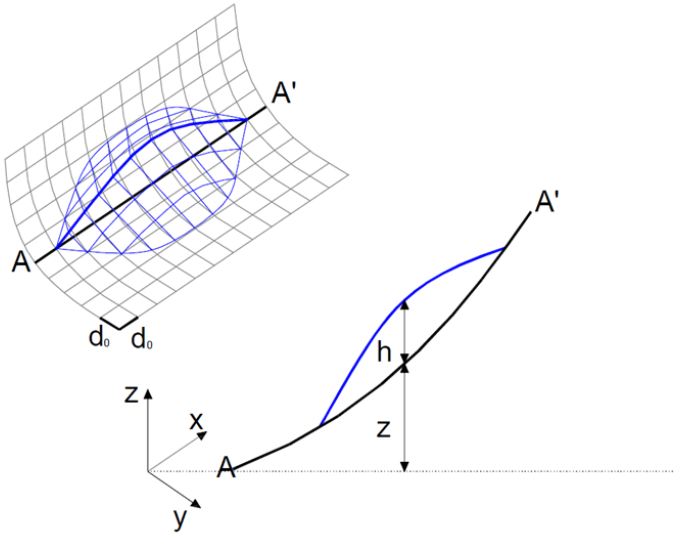

Figure 3.1 Reference system and schematic illustration in the analysis

The basic equations are the commonly-used shallow water equation as follows:

$$\frac{\partial v_x}{\partial t} + v_x \frac{\partial v_x}{\partial x} + v_y \frac{\partial v_x}{\partial y} = g_x - \frac{\partial p}{\partial x} - \frac{\tau_{bx}}{\rho h}$$
$$\frac{\partial v_y}{\partial t} + v_x \frac{\partial v_y}{\partial x} + v_y \frac{\partial v_y}{\partial y} = g_y - \frac{\partial p}{\partial y} - \frac{\tau_{by}}{\rho h} \quad (3.1)$$

where, $v = (v_x, v_y)$ is a depth-integrated flow velocity vector, h is the surface height of debris flow, $\tau_b = (\tau_{bx}, \tau_{by})$ is the bottom shear stress vector, ρ is the density of the debris flow, p is the hydraulic pressure, and $(g_x, g_y)$is the component of gravitational acceleration parallel to the base slope. Note that the mass conservation equation is not necessary in Lagrangian particle methods.

3.3 Hydraulic pressure

The hydraulic pressure concept was used to perform the interaction between the

particles. We molded the soil-water mixture as a several columns whose initial width and height are w_o and h_o, respectively. These columns are deformable, according to the hydraulic pressure modeled by the inter-particles force. However, the volume ($V = {w_0}^2 h_0$,) of each column keeps constant during the simulation. In our research, we assume that the volume of the particle keeps constant during the whole process. The validation of the proposed method can be seen in item 3.8. The pressure difference is only considered from the initial state because the pressure in the initial state is in equilibrium (Figure 3.2 (a)). Consequently, the two neighboring particles will have repulsive force (Figure 3.2 (b)) when the distance d is smaller than the initial distance d_o (d_o is assumed to be equal to the grid size w_0), while they have attractive force (Figure 3.2(c)) when the distance d is greater than the initial distance d_o . Moreover, the two particles further than $2d_o$ is assumed to have no interaction, while the perfect overlap of two particles (Figure 3.2(d)) represents to the double column height ($h_{pair} = 2h_0$); this situation creates the maximum force of repulsion between the particles. It is worth mentioning that even though the particles are perfect overlapped; those particles continue to interact with other neighboring particles.

The particle-type discretization in the hydraulic pressure is modeled by the following inter-particle force:

$$\Delta p_{pair} = (p - p_0)\frac{d}{\|d_0\|} = \rho g (h_{pair} - h_0)\frac{d}{\|d_0\|} \tag{3.2}$$

Where d is the distance vector between two neighboring particles.

In order to consider the effective length, the above model needed to be modified. Then we adopted a particle-type discretization in the hydraulic pressure, by the following inter-particle force:

$$\mathbf{p} = \rho g \nabla h = \begin{cases} -\rho g \dfrac{h_0}{d_0}\left(\dfrac{1-\|\mathbf{d}\|/d_0}{1+\|\mathbf{d}\|/d_0}\right)\dfrac{\mathbf{d}}{\|\mathbf{d}\|} & (\|\mathbf{d}\| < d_0) \\ -\dfrac{1}{2}\rho g \dfrac{h_0}{d_0}\left[\left(\dfrac{\|\mathbf{d}\|}{d_0} - \dfrac{3}{2}\right)^2 + \dfrac{1}{8}\right]\dfrac{\mathbf{d}}{\|\mathbf{d}\|} & (d_0 \le \|\mathbf{d}\| < 2d_0) \\ 0 & (\|\mathbf{d}\| \ge 2d_0) \end{cases} \tag{3.3}$$

where, h_o is the initial height of the debris flow layer, d_o is the bottom size of the debris 'particle' or 'column', **d** is the distance vector between two interacting particles. This equation describes that the repulsive force acts on the two particles closer than the initial distanced_o, while the attractive force acts on the particles further than d_o, based on the hydraulic gradient. Moreover, the two particles further than $2d_o$ is assumed to have no interaction.

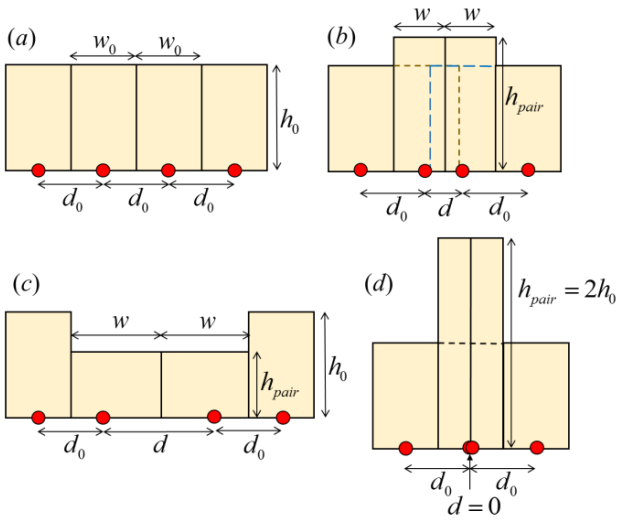

Figure 3.2 Interparticle pressure model used in this study. (a) Initial state in equilibrium, (b) two central particles have repulsive force, (c) two central particles have attractive force, (d) in case two particles are perfectly overlapped

Figure 3.3 shows the relation between the normalized pressure and the normalized inter-particle distance. In the modified model, the maximum distance to occur interaction between particles was set to $2d_o$ which was the established limit to happen the attractive force. However, further analysis showed a not expected behavior for the interactions particles when $d_o \leq d \leq 2d_o$. The problem originated from an error in the code program in which the particles shrank, reproducing an unrealistic attraction force.

Therefore, we attempt to defend the consideration of the use of only repulsive force in the present study. In the proposed new model, we consider the interaction between particles when the distance is less than $1.0d_o$. In other words, the effective influence distance was admitted to be $1.0d_o$ (Figure 3.4). In essence, considering the stability of the simulation, we assume equation 3.4 to model the interaction between particles.

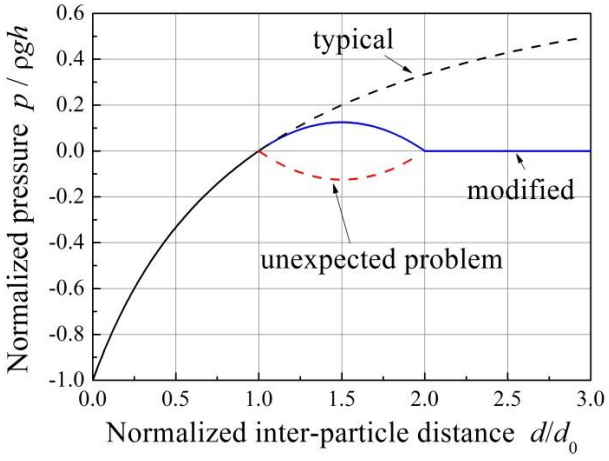

Figure 3.3 Relation between the normalized pressure and the normalized inter-particle distance defined in Eq.(3.3)

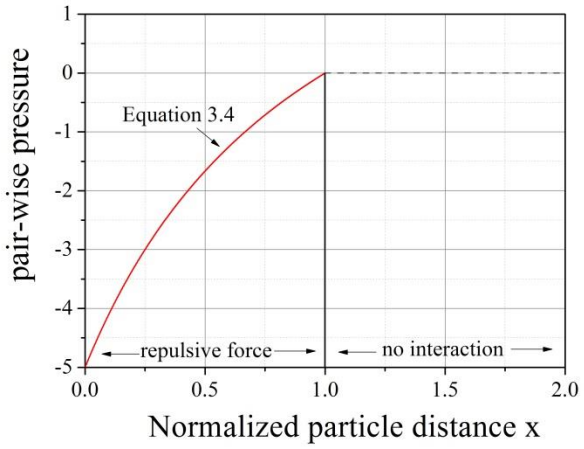

Figure 3.4 Relation between normalized particle distance and pai-wise pressure

$$p = -5\rho g h_o \left(\frac{1 - \|\mathbf{d}\|/d_0}{1 + \|\mathbf{d}\|/d_0} \right) \frac{\mathbf{d}}{\|\mathbf{d}\|} \quad (\|\mathbf{d}\| < d_0) \tag{3.4}$$

3.4 Bottom shear stress

The bottom shear stress is an opposing force to the fluid movement. Basically, the function of the bottom shear stress is retarding the flow.

Zhang et al. (2015) presented the bottom shear stress as a smoothened Bimgham-type relation as follows:

$$\boldsymbol{\tau}_b = \left(\tau_{cr} \|\boldsymbol{v}\|^m + \rho g \frac{n^2}{R_h^{1/3}} \|\boldsymbol{v}\|^2 \right) \frac{\boldsymbol{v}}{\|\boldsymbol{v}\|} \tag{3.5}$$

$$\tau_{cr} = \rho g R_h i_d \tag{3.6}$$

where, n is Manning coefficient, R_h is hydraulic radius (assumed to be equal to the grid size d_o) and i_d is the critical slope angle of deposition. Additionally, a numerical parameter m is introduced for smoothing Bingham fluid model. In the past study, m, that is a numerical model, was adopted as 0.01 to ensure the smooth transition between solid regime and flow regime (Figure 3.5).

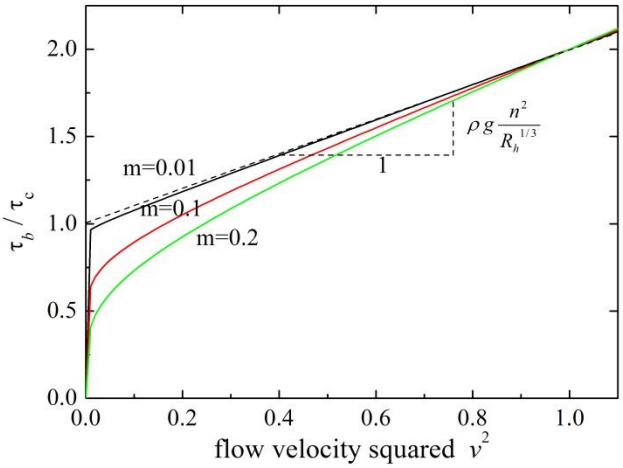

Figure 3.5 Smoothened Bingham-type model for bottom shear stress

However, the elasto-plastic regime was selected on the basis of a representation of the soil flow behavior in our study without a consideration of a numerical parameter to control the smooth transition between solid regime and flow regime. Figure 3.6 presents a sketch of the chosen model.

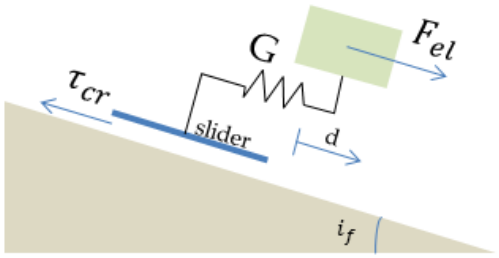

Figure 3.6 Sketch of the elasto-plastic model

$$\boldsymbol{\tau}_b = \left(\tau_{cr} + \rho g \frac{n^2}{R_h^{1/3}} \|\mathbf{v}\|^2 \right) \frac{\mathbf{v}}{\|\mathbf{v}\|} \tag{3.7}$$

where, n is Manning coefficient, R_h is hydraulic radius (assumed to be equal to the grid size d_o), v is the velocity vector, τ_{cr} is the critical shear stress below which the flow speed becomes close to zero and i_d is the critical slope angle of deposition. We expect a movement of the model if $F_{el} > \tau_b$.

$$F_{el} = G.d \tag{3.8}$$

where, G is the shear modulus and d is the strain.

3.5 Manning roughness coefficient, n

To occur a flow, it is necessary to the fluid being influenced by an accelerating force. Once this force is applied, emerges a resistance force in opposition to the previous force and it is primarily responsible to the pressure loss in uniform and gradually varied flow in the contact area between the fluid and the wetted perimeters of a certain locations. This latter force is a function of fluid viscosity and channel roughness. The most used factor associated with roughness in free flow channels is the Manning roughness coefficient. This value is affected by a variety of factors such as the roughness of the wetted perimeter of a channel, deposition of solid particles, presence of obstruction and temperature variations. To determine this value means to estimate the yield strength at a given channel. However, there is no exact method to carry this experience, turning the estimation very complicated. Regarding the typical values for the Manning coefficient for natural streams and minor streams, Chow VT (1959) established a

table of reference (see Table 3.1).

In short, Manning's roughness coefficient represents the resistance to flow of a surface likely to the bank of stream or the bed. In our research, Manning coefficient describes the bottom shear stress acting on the flowing soil-water mixture.

Table 3.1 Typical values for the Manning Coefficient

FLOODPLAINS	MINIMUM	NORMAL	MAXIMUM
a. Pasture, no brush			
1.short grass	0.025	0.030	0.035
2. high grass	0.030	0.035	0.050
b. Cultivated areas			
1. no crop	0.020	0.030	0.040
2. mature row crops	0.025	0.035	0.045
3. mature field crops	0.030	0.040	0.050
c. Brush			
1. scattered brush, heavy weeds	0.035	0.050	0.070
2. light brush and trees, in winter	0.035	0.050	0.060
3. light brush and trees, in summer	0.040	0.060	0.080
4. medium to dense brush, in winter	0.045	0.070	0.110
5. medium to dense brush, in summer	0.070	0.100	0.160
d. Trees			
1. dense willows, summer, straight	0.110	0.150	0.200
2. cleared land with tree stumps, no sprouts	0.030	0.040	0.050
3. same as above, but with heavy growth of sprouts	0.050	0.060	0.080
4. heavy stand of timber, a few down trees, little undergrowth, flood stage below branches	0.080	0.100	0.120
5. same as 4. with flood stage reaching branches	0.100	0.120	0.160

The importance of determining well the Manning coefficient lies in the fact that this value has a great influence in our simulation. We carried out a number of investigations into the behavior of the flow by changing the Manning coefficient. Figure 3.7 compares the results obtained from the sample analysis of a region in Nova Friburgo. The values were set to 0, 0.05, 0.1, 0.15 and 0.2. It becomes clear a relation between the increasing of the Manning coefficient with the decrease in the affected area by the flow. In summary, these results highlight what we previously affirmed: there are greater resistances of the flow for larges Manning coefficient.

A parametric study was used to determine the optimal Manning coefficient for each case

study with the assistance of a simple analysis of the average of the accuracy of the damage area prediction at maximum.

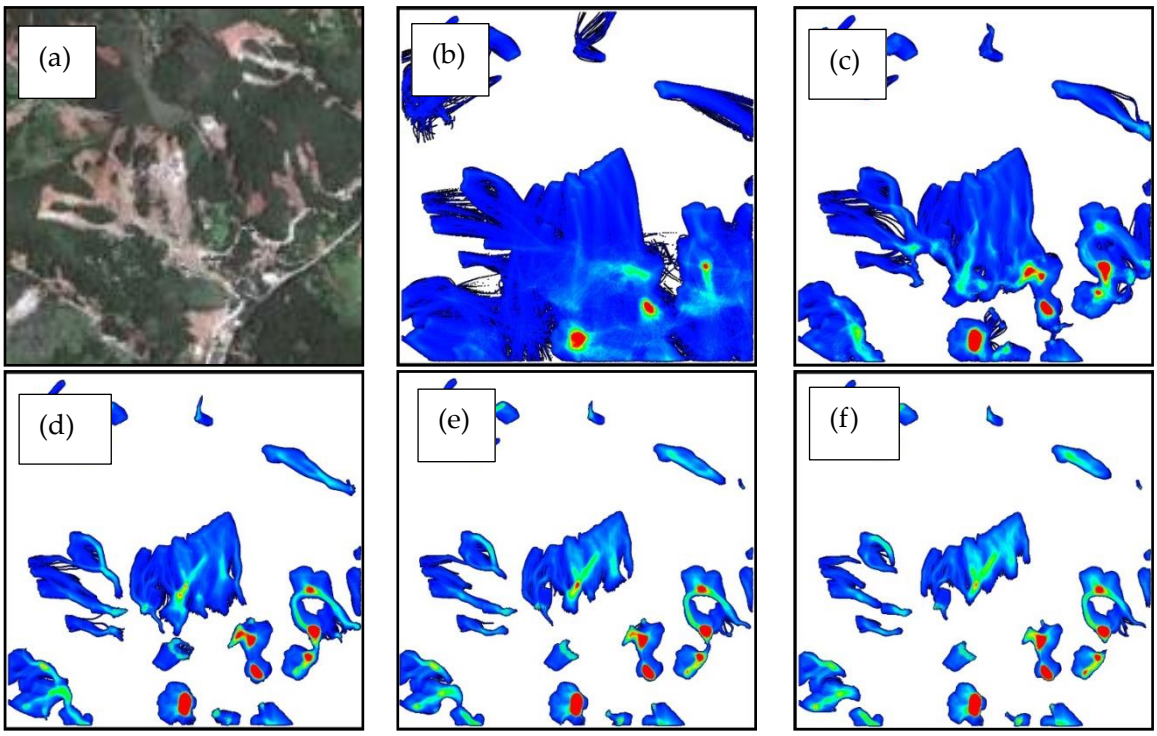

Figure 3.7 Effect of the Manning coefficient in our simulation in an area in Nova Friburgo, (a) Actual damage area, (b) n=0, (c) n=0.05, (d) n=0.1, (e) n=0.15, (f) n=0.2

3.6 Critical angle of deposition, i_d

Also knowing as angle of repose or critical angle of repose is the maximum inclination of a granular material in which the material is stable. This value represents the critical stress for fluid-to-solid transition of the debris flow. It is associated to the coefficient of friction, shape, surface area, density of the particles of the material. A list of different materials and their critical angle of deposition in a dry condition is given by Clover, T. J. (1995), Table 3.2.

Table 3.2 Typical values for the critical slope of deposition for selected soils in a dry condition

Material	Critical angle of deposition
Ashes	40°
Asphalt (crushed)	30–45°
Bark (wood refuse)	45°
Bran	30–45°
Chalk	45°
Clay (dry lump)	25–40°
Clay (wet excavated)	15°
Clover seed	28°
Coconut (shredded)	45°
Coffee bean (fresh)	35–45°
Earth	30–45°
Flour (corn)	30–40°
Flour (wheat)	45°
Granite	35–40°
Gravel (loose dry)	30–45°
Gravel (natural w/ sand)	25–30°
Malt	30–45°
Sand (dry)	34°
Sand (water filled)	15–30°
Sand (wet)	45°
Snow	38°
Urea (Granular)	27°
Wheat	27°

By adding some water in the selected soils, the cohesion increases. This action allows a steeper critical slope of deposition. However, by adding more water, the soil becomes more saturated until the cohesive forces take apart and the water acts like a lubricant. Oficina de textos (2000) related characteristics of the fluid and the critical angle of deposition (Table 3.3).

Table 3.3 Characteristics of the fluid (Oficina de textos, 2000)

Type of process	Critical angle of deposition i_d
Grain flow or sand flow	18° to 25°
Debris flow or mud flow	5°
Quick sands	0°
Turbidity current	0°

Only for illustration purposes, we carried out a number of investigations into the behavior of the flow by changing the critical slope of deposition. Figure 3.8 compares the results obtained from the sample analysis of a region in Nova Friburgo. The values were set to 0, 1, 2, 3 and 4. It is possible to visualize a minimum influence of the critical slope of deposition for angles between 0 and 4. This is in agreement with the disaster survey result in general (Takahashi, 2004).

As well as to investigate the optimal Manning coefficient to our research areas, a parametric study was used to determine the optimal critical slope of deposition for each case study with the assistance of a simple analysis of the average of the accuracy of the damage area prediction at maximum.

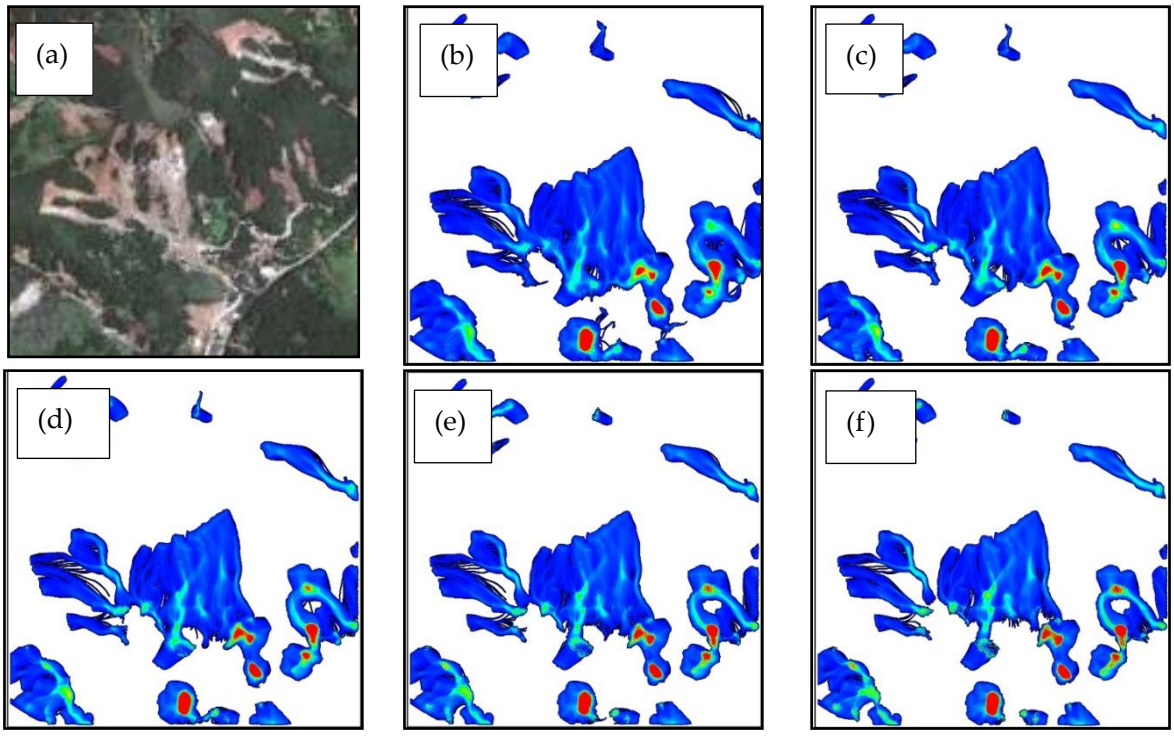

Figure 3.8 Effect of the critical angle of deposition in our simulation, (a) Actual damage area, (b) i_d=0, (c) i_d=1, (d) i_d=2, (e) i_d=3, (f) i_d=4

3.7 Critical slope for failure, i_f

Critical slope for failure i_f represents the yield strength of the soil in the initial solid phase. Figure 3.9 shows a random area where it is possible to distingue three different critical angles for failuresi_f: a) indicates 22314 dangerous location for i_f = 30 (deg.), b) reflect 9364 unstable locations for i_f = 35 (deg.), c) indicates 4542 dangerous location for i_f = 40 (deg.), d) presents1792 unstable places for i_f = 45 (deg.).

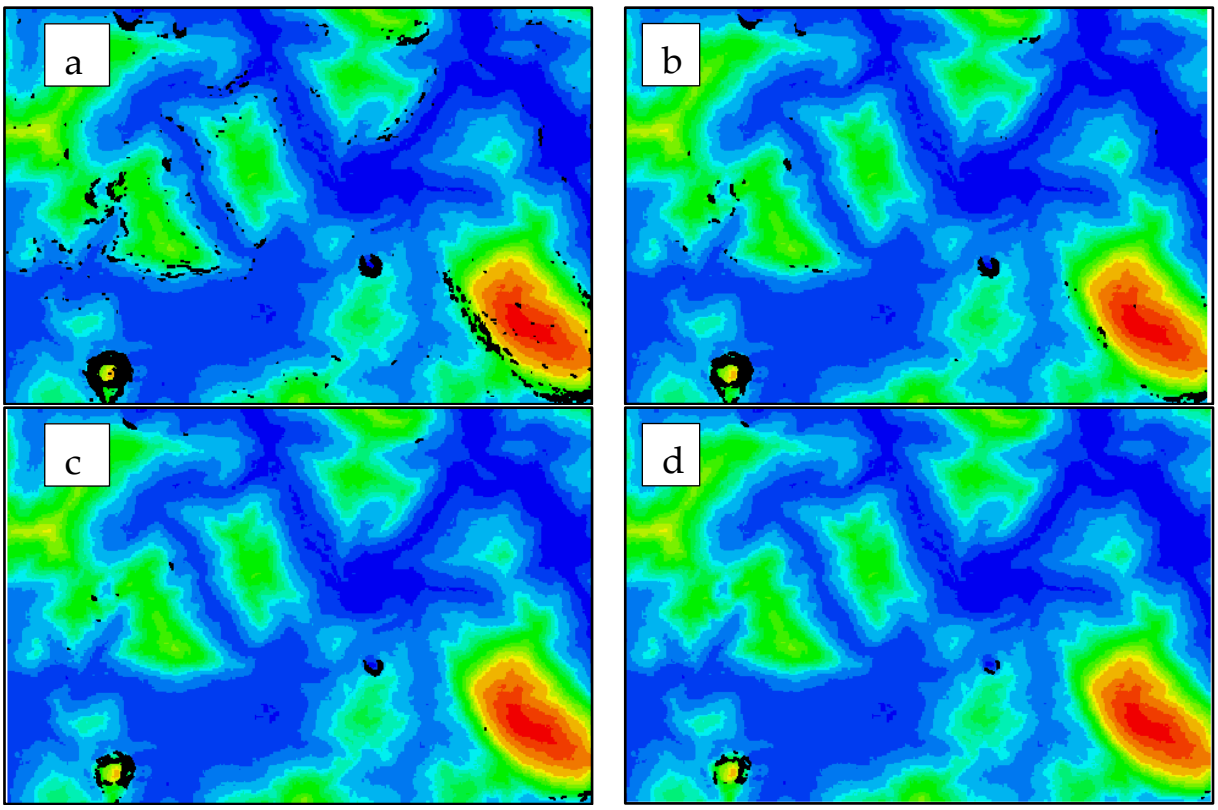

Figure 3.9 Effect of the critical slope for failure, (a) i_f=30 (deg.), (b)i_f=35 (deg.), (c) i_f=40 (deg.), (d) i_f=45 deg.)

The election of a good critical slope of failure i_f guarantees a reasonable result for the simulations of landslides.

3.8 Validation of the numerical model in a simplified geometry

A series of cases verifications were performed with different coefficients to find the

model that best adapts the requirements of the new proposed particles interactions. To do so, a 1D V-shape deposition problem (Figure 3.10) was used as the basis for succeed in study the parameters, height of the final sediment surface and volume storage stability.

The flow simulation was performed according to the equation of motion in a one-dimensional slope named V-shape, in which 55 flow particles with 1.0 m height each, were proportional distributed (Figure 3.10) in a slope with 19.7 (deg), Manning coefficient and critical slope of deposition equal to 0.1 and 0 (deg), respectively based on the proposed validation by Zhang et. al. (2015). The assumption of the conservation of the particles volume is verified and showed in Figure 3.10, where it is possible to see the final deposition height of the flow, which had a satisfactory agreement with the theoretical height. Therefore, it is possible to conclude that the simulation keeps the volume unchanged throughout the simulation.

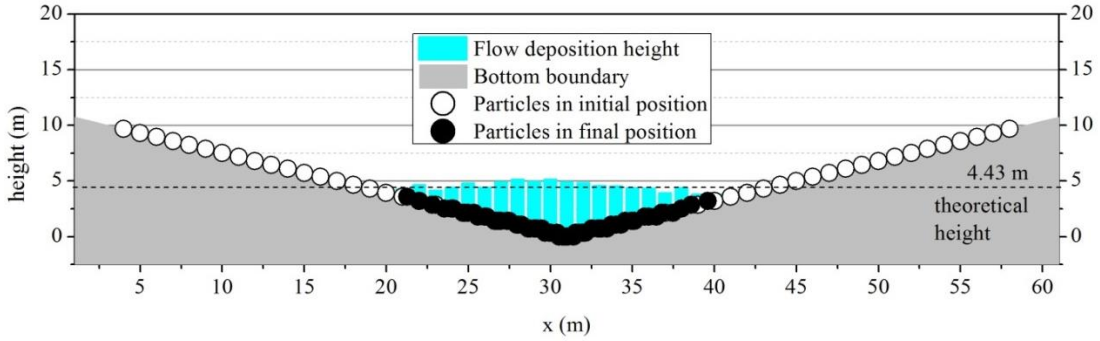

Figure 3.10 Validation of the proposed method in a simplified geometry

As well, we have utilized the before mentioned validation to analyze the behavior of the soil-water mixture by changing the critical angle of deposition, i_d. Figure 3.11 compares the simulation with two different critical angles of deposition: 15 and 19.7 (deg). The result suggests an expected behavior of the flows which were confirmed by the simulation in a simplified geometry. Therefore, the proposed method seems appropriate to perform the conduct of the flow.

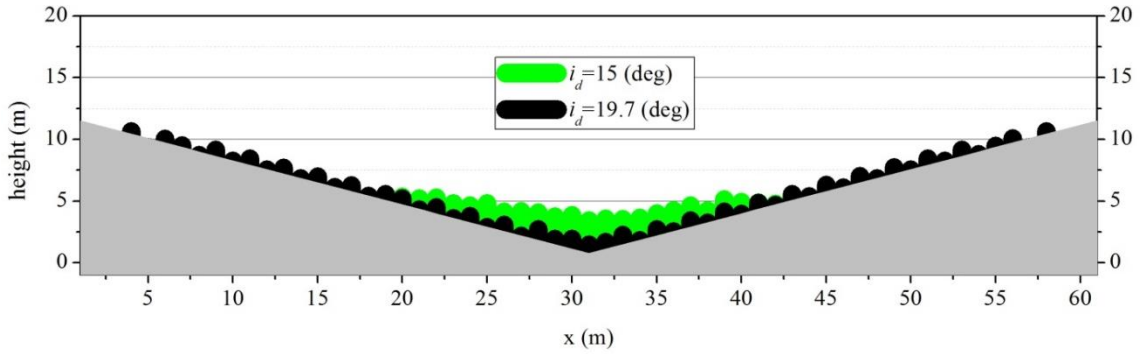

Figure 3.11 flows in 1-D simplified geometry by changing the critical angle of deposition

3.9 Accuracy of the flow simulation

For this study, the simulated damage area is called A_s. The coverage for this nomination takes into account not only the initiation area but also the flow and the deposition area (Figure 3.12). The simulation is modeled by computational particles (item 3.3) which represent the mass of soil-water mixture after failures were placed onto the area. Then, those particles moved down the slope according to the equation of motion (Eq. 3.1) as shown in Figure 3.14, and finally deposited at the bottom of the slope (Figure 3.15).

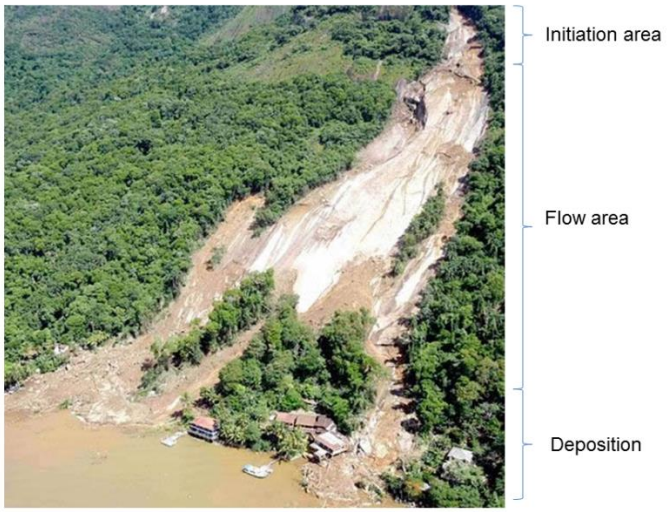

Figure 3.12 Scheme of the constituent parts of the landslide

The simulated affected area of soil mass flow is defined by the area in which the soil mass particles pass through during the flow. Figure 3.15 shows the resulting affected area. This simulation result is compared with the actual landslide scars (Figure 3.17) detected from the satellite image. Figure 3.18 shows the overlapped area (in black) between the two.

We performed the flow simulations in the entire region of interest and computed the total accuracy for different material parameters set (i_f, n, i_d) using a statistical evaluation. Such analysis helps us to determine such sensitive parameters in a reasonable way.

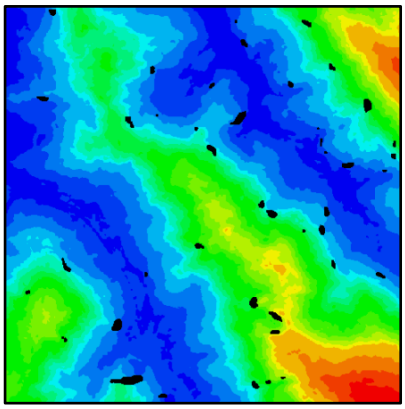

Figure 3.13 Soil particles in initial position

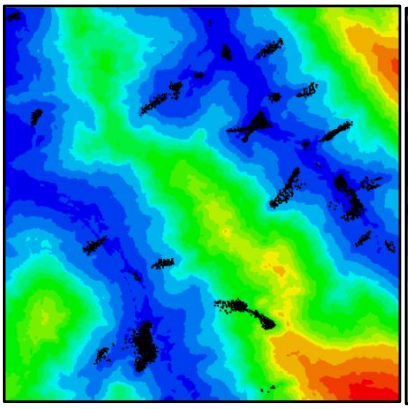

Figure 3.14 Soil particles in motion

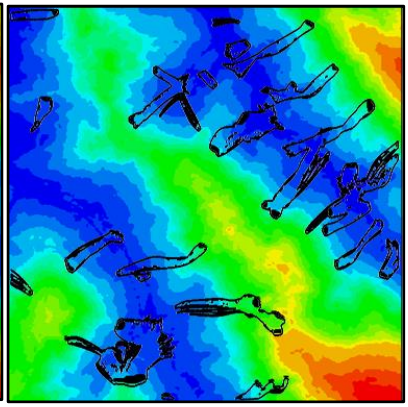

Figure 3.15 Simulated damage area A_s

Figure 3.16 Actual damage area (Google Earth)

Figure 3.17 Landslide-scars of the actual damage area extracted from the image binarization

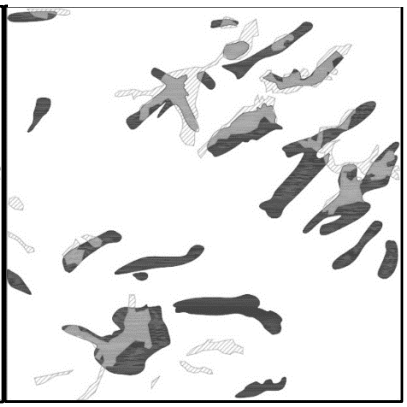

Figure 3.18 Overlapped areas: simulated affected area in black, and actual damage area in stripes. The intersection formed by the two areas is represented in gray

The equation was based on the intersection between the Actual damage area A_a and the Simulated damage area A_s, classified in this study as a True Positive (TP) results. The accuracy of the simulation, a_c, is then defined by the ratio of overlapped area to the union of the two areas, Eq. 4.1.

Other key performance to be considered is the False Negative (FN) results (Eq. 4.2). The evidence from this study suggests that the false negative is particularly useful in indicating simulations where the simulated damage area A_s were over-estimated. A natural increase in the false negative results is accompanied by the increase of the simulated damage area A_s. Thus, the greater is the false negative, the smaller is the intersection areas.

It was noticed that the key indicators true positive, false negative and false positive complement each other and each of them can be used for a specific purpose. In order to validate the efficiency of the proposed landslide simulation, we will use the key performance classified as a True Positive results.

$$a_{c,true\ positive} = \frac{A_a \cap A_s}{A_a \cup A_s} \tag{4.1}$$

$$a_{c,false\ negative} = \frac{(A_a \cup A_s) - A_a}{A_a \cup A_s} \tag{4.2}$$

$$a_{c,false\ positive} = \frac{(A_a \cup A_s) - A_s}{A_a \cup A_s} \tag{4.3}$$

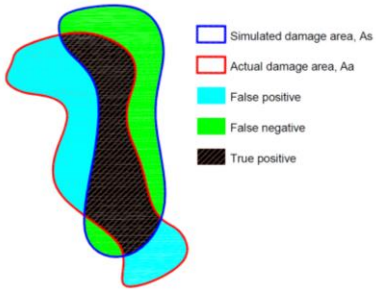

Figure 3.19 Definition of true positive, false negative and false positive key performances

3.10 Grid size

3.10.1 Overview

Recent advances in our proposed method given the current status of embedded information, we desire the refinement of study of the grid size applied in our simulation. Our focus is not on whether the accuracy of the flow simulation, but rather on proposing a study of the effect of the grid size in our research.

In this chapter, it should be noted that our method is derived from the evaluation of the mentioned cases studies in Chapter 5 and 6. For the Rio de Janeiro's case and Hofu's case studies the grid size set was 5.0 m. Our objective here is to discuss the difference between both cases and demonstrate the exploration of a new one: 1.0 m.

The image with a spatial resolution equal to 1.0 m from Hofu city was kindly provided by the CRDB (Chugoku Regional Development Bureau – Yamaguchi Branch).

3.10.2 Evaluation of grid size

Based on several tests performed beforehand, we are able to affirm that the grid size is an important driving factor of the accuracy of the flow simulation and in the maximum velocity of the flow. The causes have been discussed below:

- Accuracy of the flow simulation: Grids with larger size dispense the details in the topography. In some cases, it is essential to consider all topographic information to have a landslide simulation close to the real situation.
- Maximum velocity of the flow: A grid with a bigger size has a lower detailed topography, which implying a minor disturbance of the flow. Moreover, the size of particles is set to equal the DEM grid size, which means the greater the grid size, the greater the particles size will be, however, with smaller number of particles to interact, which can reduce the shear stress in the bottom.

The maximum velocity of the flow is an important feature to validate the proposed method: facing unrealistic results it is possible to discard some grid sizes. The effect of the grid

size can be faced in Figures 3.20.

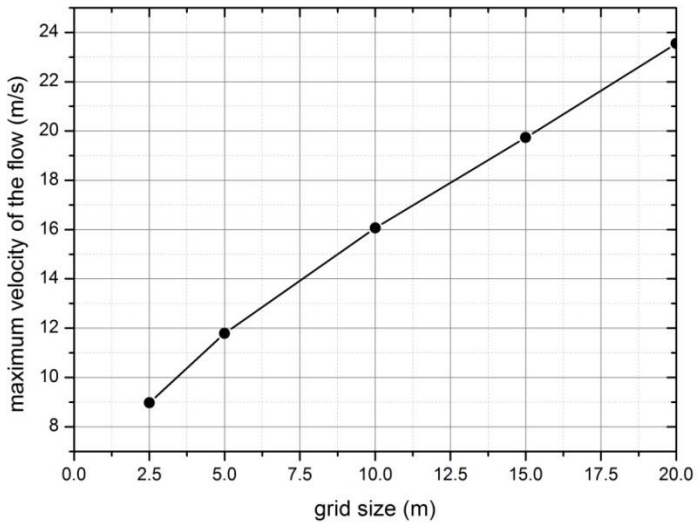

Figure 3.20 Relationship between the maximum velocity of the flow and the respective grid size

The results of the correlational analysis between the grid size (i.e. 2.5 m, 5.0 m, 7.5 m, 10.0 m) and the slope gradient can be compared in Figures 3.21-3.24. It is apparent from these results that the grid size has a direct impact on landscape representation; the smaller the grid size, the greater is the percent of steeper slopes. This tendency is more clear in Figure 3.25. where the relation between the slope gradient and its cumulative frequency is plotted for different grid sizes. Similar findings were reported by Jenson (1991), Panuska et al. (1991) and Zhang et al. (1994).

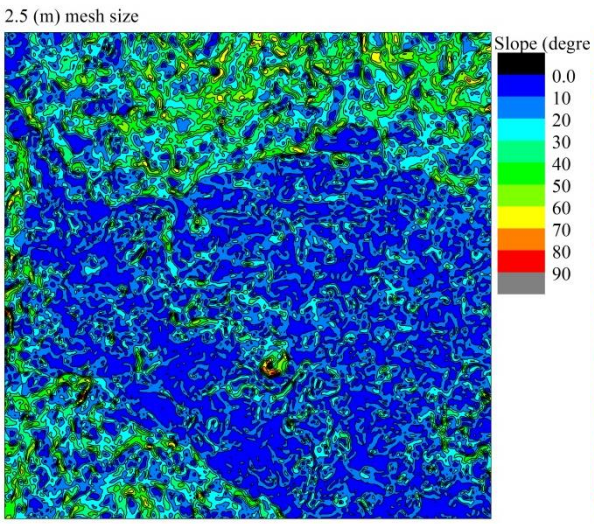

Figure 3.21 Effect in the topography when the grid size is 2.5 (m)

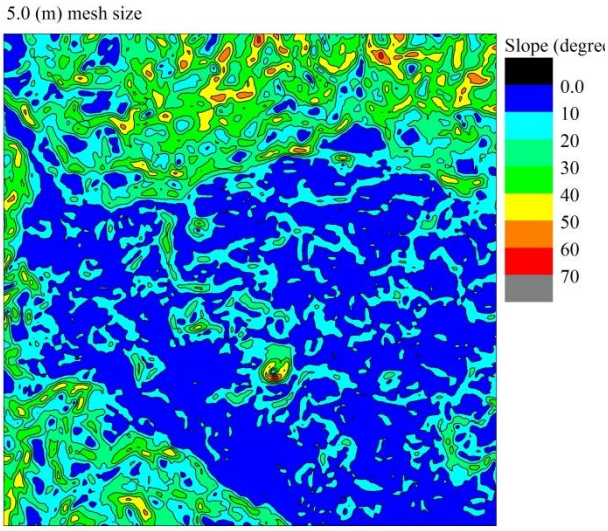

Figure 3.22 Effect in the topography when the grid size is 5.0 (m)

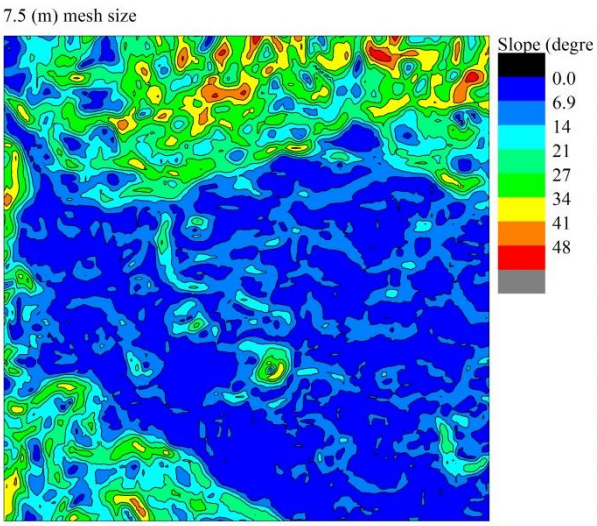

Figure 3.23 Effect in the topography when the grid size is 7.5 (m)

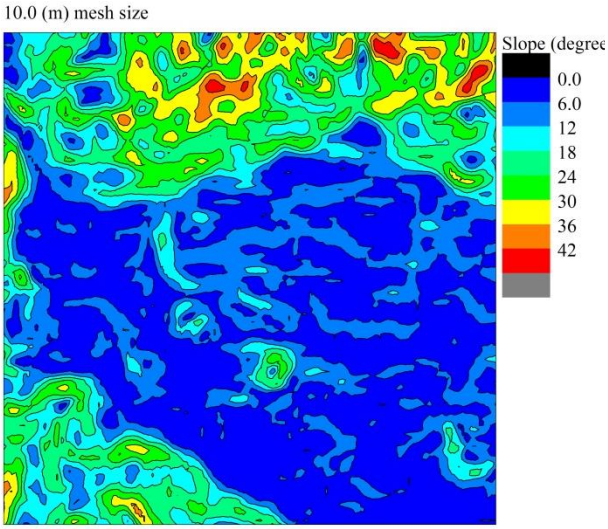

Figure 3.24 Effect in the topography when the grid size is 10.0 (m)

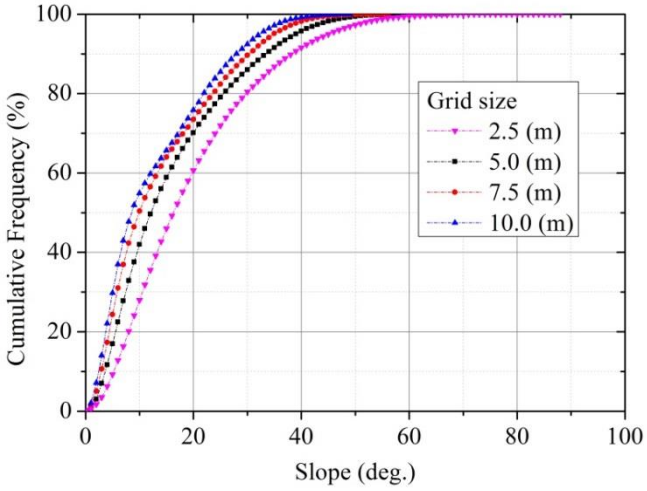

Figure 3.25 Cumulative slope distribution for 4 different grid sizes

Here, we would like to explore the effect of the grid size in the accuracy of the flow simulation. To do so, we chose a small area in Nova Friburgo measuring 1125 m by 1680 m. It is located in the portion Northeast in our current research.

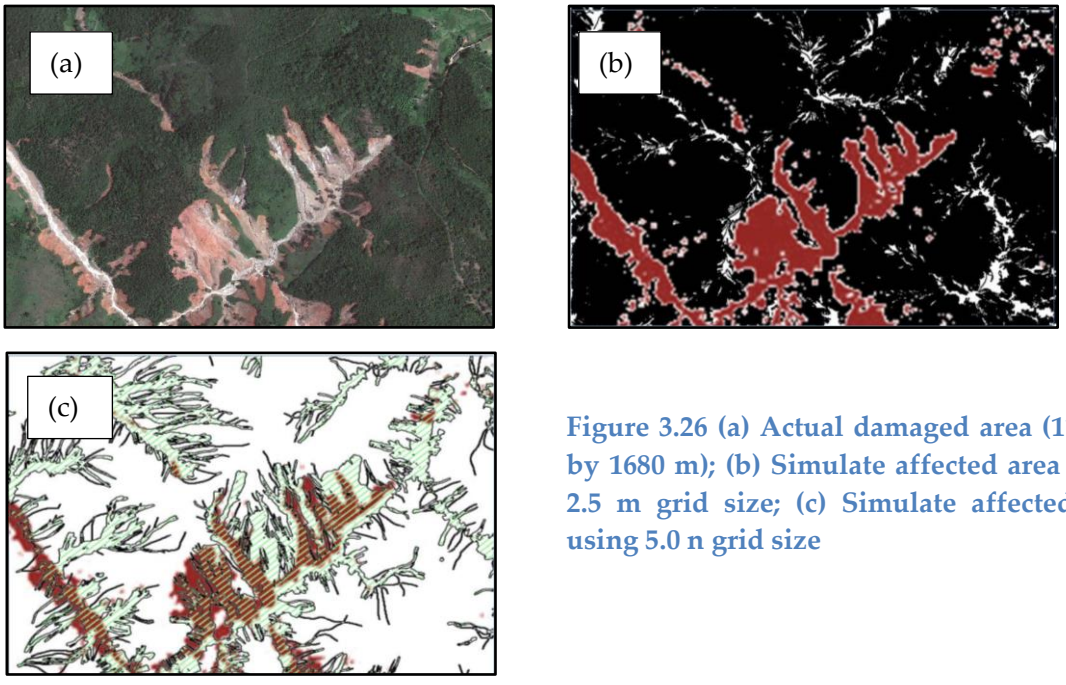

Figure 3.26 (a) Actual damaged area (1125 m by 1680 m); (b) Simulate affected area using 2.5 m grid size; (c) Simulate affected area using 5.0 n grid size

In order to simulate in the previously mentioned area, we set the same condition for both cases: $i_f = 32$ (deg), n=0.1, i_d=0 (deg). Figure 7.7 (b) present the result when using a grid size equal to 2.5 m; the area in black solid represents the affected area by the landslides A_s, while the brown area represents the actual damaged area A_a. It is possible to see how the simulation model over-estimates this area using the established conditions. Figure 3.26 (c) shows a Simulate affect area A_s, represented by the green dashed hatched area; here, there was a decrease in the over-estimation subject, although it is still possible to see places with over-estimated areas. For the case using 2.5 m grid size the accuracy of the flow simulation a_c is 13.24 (%), while for the case using 5.0 m grid size, the accuracy of the flow simulation a_c is 30.82 (%). Therefore, for this area with the established conditions presented here, the best result was found while using a grid size with 5.0 m.

3.10.3 Conclusion of the effect of the grid size in this simulation

It is well know that the DEM is important to define the slope and the landscape representation. These items directly interfere in the velocity of the flow and in the accuracy of the flow simulation, as we already mentioned. The mesh sizes therefore need to be interpreted with caution.

After several analysis using a grid size measuring 2.5 m and 5.0 m, the result suggest that it is possible to have approximate values for the accuracy of the flow simulation using different grid sizes. However, it is necessary to modify the smoothness of the landscape representation in order to obtain such approach. It is necessary further study in order to interpret the smoothness issue. Therefore, this subject was not mentioned in this study and will be discussed in the next researches.

Also, this study set out with the aim of assessing the importance of considering a reasonable computational time. Only to exemplify: when we analyzed that area using a 2.5 m mesh, the computational time was 14 hours and 32 minutes to compute 125.149 particles within an area equal to 450 pixels by 672 pixels. However, to analyze the same area using a 5.0 m mesh size, it took 18 minutes to perform 4.617 particles. The present study was designed to

perform a landslide simulation in a non-complex assignment. Therefore, the computational time should be considered as an important issue to suit the proposed needs.

4. FLOW SIMULATION FOR EVALUATING DAMAGED AREA IN RIO DE JANEIRO

4.1 Landslides in Nova Friburgo, Rio de Janeiro (Brazil)

In the state of Rio de Janeiro, disasters related to mass movement correspond to 140 events that were recorded from 1991 to 2010 (Atlas Brasileiro de desastres naturais, 2011)

According to the NADE 2010 (Nucleo de Analise e Diagnostico de Escorregamentos), the state of Rio de Janeiro was classified by its landslide risk assessment during november and december of the same year. Data from this classification has identified Nova Friburgo as one of the potential very high risk of landslides. Predisposing factors (i.e. geology, geomorphology, surface hydrology and hydrogeology, and climate) together with effectives factors (i.e. occupation of the soil, record rainfall, erosion) and triggering factor (i.e. torrential rain) are responsible for landslides in Rio de Janeiro.

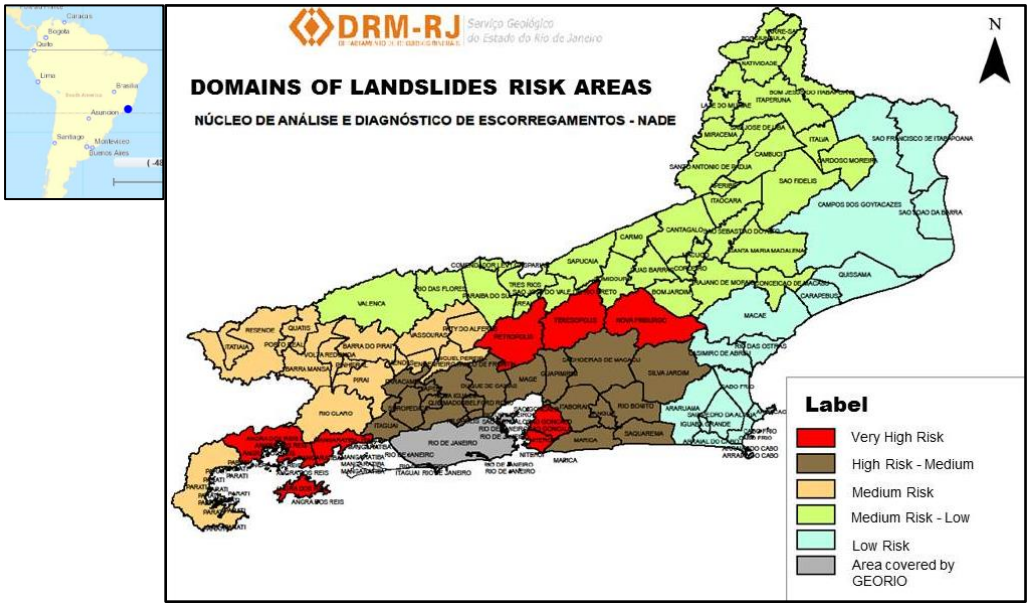

Figure 4.1 Domains of landslides risk areas in Rio de Janeiro

Nova Friburgo is located in the Southeast region in Brazil, we chosen as a case study. Brazil has been suffered with extreme events of landslide caused by heavy rain, specifically in Rio de Janeiro, where the accentuated topography and the tropical climate contribute to the occurrences of landslides. This is an annual concern during summer season (from October to March). Torrential rain in Brazil has been known to lead to high death tolls in a general way because homes are often constructed in dangerous locations (Figure 4.3) that are vulnerable to landslides. Accordingly, landslide-induced disaster is the one that most cause fatalities, representing 60% of the total in this category (Nobre, 2011).

In accordance with "official documents of the state of Rio de Janeiro, 2011", the summer season represents the highest frequency of mass movement in the state between 1991 and 2010. Figure 4.2 shows that January has the highest frequency of mass movement (46 occurrences) followed by December (37 occurrences).

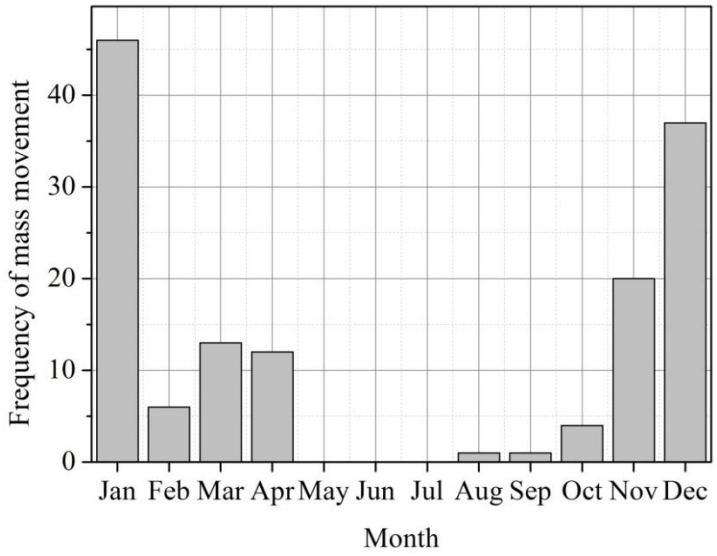

Figure 4.2 Frequency of mass movement per month

The conditioning factors to the mass movement correspond mainly to the high rainfall, erosion by water or wind, level of oscillation of lakes and seas and groundwater, action of animals and humans. Human action has an important influence on the occurrence of mass movement. Among the causes it is possible to mention the vegetation removal, garbage accumulation, construction of houses on the slopes, the leakage of water and sewer, etc.

Figure 4.3 Homes constructed in dangerous location in Nova Friburgo, Rio de Janeiro

According to Figure 4.4, the number of affected people reached 747.372. In addition, 28.389 people were dislodged, 16.136 people turned to homeless, 5.639 were displaced, 41 are still missing, 86 were slightly injured, 645 were infirm and 395 people died.

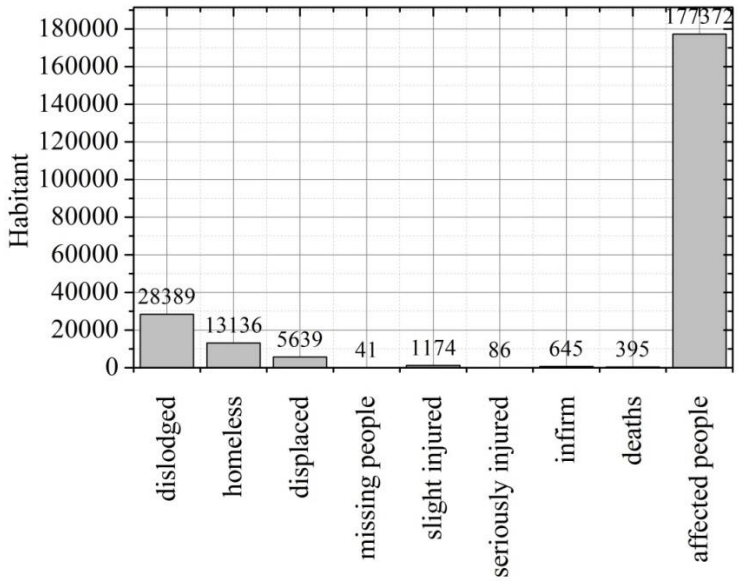

Figure 4.4 Number of people reached directly or indirectly by landslides

Our case study area had around 10% of its mountainous area destroyed due to several landslides triggered by heavy rain in 2011. According to Coelho et al., 2011 (Figure 5.3) the accumulated volume in all rainfall stations overtook values expected for monthly rainfall in

under than10 hours. GEO-RIO foundation (d'Orsi et. al 2004) declared a rainfall precipitation around 30mm/h or 70mm/24h or 100mm/96h as rainfall intensities that initiate failure process in Rio de Janeiro. Basically, the mountains and hills in this area are composed of rock, saprolites and colluvium. An earlier study (Avelar, et al 2011) mentioned that the rupture surface is located within the saprolites or along the interface between the soil (with depth bewteen 0.5 and 2 m) and bedrock. Figure 4.10, Around 80% of the entire area is formed by slopes with less than 20 (deg.) and quotes elevation between 850 (m) to 1350 (m), (Figure 4.9).

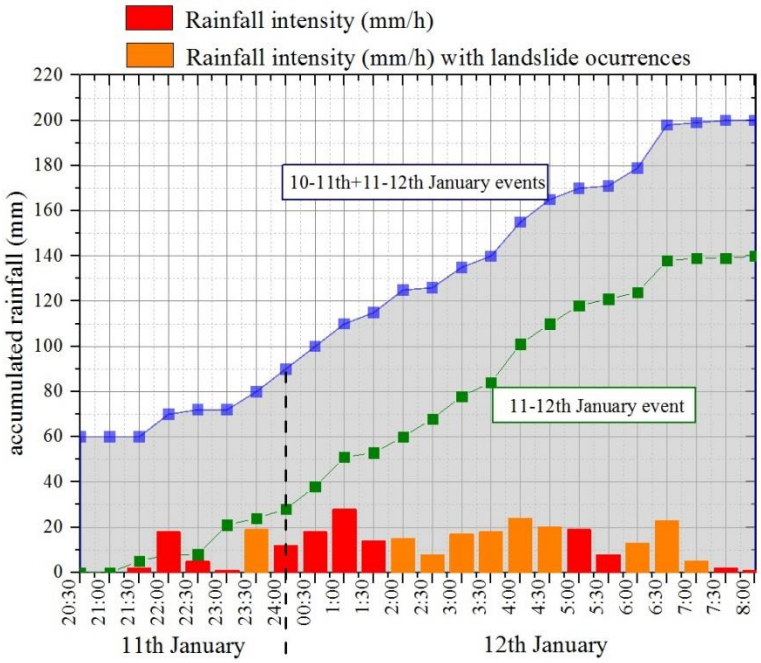

Figure 4.5 Accumulated rainfall curve and rainfall intensity in Rio de Janeiro (Coelho et al., 2011)

Figure 4.6 provides the satellite image of the research area in Nova Friburgo (6,72km by 4,5km) taken before the disaster. The landslides scars were extracted from the damaged area (Figure 4.7) by the image binarization. The threshold of the binarization was determined by using an image composition program. The implementation consists of determining a range of colors related to the landslides scars, which was determined with values between 131 and 255. After several analyses, we confirmed that the selected threshold values represented well the landslides scars. The result is show in Figure 4.8.

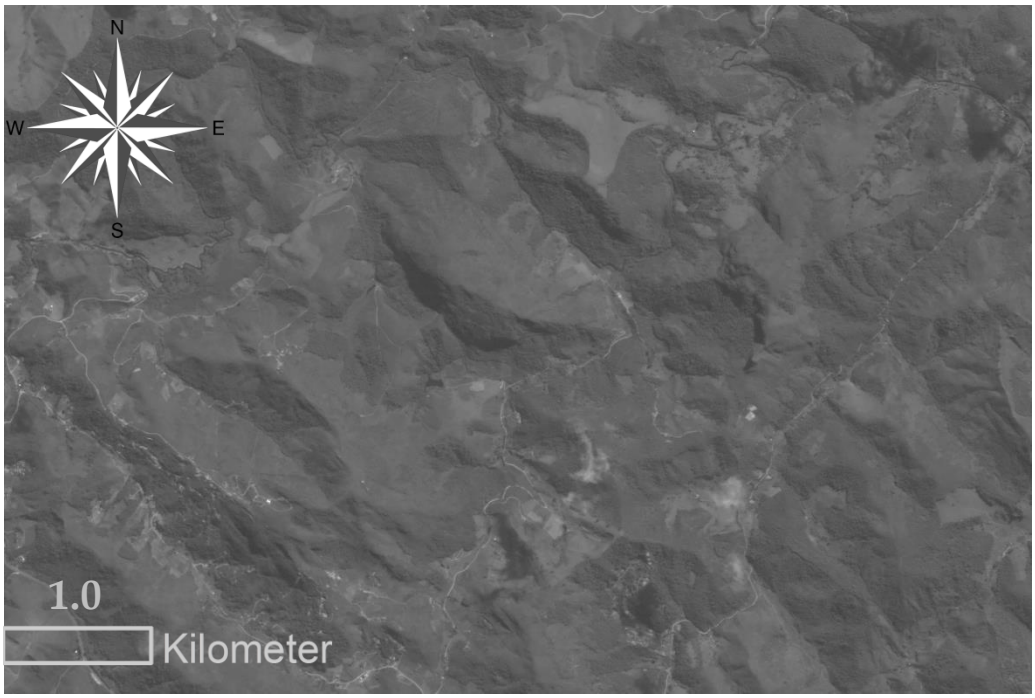

Figure 4.6 Satellite image of the researched area in Nova Friburgo, Rio de Janeiro

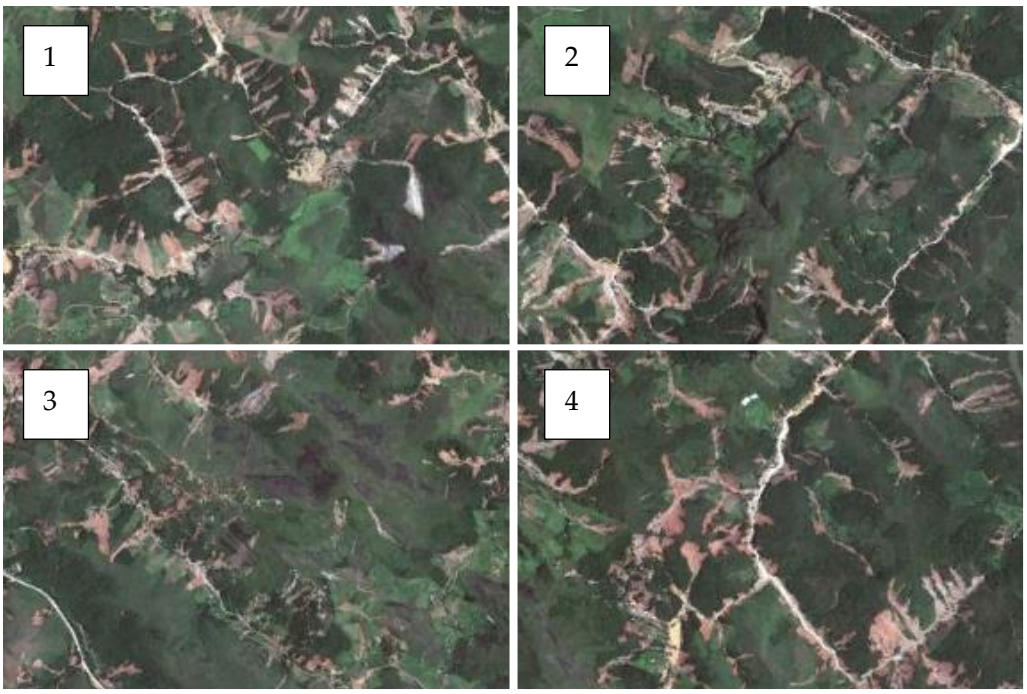

Figure 4.7 Researched area after the disaster on January 11-12th 2011. The grids show the discretized domain for flow simulation

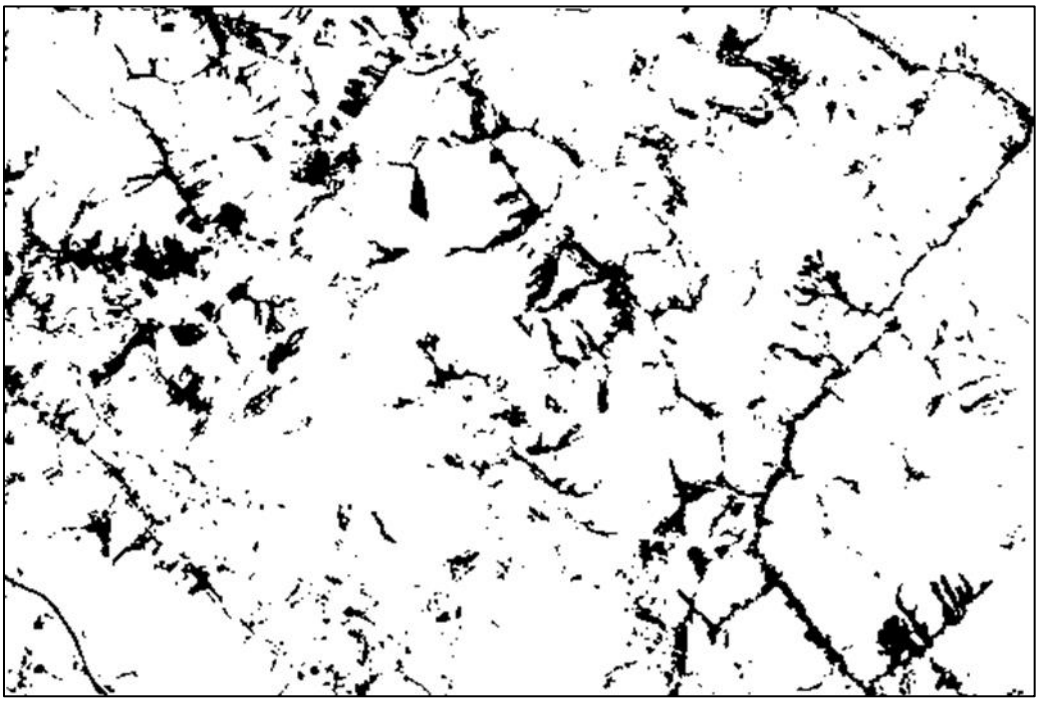

Figure 4.8 Landslides scars extracted by image processing

The relative frequency of the elevation for each case study area is shown below. It is possible to notice that the four areas have similar representations. These associated characteristics are verified in the slope cumulative frequency graph (Figure 4.10), in which shows similar results for the chosen areas.

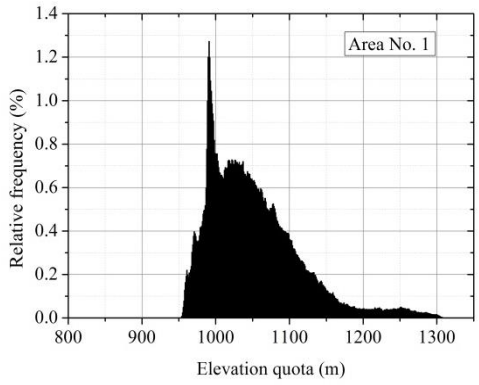

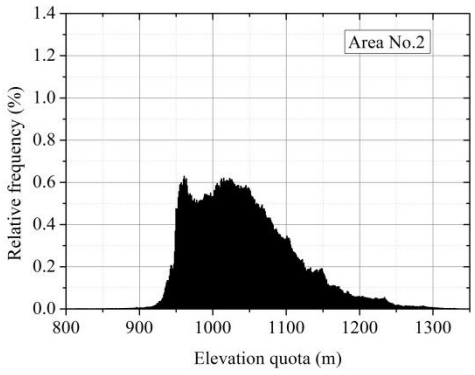

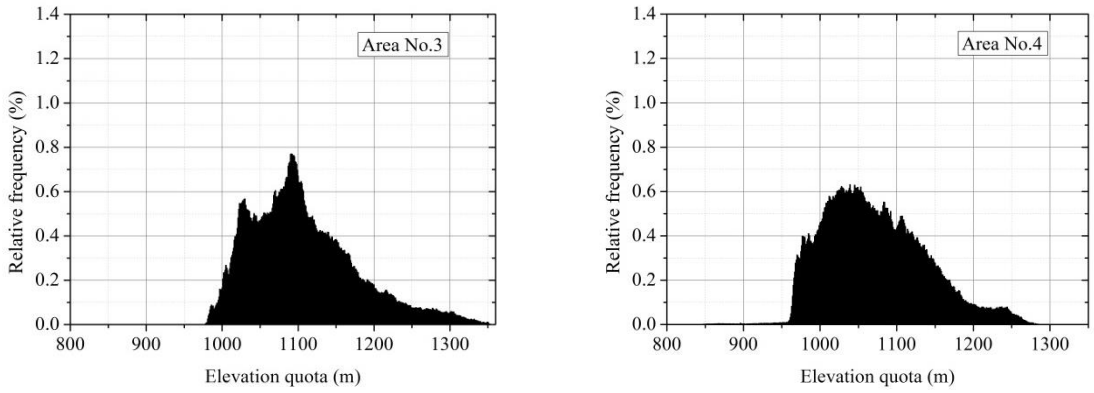

Figure 4.9 Relative quota elevation in Nova Friburgo for each area

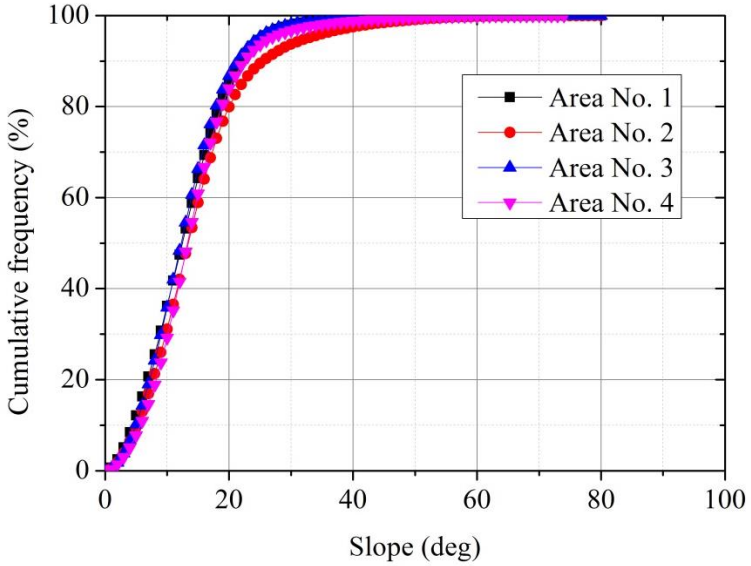

Figure 4.10 Slope cumulative frequency in Rio de Janeiro

4.2 Evaluation of failure slopes

In an analysis of the mechanisms of the landslides in the mountainous area of Rio de Janeiro, Avelar et al. (2011) drew a typical geological profile for this region. Avelar describes four soil types for the composition of the predominant type of slope (i.e. grey saprolite, pink saprolite, slope colluvium and valley bottom colluvium).The failure surface is found among 0.5 to 2 meters. Therefore, we assumed the surface soil depth as 2 meters.

Table 4.1 Mechanical properties of the surface soil in the research area in Nova Friburgo

Soil type	Specific gravity	Void ratio	Friction angle (deg.)	Cohesion (kPa)
Valley bottom colluvium	2.693.	0.97-1.21	42	6
Slope colluvium	2.664	1.16-1.61	38.3	0
Pink saprolite	2.858	0.77-0.80	38.6	25
Gray saprolite	2.650	0.95-1.03	36.7	25

One of the difficulties in predicting landslides disasters originates from the complexity in reproduce exactly all the soil layers. It is well know that the mechanical properties of surface soil and other components differ and different places. In order to overcome such complexity, we examined the four soil types mentioned by Avelar et al. (2011). The relationship between the critical slope for failure i_f and saturated soil height h_2 determined when the $F_s = 1$ in Eq. 1.5 for the reported soil types is showed in Figure 4.11.

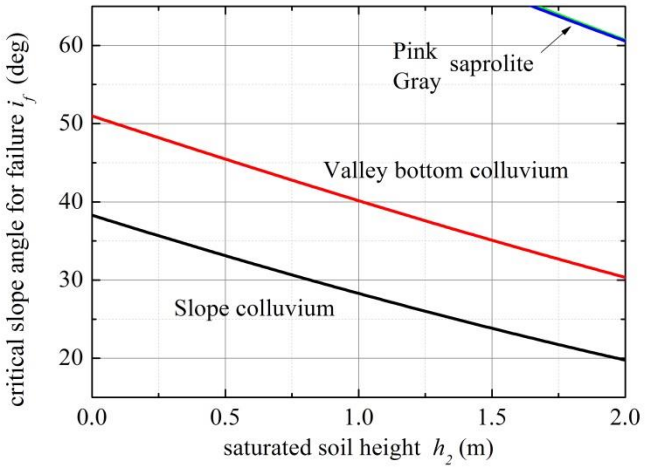

Figure 4.11 Relationship between the critical slope angle for failure and its saturated soil height

In order to simplify the complexity in case we have to consider all soil layers, we first assumed the most fragile soil (i.e. slope colluvium) when considering the stability of the slope as a function of the soil saturation. Five critical slope angles for failure, i_f, emerged from the analysis of instability of the slope and its relation with the soil saturation, those angles are: i_f=38 (deg), i_f=33 (deg), i_f=28.5 (deg), i_f=24 (deg) and i_f=19.7 (deg), which make correspondence

to the saturated soil height h_2 0.0 (m), 0.5 (m), 1.0 (m), 1.5 (m) and 2.0 (m), respectively. However, we do not discard to consider the valley bottom colluvium soil as well.

A complementary way to evaluate the critical slope angle for failure i_f, consists in overlapping areas of slope distribution and actual damaged areas A_a (Figures 4.12-4.15) to search for a relationship between both. It is not expected an easy and clear evaluation as we ignore a series of complex items to make this landslide model simulation more convenient.

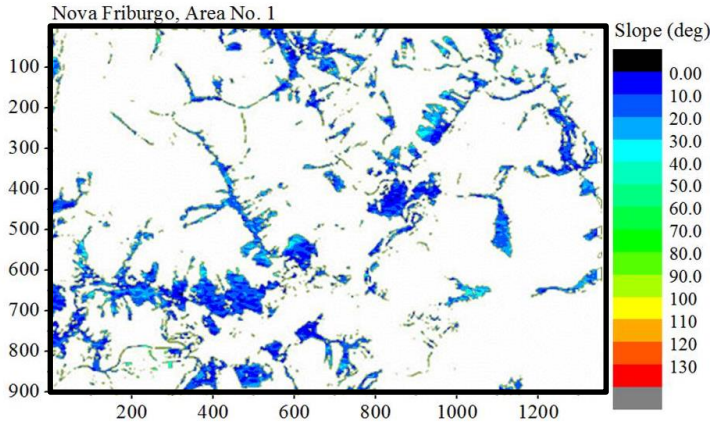

Figure 4.12 Slope distribution in Nova Friburgo with actual damaged area overlapped, Area No. 1

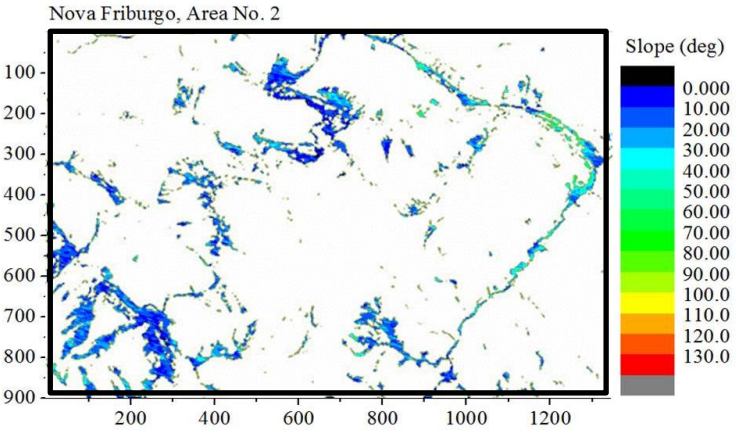

Figure 4.13 Slope distribution in Nova Friburgo with actual damaged area overlapped, Area No. 2

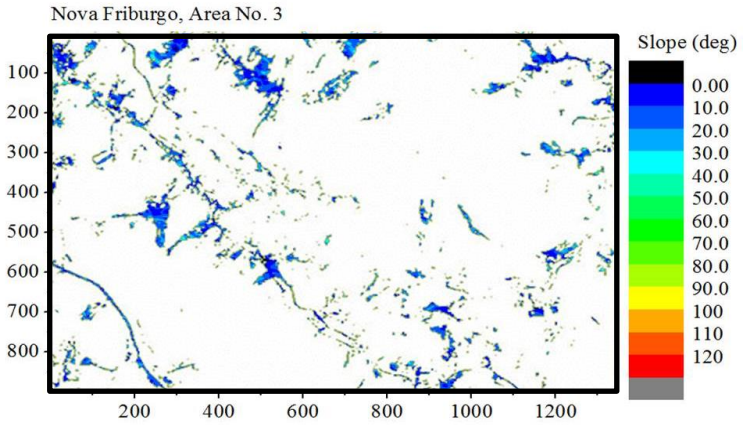

Figure 4.14 Slope distribution in Nova Friburgo with actual damaged area overlapped, Area No. 3

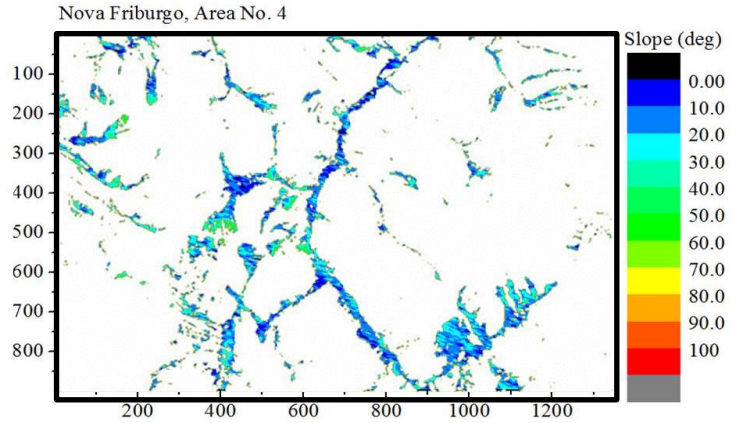

Figure 4.15 Slope distribution in Nova Friburgo with actual damaged area overlapped, Area No. 4

4.3 Flow simulation for evaluating damage area

Once the critical slope angles for failure i_f were determined, we added numerical particles described on item 3.3 and perform flow simulations according to Eq. 3.1. The size of the particles is set to equal the DEM grid size that is 5.0 (m).

Particularly, to reproduce a landslide demands the mechanical properties of the rapidly flowing soil-water mixture, which are quite difficult to obtain before failure. Our method

reduced the number of needed parameters to the previous mentioned set (i_f, n, i_d), which the optimal values were statistical evaluated in the entire research area.

The researched area located in Nova Friburgo measures 6,72km by 4,5km. This area was reached by several landslides. The total numerical particles exceeded the computational limitation (up to 400000 particles). Therefore, it was needed to divide in 4 small areas in which were discretized in Figure 4.7.

Just for illustration purposes, we offer the flow simulation for the entire case study area with the parameters set to 30 (deg), 0.1 and 0 (deg), regarding to the Critical slope of failure i_f, Manning's coefficient n and critical angle of depositioni_d, respectively (Figures 4.16-4.18).

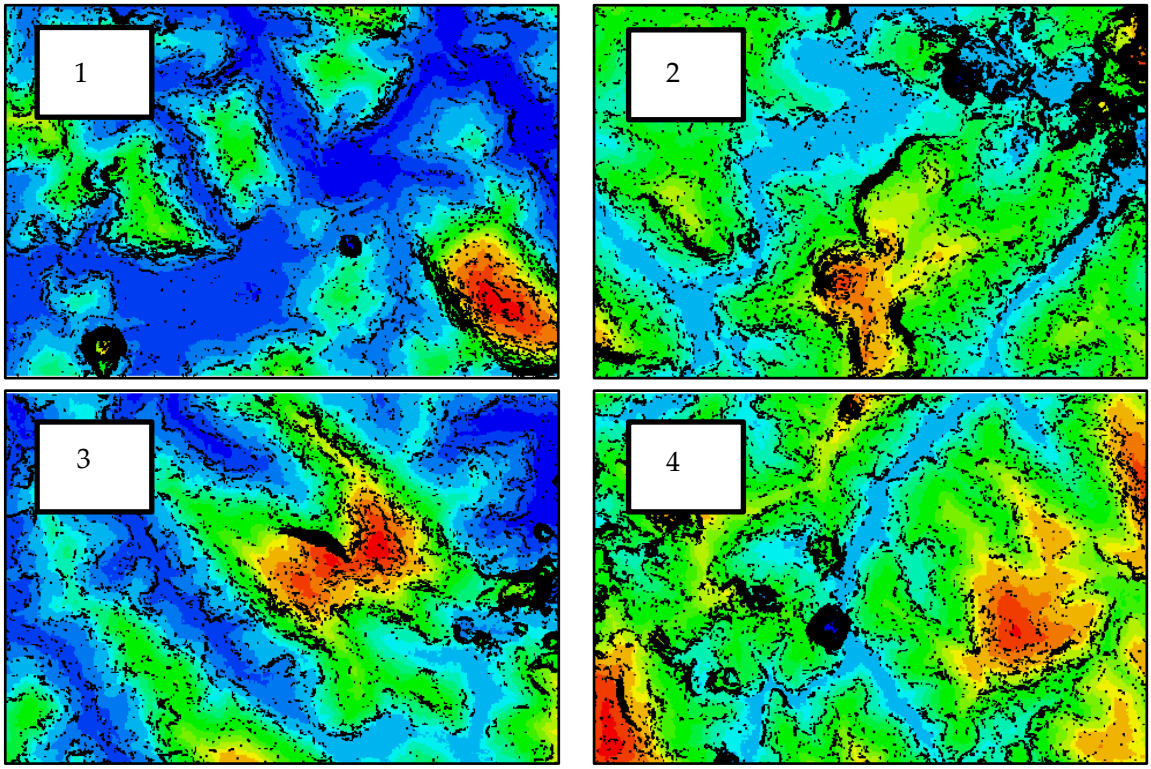

Figure 4.16 Soil particles in initial position distributed in the four case study areas

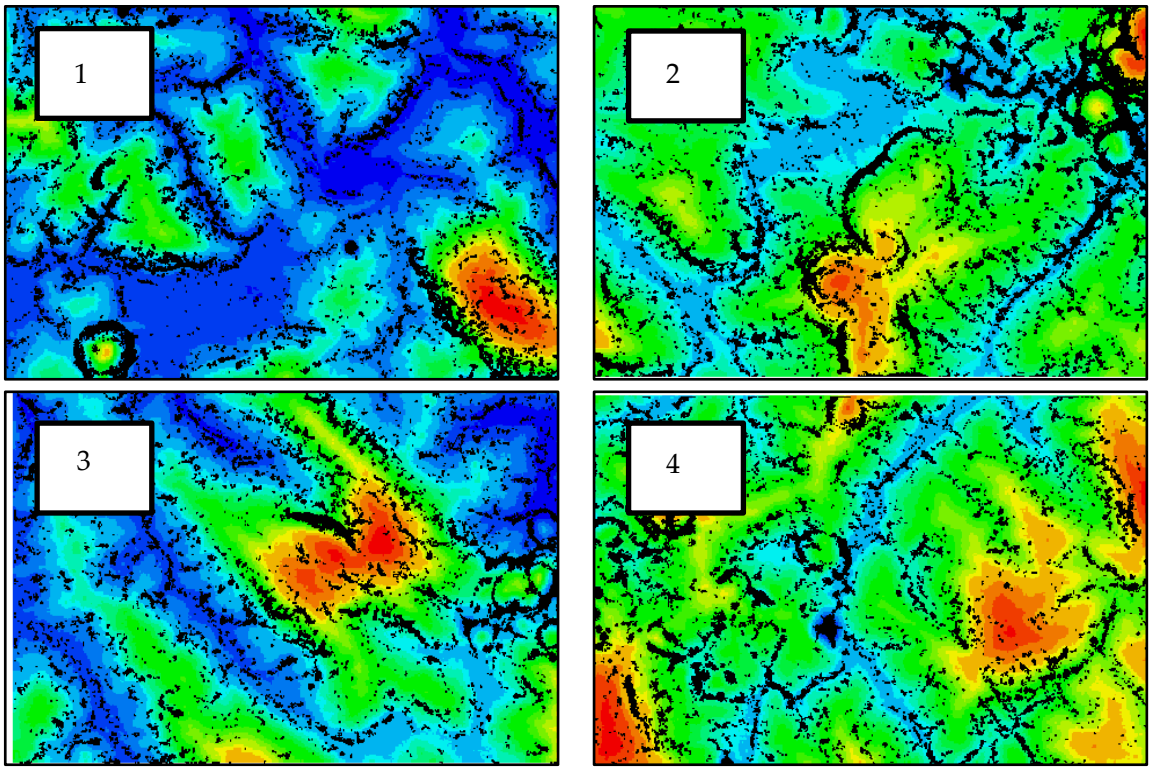

Figure 4.17 Soil particles in motion distributed in the four case study areas

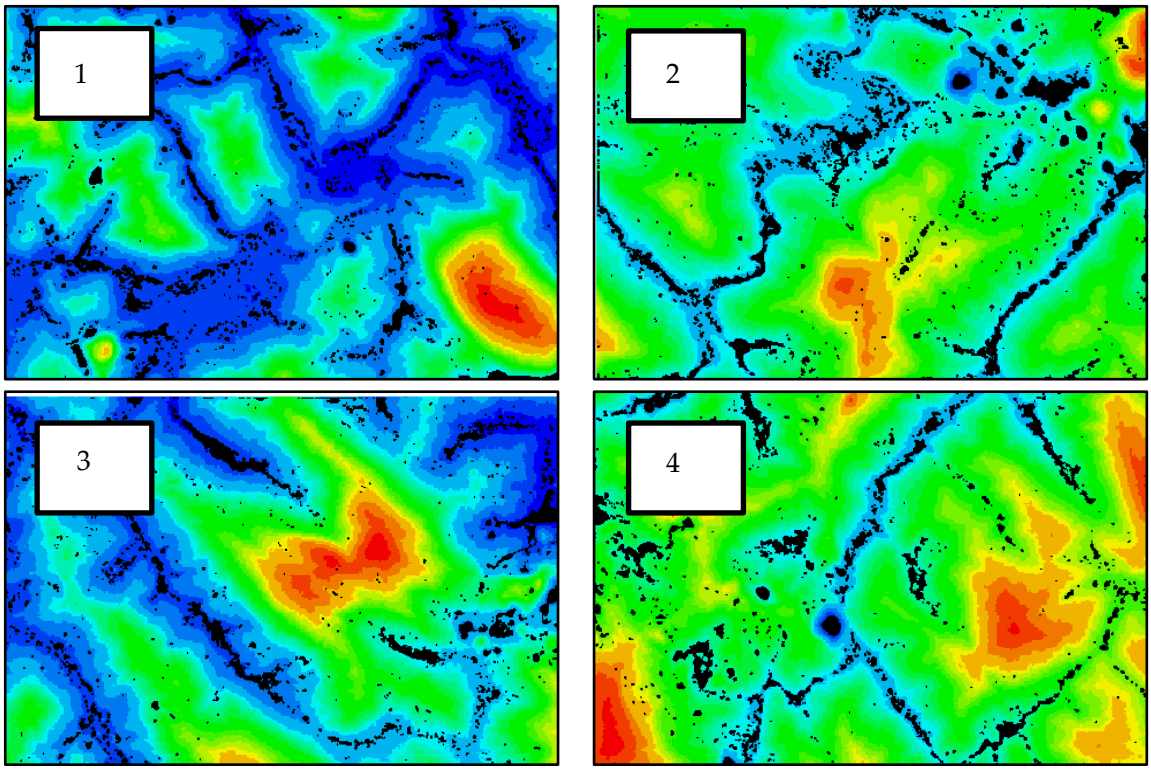

Figure 4.18 Soil particles in final position distributed in the four case study areas

4.4 Discussion of the flow simulation results

We performed the parametric study for the critical slope for failure i_f, Manning's coefficient n and critical angle of deposition i_d in the entire research area. To compare the results, the Figure 4.20 show the sensibility of the accuracy of the simulation a_c for different i_f, n and i_d. The best accuracy when i_f = 30 (deg.), 32 (deg), 35 (deg.), 40 (deg.), 45 (deg.) and 50 (deg.) is 33.43 (%), 35.62 (%), 30.52 (%), 18.77(%), 6.48 (%) and 2 (%), respectively. The accuracy when n=0.1 and i_d==0 (deg) is reported to be bound with the maximum value for the accuracy of the flow simulation. Figure 4.19 shows a relation between the accuracy of the flow simulation a_c with the critical slope angle for faiure i_f.

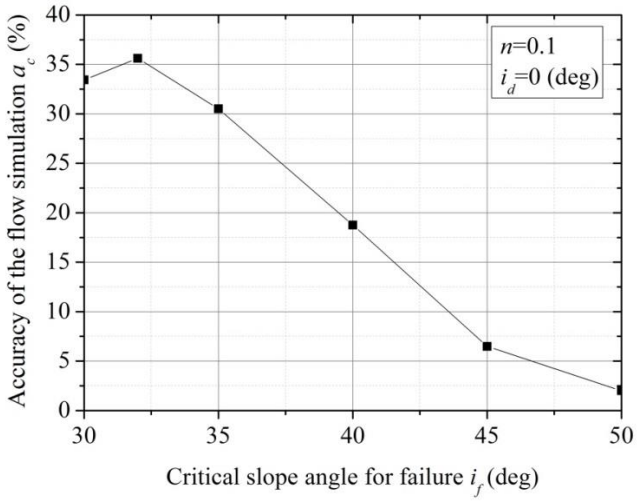

Figure 4.19 Relationship between the accuracy of the flow simulation with respect critical slope angle for failure

Therefore, the accuracy when i_f=32 (deg.), n=0.1 and i_d=0 (deg.) reported the maximum value. The best value of Manning's coefficient corresponds to the values established on literature for water flow on the floodplains for medium to dense brush (item 3.5). Thus, the simulated best result for the Manning coefficient n=0.1 may be suitable.

The critical slope angle for failure i_f=32 (deg.) matches for saturated soil height (h_2 =

0.56 m) for the valley bottom colluvium, which indicates a parcial saturation of the soil that supports the affirmation that the region was severely hit by intense heavy rain during two days before the disaster on January 11-12, 2011.

The third parameter, the critical angle of deposition i_d=0 (deg.), is also in accordance with typical disaster surveys.

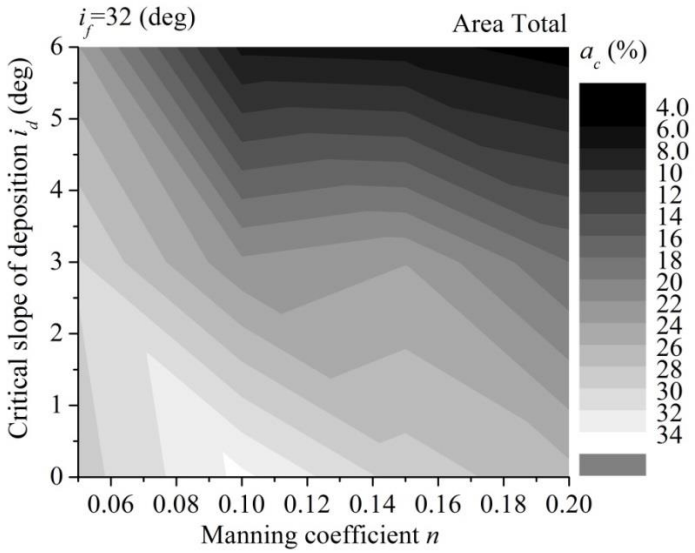

Figure 4.20 Relationship between the accuracy of the simulation facing the sensivity of the parameters n and i_d, when i_f=32 (deg)

Manning coefficient exerts a considerable effect on the accuracy of the flow simulation. This influence is more noticeable in Figure 4.21 where the relation between the accuracy of the flow simulation and Manning coefficient is plotted for the constant $i_d = 0$. Values for $n < 0.1$ represent an over-estimate area, while $n > 0.1$ indicates an under-estimate area.

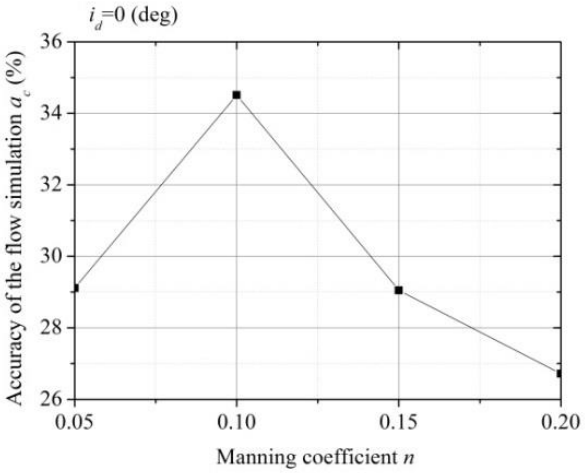

Figure 4.21 Relation between accuracy of the flow simulation and Manning coefficient for the critical angle of deposition equal to 0 (deg.)

4.5 Accuracy of the flow simulation

In the previous item (5.4) we venture to find the optimal parameters for the entire region: 0.1 and 0 (deg.) for Manning coefficient and critical slope of depositioni_d, respectively. Finally, we tested the accuracy of the flow simulation with the optimal parameters. Eq. 4.1 was used to calculate the agreement between the simulated damage area A_s and the actual damage area A_a (item 4.2). Prior to analyze the accuracy, a quantitative approach was employed to find the average of accuracy of the flow simulation among the four areas.

$$a_c(average) = \sum_{n=1}^{4} \frac{a_n}{4} \tag{5.1}$$

Table 5.2 provides the results obtained from the analysis when the critical slope angle for failure are $30(\text{deg.}) \leq i_f \leq 50(\text{deg.})$. The average accuracy when $i_f = 35$ (deg) is about 30.52%. This value falls drastically when $i_f = 50$ (deg). It can be seen in details from the Table 4.2 that the results reported when the critical slope angle for failure $i_f = 32$ (deg) revels that the best average accuracy of the flow simulation is about 35.62%. Results for the critical slope angle for

failure i_f >32 (deg.) present a decay in the accuracy until it reaches 2.01% when i_f = 50 (deg.). For i_f <32 (deg.), the accuracy also declines starting around 30 (deg.), when the accuracy is 33.43%. In an analysis of the events of landslides related to the rainfall in Rio de Janeiro, Overall, these results indicate a good agreement with our landslide simulation.

Table 4.2 Results of the accuracy of the flow simulation to respect critical slope angle for failure in the 25 small areas

	$\mathbf{A}_s$	$\mathbf{A}_s$	$A_a \cup A_s$	$A_a \cap A_s$	$a_c(\%)$	$a_c(\%)$ (average)
UPPER LEFT (1), if 30	2,468,571.43	5,513,142.86	5,533,714.29	2,448,000.00	44.23792	33.43
UPPER RIGHT (2), if 30	1,933,714.29	6,171,428.57	6,212,571.43	1,892,571.43	30.46358	
BOTTOM LEFT (3), if 30	1,707,428.57	5,101,714.29	5,369,142.86	1,440,000.00	26.81992	
BOTTOM RIGHT (4), if 30	1,810,285.71	5,451,428.57	5,492,571.43	1,769,142.86	32.20974	
UPPER LEFT (1), if 32	2,468,571.43	2,756,571.43	3,764,571.43	1,460,571.43	38.79781	35.62
UPPER RIGHT (2), if 32	1,933,714.29	3,744,000.00	4,217,142.86	1,460,571.43	34.63415	
BOTTOM LEFT (3), if 32	1,707,428.57	3,456,000.00	3,929,142.86	1,234,285.71	31.41361	
BOTTOM RIGHT (4), if 32	1,810,285.71	3,003,428.57	3,497,142.86	1,316,571.43	37.64706	
UPPER LEFT (1), if 35	2,468,571.43	2,838,857.14	3,846,857.14	1,460,571.43	37.96791	30.52
UPPER RIGHT (2), if 35	1,933,714.29	3,908,571.43	4,402,285.71	1,440,000.00	32.71028	
BOTTOM LEFT (3), if 35	1,707,428.57	3,291,428.57	3,949,714.29	1,049,142.86	26.5625	
BOTTOM RIGHT (4), if 35	1,810,285.71	2,736,000.00	3,641,142.86	905,142.86	24.85876	
UPPER LEFT (1), if 40	2,468,571.43	1,563,428.57	3,229,714.29	802,285.71	24.84076	18.76
UPPER RIGHT (2), if 40	1,933,714.29	1,728,000.00	2,941,714.29	720,000.00	24.47552	
BOTTOM LEFT (3), if 40	1,707,428.57	946,285.71	2,406,857.14	246,857.14	10.25641	
BOTTOM RIGHT (4), if 40	1,810,285.71	1,254,857.14	2,653,714.29	411,428.57	15.50388	
UPPER LEFT (1), if 45	2,468,571.43	226,285.71	2,633,142.86	61,714.29	2.34375	6.48
UPPER RIGHT (2), if 45	1,933,714.29	987,428.57	2,592,000.00	329,142.86	12.69841	
BOTTOM LEFT (3), if 45	1,707,428.57	288,000.00	1,933,714.29	61,714.29	3.191489	
BOTTOM RIGHT (4), if 45	1,810,285.71	493,714.29	2,139,428.57	164,571.43	7.692308	
UPPER LEFT (1), if 50	2,468,571.43	144,000.00	2,592,000.00	20,571.43	0.793651	2.01
UPPER RIGHT (2), if 50	1,933,714.29	432,000.00	2,262,857.14	102,857.14	4.545455	
BOTTOM LEFT (3), if 50	1,707,428.57	92,571.43	1,789,714.29	10,285.71	0.574713	
BOTTOM RIGHT (4), if 50	1,810,285.71	185,142.86	1,954,285.71	41,142.86	2.105263	

This case study seeks to examine the simulation result for each small analyzing area. Just for illustration purposes, Figures 4.22 and 4.23 explore the variation of the flow simulation in cases when i_f = 30 (deg) and i_f = 40 (deg), with n=0.1, i_d=0 deg. for the entire area.

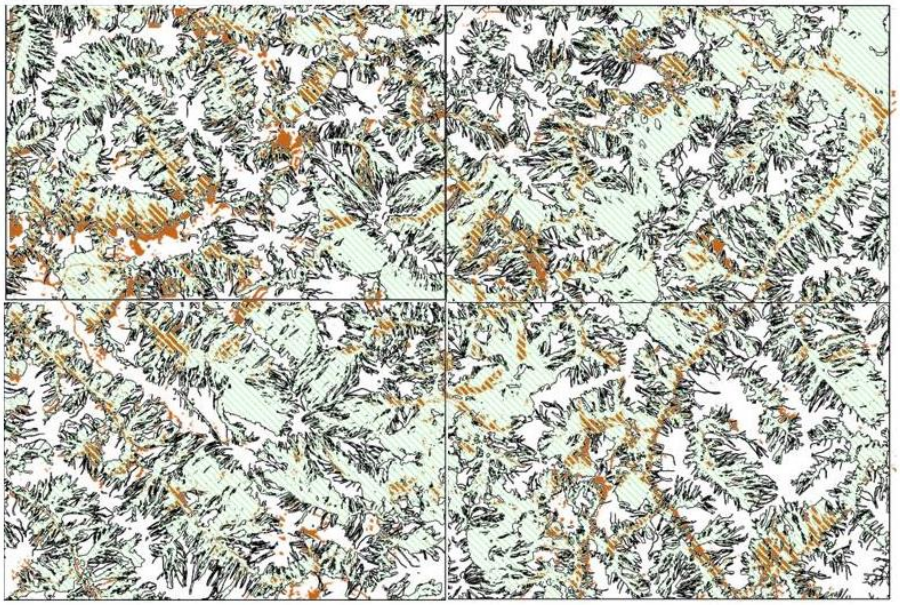

Figure 4.22 Result of the flow simulation in the entire area when if=30 (deg), id=0 and n=0.1

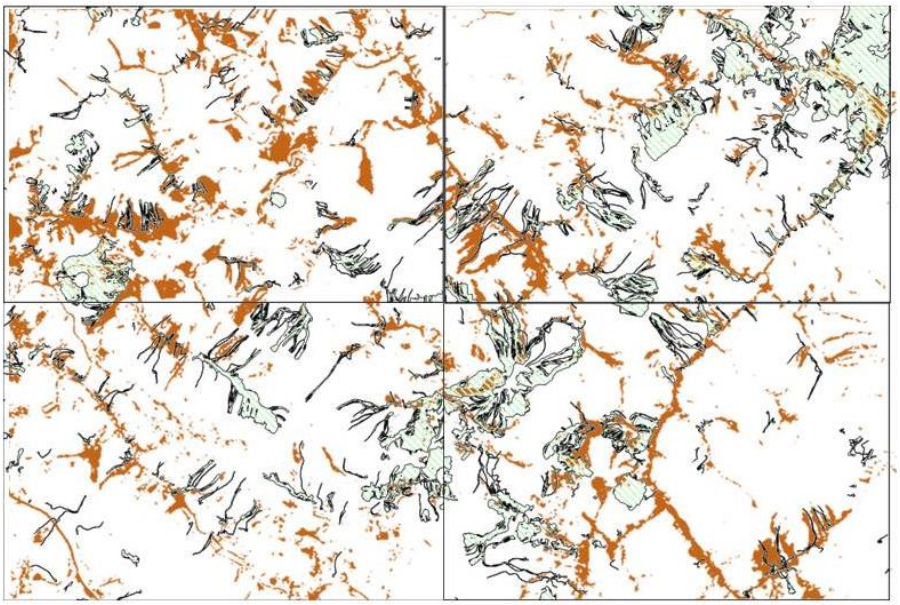

Figure 4.23 Result of the flow simulation in the entire area when if=40 (deg), id=0 and n=0.1

The actual damaged area A_a is represented by the orange color in Figures 4.22-4.23. Hatched green is showing the area hit by the landslide simulation, or as we call in this research

"Simulated affected area A_s". The case when i_f =30 (deg) shows a large over-estimated area, while i_f =40 (deg) presents an under-estimated area.

The average of the accuracy of the damaged area prediction is 35.62 (%) at maximum when i_f =32 (deg), n==0.1, i_d=0 deg. As can be seen from the Figure 4.24, the previously set of parameters reported significantly a good balance between the intersections areas ($A_a \cap A_s$) and the simulated area A_s. The simulated affected area A_s, in black here, shows a good coverage of the areas marked in orange (Actual damage area A_a).

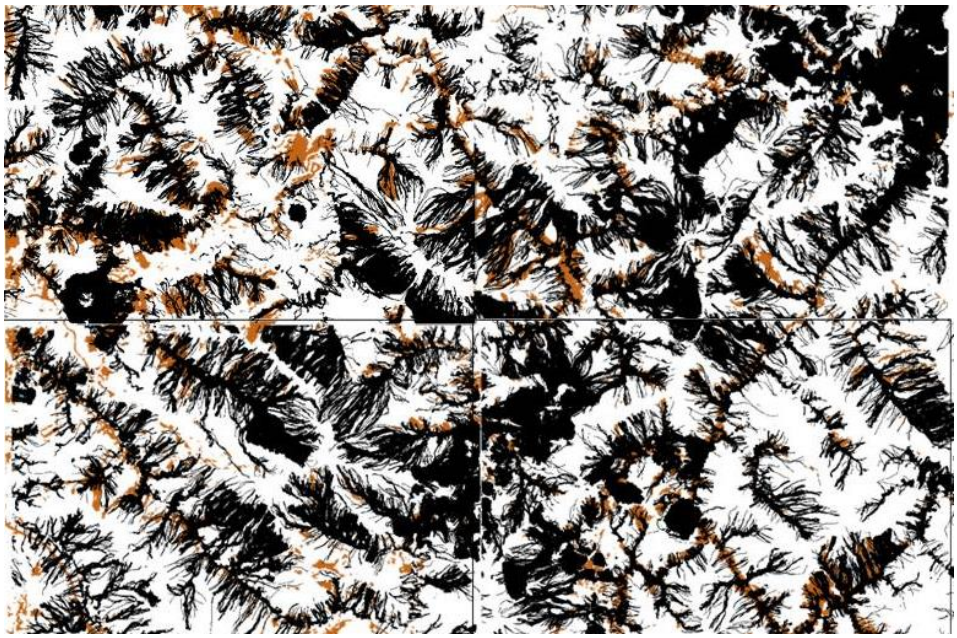

Figure 4.24 Result of the flow simulation in the entire area when if=32 (deg), id=0 and n=0.1

The first set of questions aimed to the accuracy found in Areas No. 1 and No. 3. After examining these areas, we found that these areas include the old landslide scars as shown in Figure 4.25 and 4.26 and that the simulation reproduced them (Figure 4.26 and 4.27). If we exclude those old scars, the accuracy improved from 38.79(%) and 31.41(%) to 39.88(%) and 37.26(%) in Areas No. 1 and No.3, respectively. Therefore, in case that we can discard the simulate damaged area in the areas where it is possible to recognize old landslide scar, the average of the accuracy of the damaged area prediction increase to 37.35 (%). This finding

represents an increase of 4.86% in the previous result. Such discovery, further suggests that the simulation result may include some 'future' landslide scars as well. If we carefully compare the simulation result to the damage this time in 2011, we found some dangerous sites in which landslide may occur in the future as shown in Figure 4.29.

Figure 4.25 The scars of old landslide in Area No.1 (left upper)

Figure 4.26 Simulate affected area in Area No. 1

Figure 4.27 The scars of old landslide in Area No.3 (left bottom)

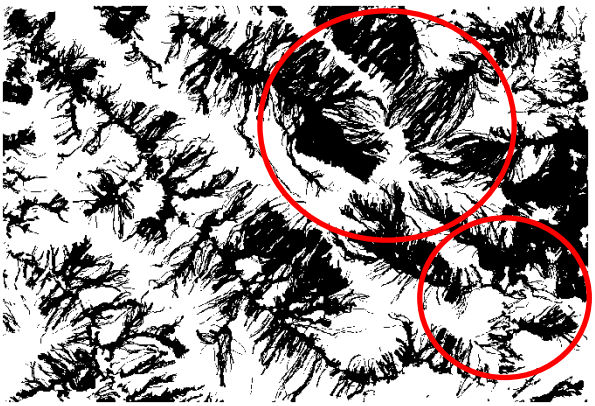

Figure 4.28 Simulate affected area in Area No. 3

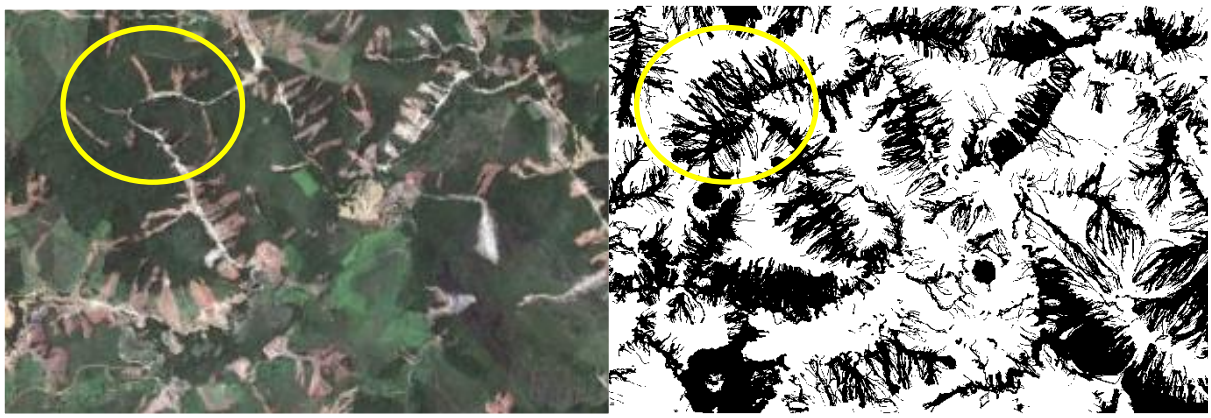

Figure 4.29 Some candidates of future landslide scars shown by yellow circles (Area No.1)

Another issue that should be discussed is the occurrences of interference (i.e. clouds, shadow) in satellite images as explained in item 2.3. It is very difficult to acquire a satellite image totally free of such interferences. Therefore, the acquisition of a satellite image with least interference possible is one of the main issues in order to acquire good result in the flow simulation. Area No. 2 shows two shadows (Figure 4.30) and the consequence in the simulation (Figure 4.31).

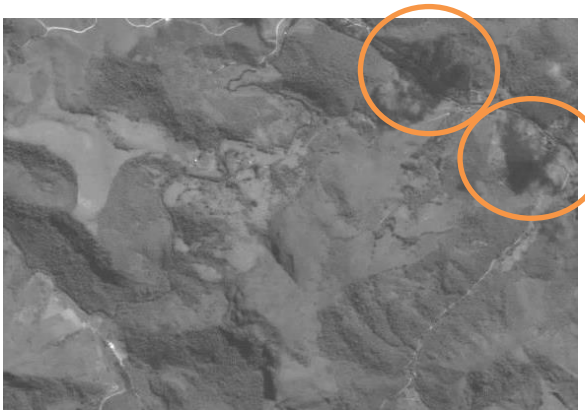

Figure 4.30 Shadows in Area No. 2

Figure 4.31 Effect of the shadows in the simulation result

Area No. 4 has two small clouds; however it interferes in the acquisition of a good landscape representation. The result can be seen in Figure 4.32.

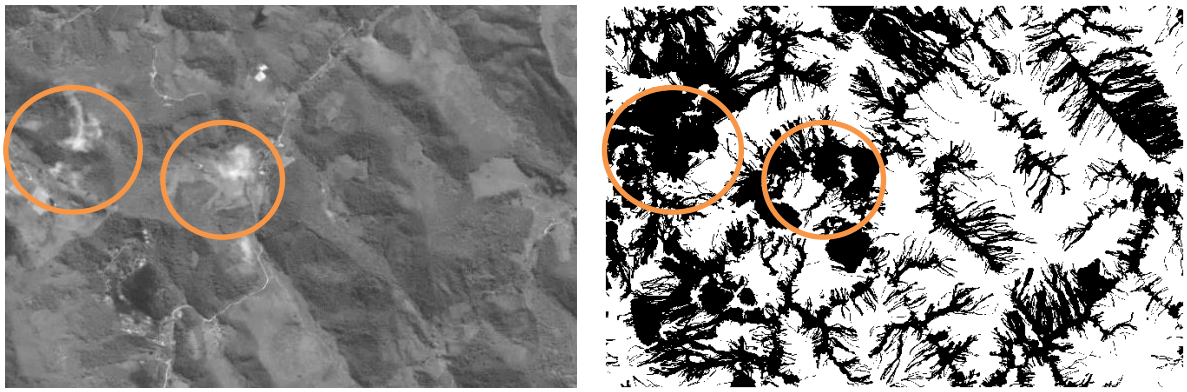

Figure 4.32 Effect of clouds in the simulation result

The key performance, a_c corresponds to the percent of the overlapped area between the simulated area A_s and the actual damage area A_a. Furthermore, we would like to introduce another two keys performances so-called "Simulate Area Ratio" (Eq. 5.2) and "Actual Damaged Area Ratio" (Eq. 5.3), which are defined as the simulated and actual damaged area, respectively, by the total area.

$$R_s = \frac{A_s}{A} \tag{5.2}$$

$$R_a = \frac{A_a}{A} \tag{5.3}$$

The new keys performances helps us to understand the tendency of a_c with respect to i_f (Figure 4.33) According to the results, values for i_f >32 (deg.) correspond to the under-estimated simulated areas, while i_f <32 (deg.) matches the over-estimated simulated areas.

For Nova Friburgo's case study, it would be inappropriate to take more conclusions regarding to the simulate area ratio facing the interferences in the satellite image that we exhaustively mentioned (i.e. clouds, shadows, old landslide scar).

It should be highlighted that a good representation of the landscape has a total influence on the result of the flow simulation. This conclusion is in agreement with Fannin et al. (2001) and Rickenmann et al. (2006).

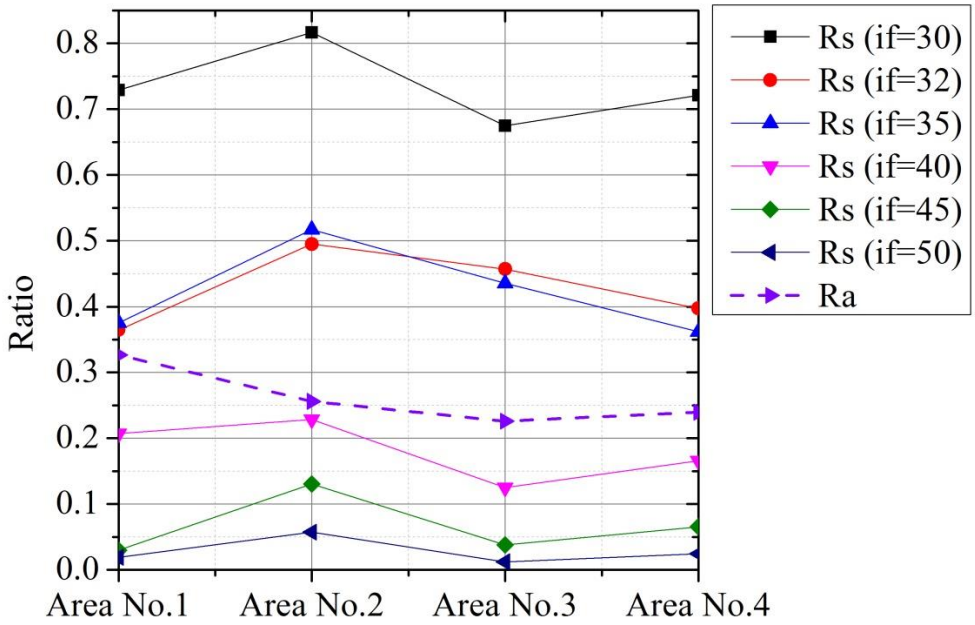

Figure 4.33 Damage area ratio for the simulation and for the actual damage.

5. FLOW SIMULATION FOR EVALUATING DAMAGE AREA IN HOFU

5.1 Landslides in Hofu, Yamaguchi (Japan)

Japan's land is formed by 75% of mountainous area. This natural condition associated with triggers factor such as torrential rain, earthquake, snow provide susceptible condition to landslides. Data from several resources have identified the occurrences of landslides disasters since ancient times. Between 3000 to 1000 BC, there is evidence of landslide failure in Aso-cho, Ibaragi Prefecture. Other example in Kumamoto and Nagasaki (1972), where we faced several landslides caused by heavy rain. More recently, on July 21, 2009, Hofu city was devastated by over 1,000 landslides triggered by torrential rain. Due to its impressive quantity of landslides, Hofu city was chosen as a case study.

Hofu city is located in the south of Yamaguchi Prefecture, western Japan (Japan National Tourism Organization). The torrential rain was characterized by daily precipitation reaching 275 mm (Misumi, 2010) with higher rainfall intensity (around 6.35 centimeters per hour) that was able to induce shallow landslides (Chen et al. 2013) and floods. Around 9% of its area was destroyed due to several landslides triggered by heavy rain in 2009. Many people die and hundreds others had their houses flooded by a mass of soil.

Additional and more accurate information provided by Japan Society of Civil Engineers (Figure 6.1) informed that there are 160 piezometers spread around Yamaguchi Prefecture. During July 20th and 21th , the piezometer in Hofu city reached 331.5 mm. The maximum amount of rainfall per hour was 63.5 mm in Hofu. Near Hofu city (Shimomigita) during 10 minutes of rainfall the amount of rain reached 18 mm at 8:00. Later, around 11:40, the precipitation was 12-13 mm. From July 21th at 6:00 after 15 hours, the total amount of rainfall was 228.5 mm in Hofu city. During 10 minutes, the rain precipitation reached the peak of 10 mm between 7 and 9 times. Therefore, it is possible to affirm that the rain happened in concentrated form and in a short period of time.

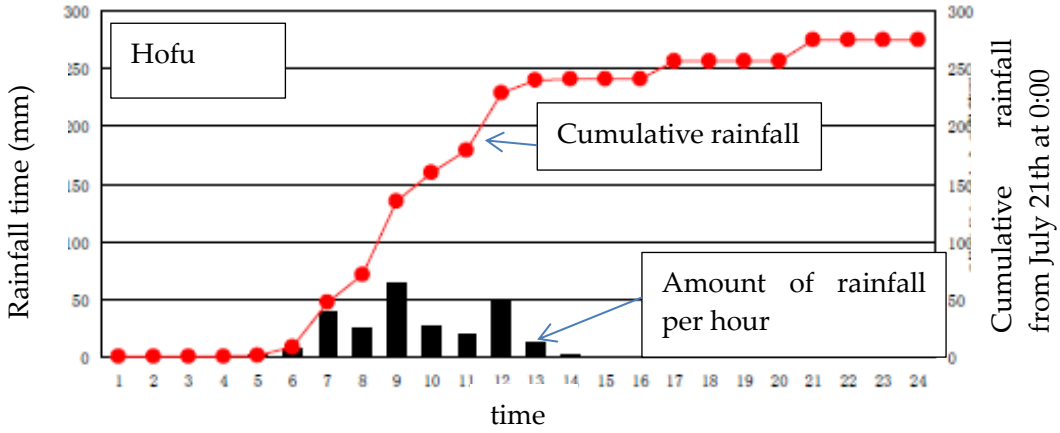

Figure 5.1 Accumulated rainfall in Hofu

According to Yamashita et al. (2011) the area is basically formed by two types of granite rocks: granodiorite (Gd) and Granite (Gr). Yamashita et al. analyzed that places with granodiorite (Gd) showed lower number of landslides with larger size, while places formed by Granite (Gr) had higher number of landslides with smaller size.

Shortly after the disaster on July 21, 2009, Pasco Corporation had staked out the areas hit by landslides marked with solid line. A while after, Asia Air Survey Corporation added the missing areas (shown in dashed line). The most complete mapping of the affected area can be seen in Figure 5.3.

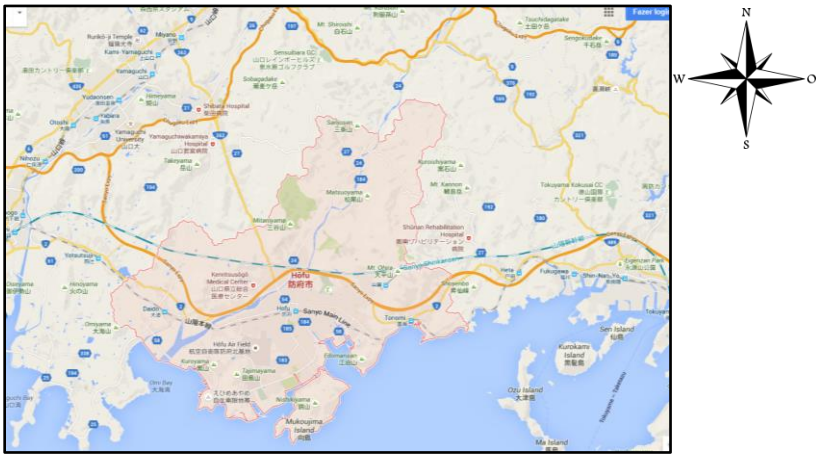

Figure 5.2 Map with Hofu location

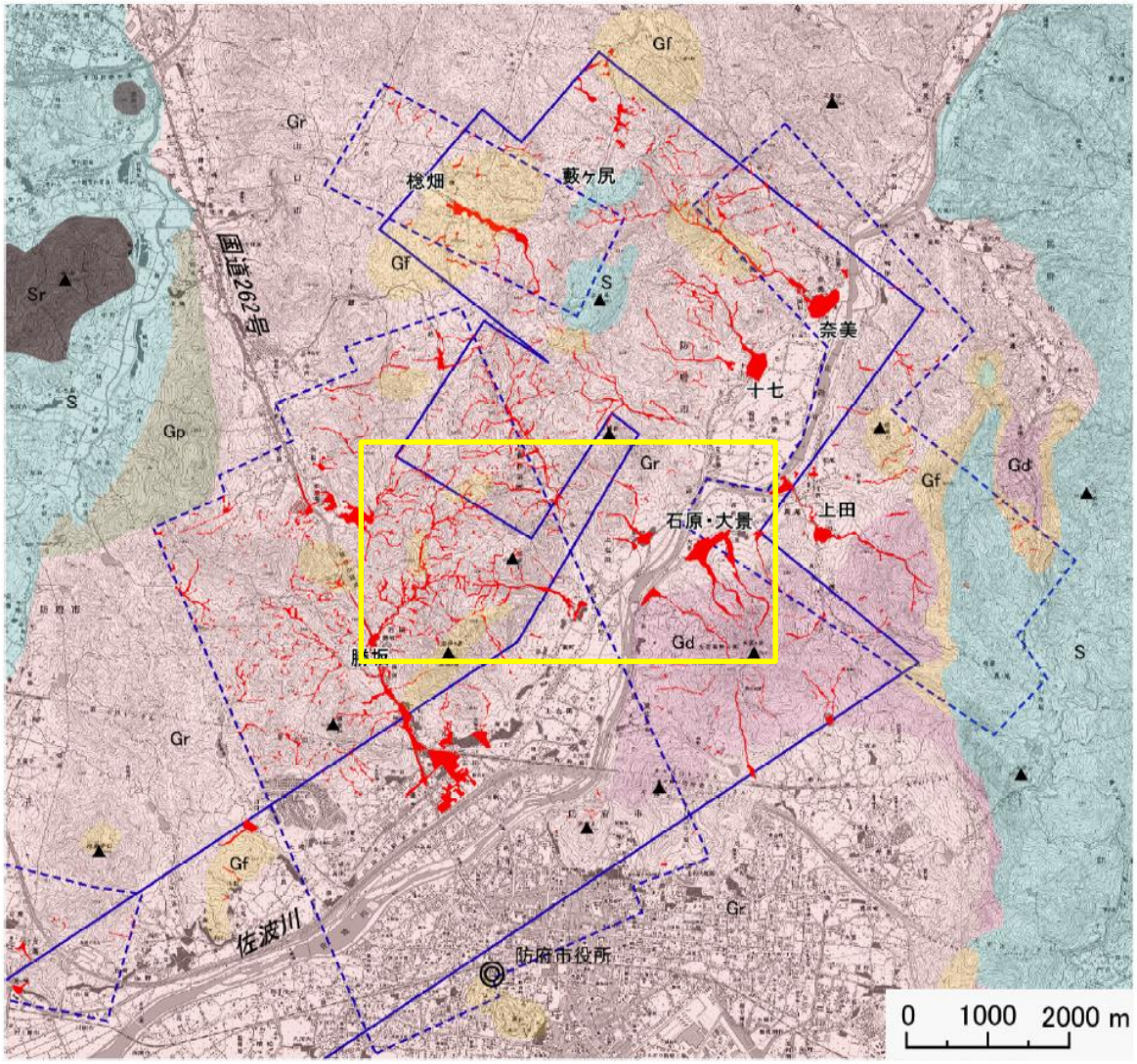

Figure 5.3 Landslide map constructed by Asia Air Survey Co. in dashed line and Kokusai Kogyo Co. Ltd and Pasco Co., Ltd. in solid line (Wakatsuki et al. 2010). The area highlighted in yellow is our case study area

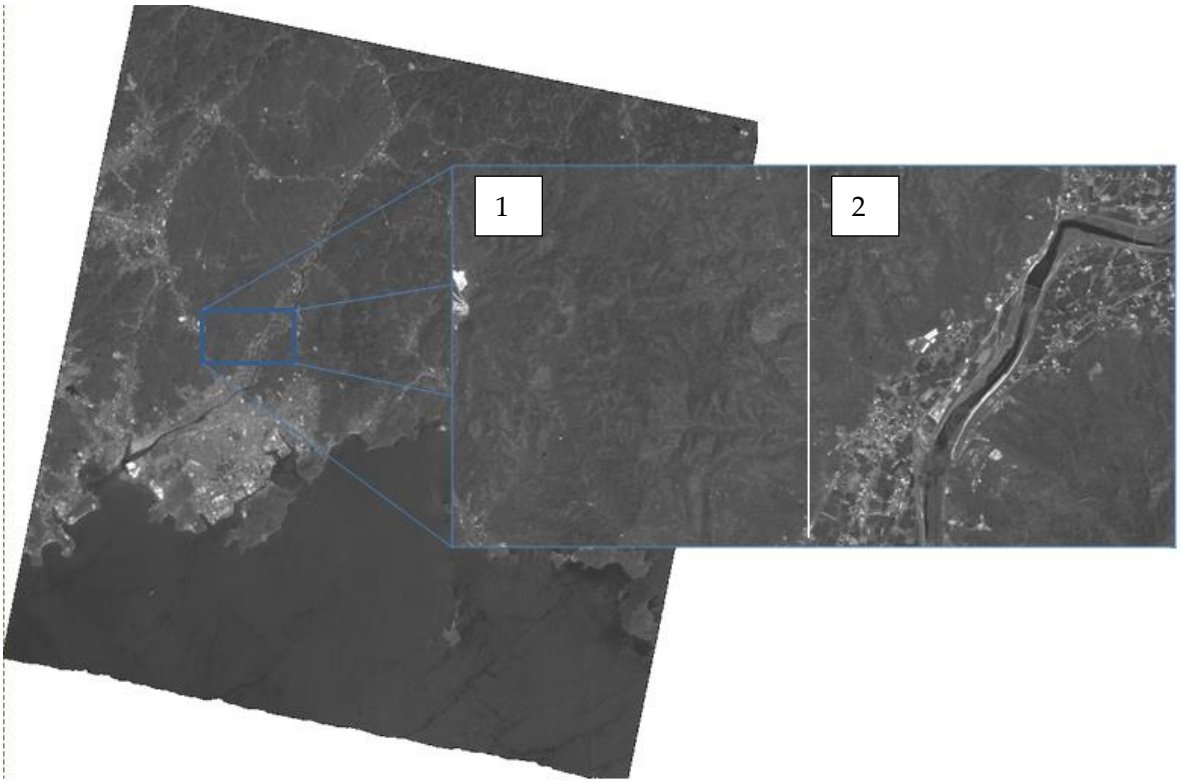

Figure 5.4 ALOS satellite image before disaster in Hofu. Detailed is the researched area (4750m by 2500m)

The area schedule to our study measures 4750 m by 2500 m in Hofu city. This area covers the most important two different type of soil of the region: granite in Area No.1 and granodiorite in Area No.2 (Figure 5.4). This region lies on moderate mountains under quota elevation of 500 m (Figures 5.5 and 5.6).

- Area No.1: Figure 5.7 presents the summary curve of cumulative frequency of slopes that shows the steepest region with around 90% of the area composed by slopes up to 25 (deg.). This area also presents higher number of landslides with smaller size.
- Area No.2: covers a region with around 90% composed by slopes up to 20 (deg.) (Figure 5.7). This area showed lower number of landslides with larger size.

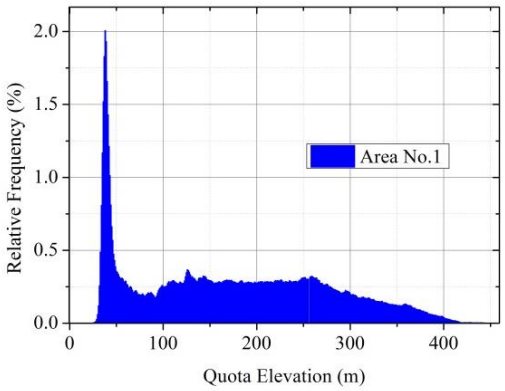

Figure 5.5 Curve of cumulative frequency of quota elevation of the Area No.1

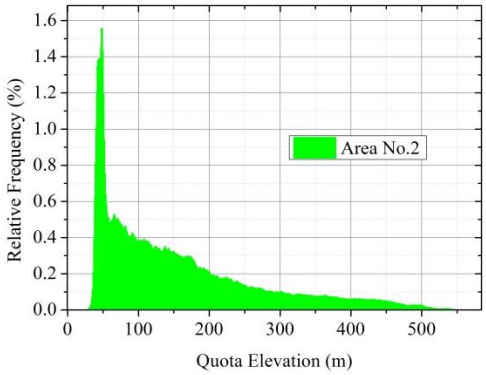

Figure 5.6 Curve of cumulative frequency of quota elevation of the Area No.2

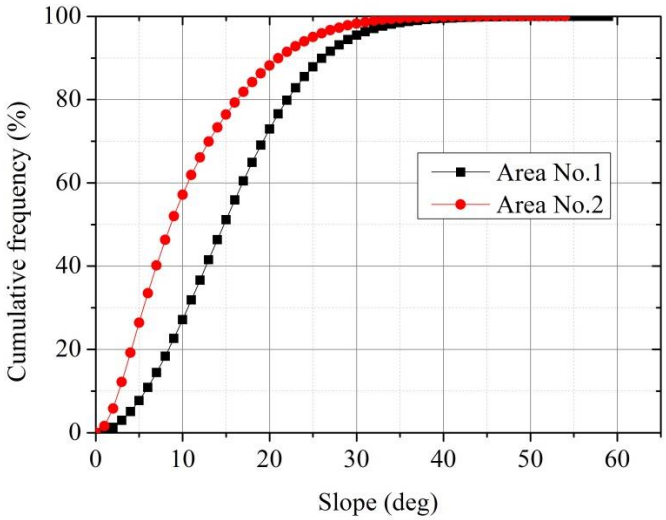

Figure 5.7 Curve of cumulative frequency of slopes of the two areas

5.2 Mechanical properties of the surface soil

Due to the magnitude of the catastrophe in 2009, the area in Hofu city has been well studied by several researches. Yamashita et al. (2013) conducted a new field research to determine the soil parameters for the area in Hofu city (Figure 5.8). On completion of acquisition of the samples, the process of parameters values estimation was carried out and the result can be seen from the data in Table 5.1.

Figure 5.8 Researched area after the disaster in Hofu city, Yamaguchi Prefecture

Differently from the image binarization processed in Rio de Janeiro's case study to extract the landslides scars, here we use the survey produced by Asia Air Survey Co., Kokusai Kogyo Co. Ltd and Pasco Co. Figure 5.9 shows the landslides scars in the region chosen for case study.

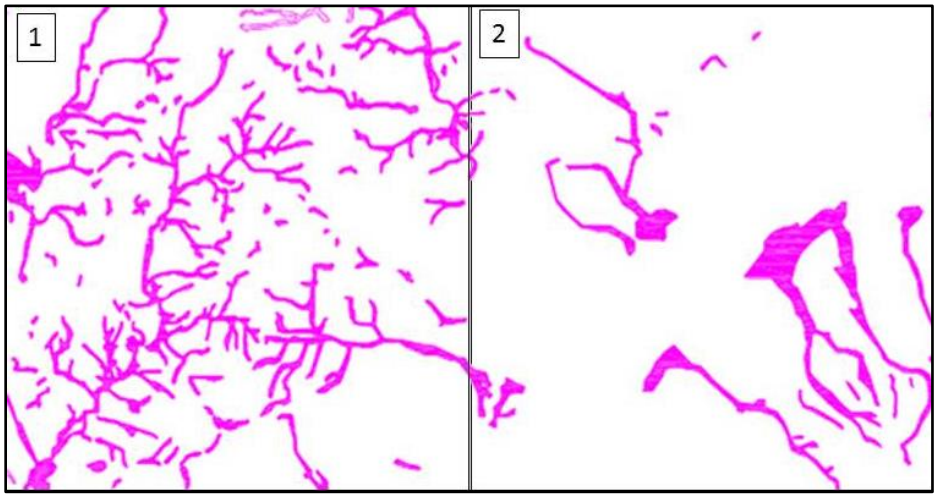

Figure 5.9from Landslides scars extracted the survey produced by Asia Air Survey Co., Kokusai Kogyo Co. Ltd and Pasco Co

It has been suggested by Chen et al. (2013) a typical soil thickness of the slope as about 2.0 m. Therefore, we also assumed the surface soil depth as 2 meters.

In order to reduce the complexity in reproduce exactly the soil parameters that differ in

different places, we examined the four types of weathered granite presented by Yamashita et al. (2013) and we drew a relationship between the critical slope for failure i_f and saturated soil height h_2 determined when the $F_s = 1$ in Eq. 1.5.

Table 5.1 Mechanical properties of the surface soil in the research area in Hofu (Yamashita et al. 2013)

Soil type	Specific gravity	Void ratio	Friction angle (deg.)	Cohesion (kPa)
Gr	1.603	0.7-0.8	25.8	12.65
Gd	1.603	0.7-0.8	46.9	0.6

Different from Chapter 5, we decided to perform the landslide simulations using two optimal sets of soil parameters for the Hofu's case study. For the Area No.1, and Area No. 2 the Gr and Gd will be employed, respectively.

Figure 5.10 shows that the Granite (Gr) is more fragile than the Granodiorite (Gd). This finding can be verified through the number of small landslides in Area No. 1, while in Area No. 2 it is possible to find a smaller number of landslides, with larger size.

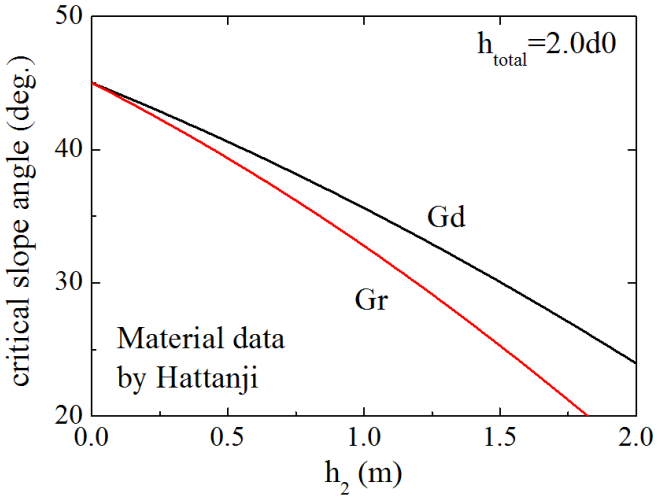

Figure 5.10 Relationship between the critical slope angle for failure and its saturated soil height

We decided to evaluate the total area with i_f (20, 23, 24, 25, 30, 35 and 40 deg).

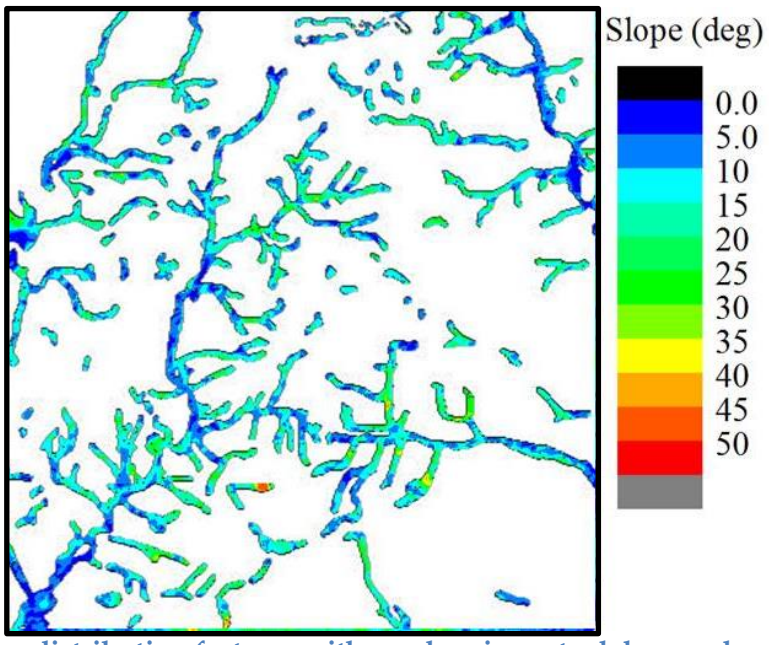

Figure 5.11 Slope distribution features with overlapping actual damaged area for Area No. 1

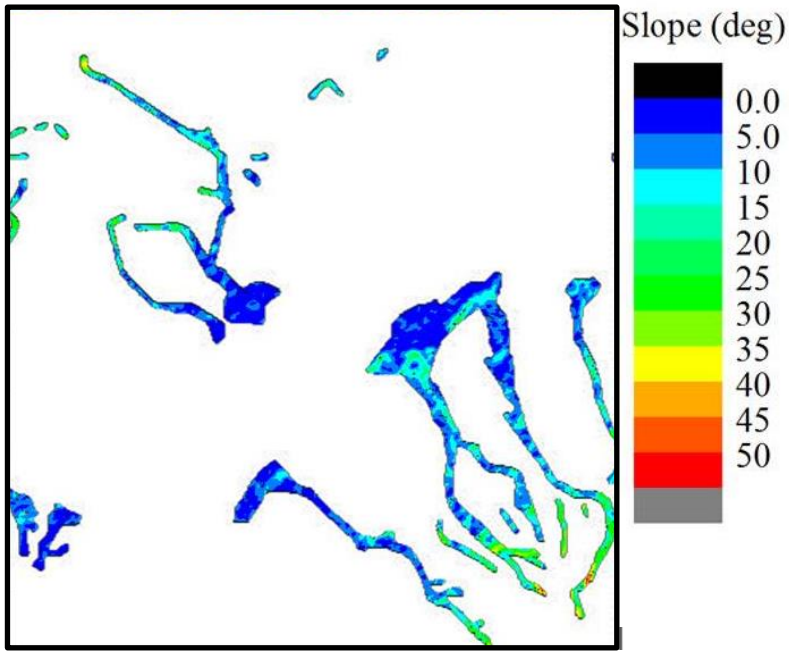

Figure 5.12 ith overlapping actual damaged area for Area No. 2

A complementary evaluation to find the critical slope angle for failure i_f that best represents the real case, consists in overlapping areas of slope distribution and actual damaged areas A_a (Figures 5.11 and 5.12) to search for a relationship between both. It is not expected an

easy and clear evaluation as we ignore a series of complex items to make this landslide model simulation more convenient. However, we can note from the images that the initiation area is composed by slopes between 20 (deg) and 35 (deg).

5.3 Flow simulation for evaluating damage area

In here, we consider the process described previously and we added particles described on item 3.3 and perform flow simulations according to Eq. 3.1. We decide to carry the simulations in a 5.0 m grid size.

The researched area in Hofu measures 4,75 km by 2,5 km, we discretized in two domains for flow simulations (Figure 5.4).

Figure 5.13 presents the initial position (in black) for the particles in the area chosen as a case study in Hofu city. As well as the Figure 5.14 shows the particles in motion and Figure 5.15 indicates the final position of the particles.

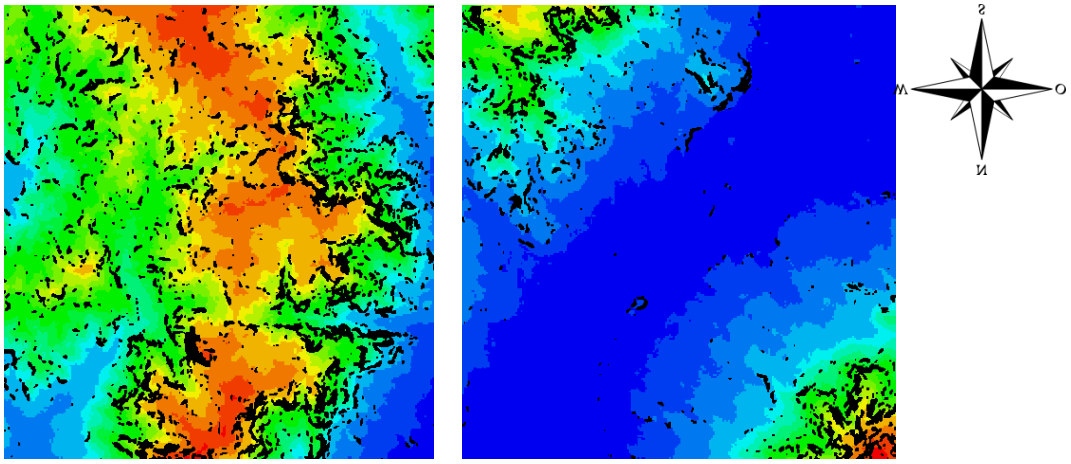

Figure 5.13 Particles in initial position

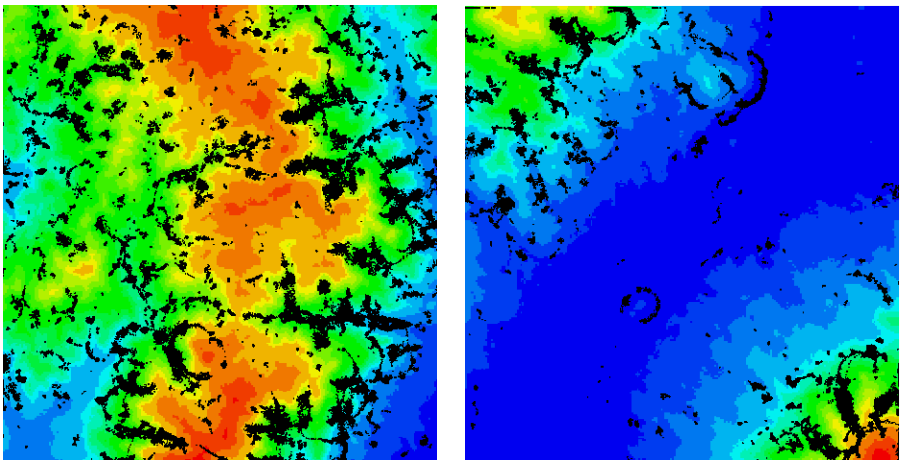

Figure 5.14 Particles in motion

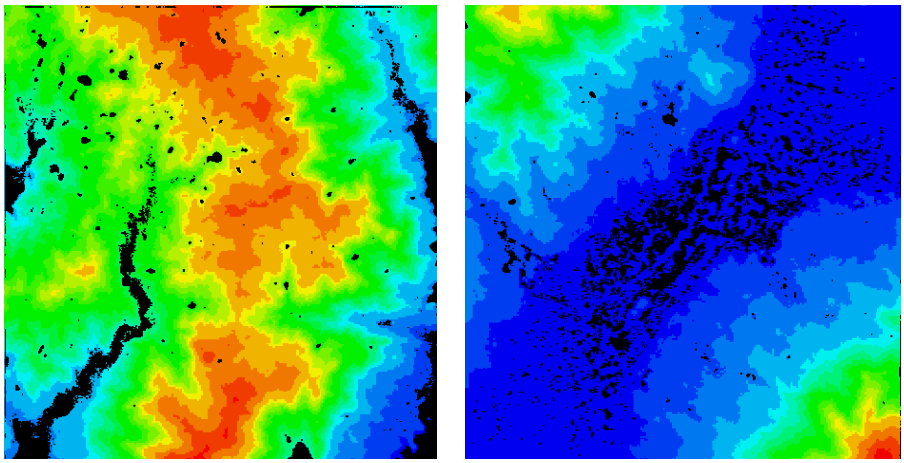

Figure 5.15 Particles in final position

5.4 Discussion of the flow simulation result

The rapidly flowing soil-water mixture required for the evaluation of landslide run out areas is quite difficult to obtain before failure. Therefore, our statistical analysis represents a valuable evaluation of the sensibility of the parameters. We performed the parametric study for the critical slope angle for failure i_f , Manning's coefficient n and critical angle of deposition i_d in the entire research area. The first set of analyzes examined the two area with the same set of parameters. To compare the results, the Figures 5-16-5-18 show the sensibility of the accuracy of the simulation a_c for different i_f, n and i_d. The best accuracy when i_f = 20 (deg.), 23 (deg.), 24

(deg.), 25 (deg.), 30 (deg.), 35 (deg.) and 40 (deg.) is 31.59 (%), 31.5 (%), 31.72 (%), 31.71 (%), 29..7 (%), 11.71 (%) and 3.68 (%), respectively. Therefore, the accuracy when i_f=24 (deg.), n=0.04 and i_d=0 (deg.) reported the maximum value. The best value of Manning's coefficient corresponds to the value utilized by Maeda et al. (2011). Also, the critical angle of deposition i_d=0 (deg.), is also in accordance with typical disaster surveys.

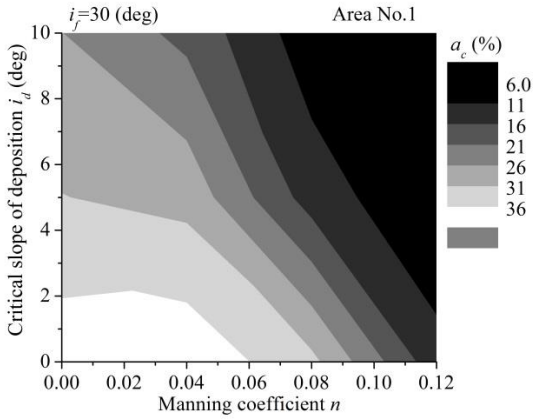

Figure 5.16 Accuracy of the simulation in if=30 (deg.)

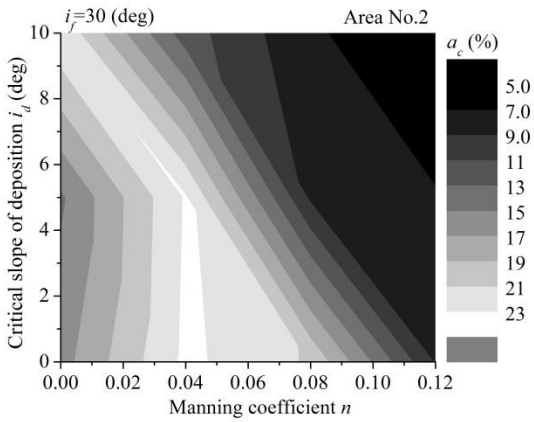

Figure 5.17 Accuracy of the flow simulation in if=30 (deg.)

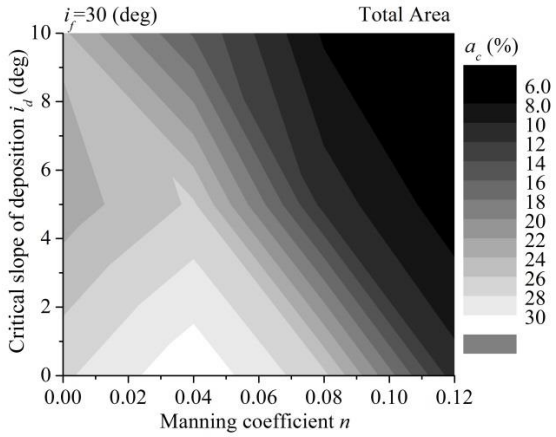

Figure 5.18 Accuracy of the flow simulation in if=28 (deg.)

This case study seeks to examine the simulation result for each analyzing area. Just for

illustration purposes, Figure 5.19-5.20 explore the variation of the flow simulation in cases when i_f = 20 (deg), 25 (deg), 30 (deg), 35 (deg) and 40 (deg), with n=0.04, i_d=0 deg. for the entire area.

Turn out that in Area No.1, it is possible to elect a Manning coefficient between 0.0 and 0.06, and the critical slope of deposition i_d, between 0 (deg) and 2 (deg), even so, it maintains the maximum average for the accuracy for the flow simulation in this area. Area No. 2, in which the landscape representation is composed by the steepest region, the accuracy of the simulation has a variation in the accuracy of the flow simulation more unlike.

It is interesting to note that in the total area of this analysis (Figure 5.18), the accuracy of the simulation did not suffer much variation when i_d is between 4 (deg) and 6 (deg.) for n=0.0 However, although the accuracy of the flow simulations have been reasonable for values in n=0.0, the simulations do not demonstrated a realistic performance.. The relation between the accuracy of the simulation and the manning coefficient is explored for the i_f=24 (deg.) for the entire area in Figure 5.19, as well as the relationship between the critical slope of deposition i_d and the accuracy of the flow simulations a_c.

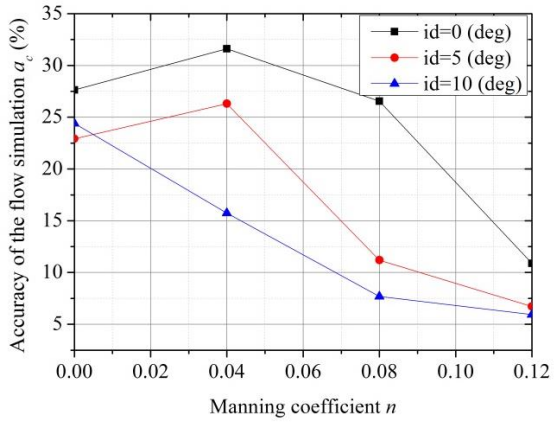

Figure 5.19 Relation between accuracy of the flow simulation and Manning coefficient for id=0 (deg), 5 (deg) and 10 (deg)

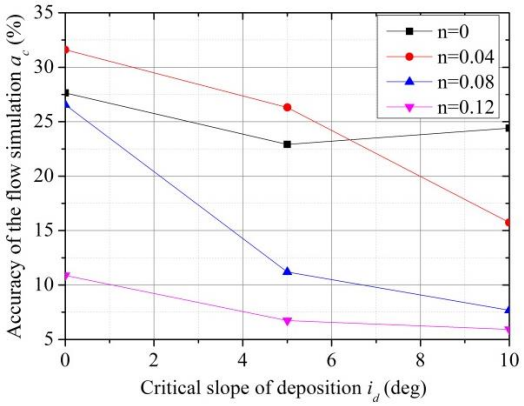

Figure 5.20 Relation between accuracy of the flow simulation and critical slope of deposition for n=0, 0.04, 0.08 and 0.12

Only for illustration purposes, Figures 5.21 show a variation in the simulation areas

results for i_f=25, 30, 35 and 40 (deg) for Area No. 1. As well as Figures 5.22 illustrate the simulation behavior for i_f=25, 30, 35 and 40 (deg) for Area No. 2.

Area No. 1

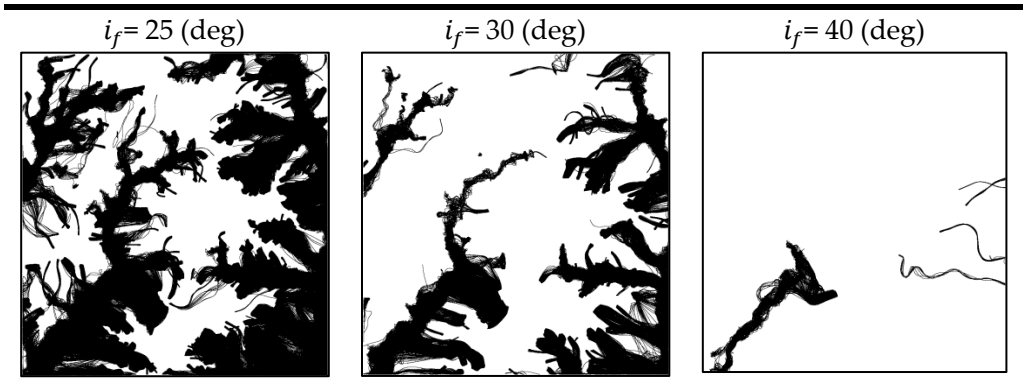

Figure 5.21 Flow behavior under different critical slope for failures in Area No. 1

Area No. 2

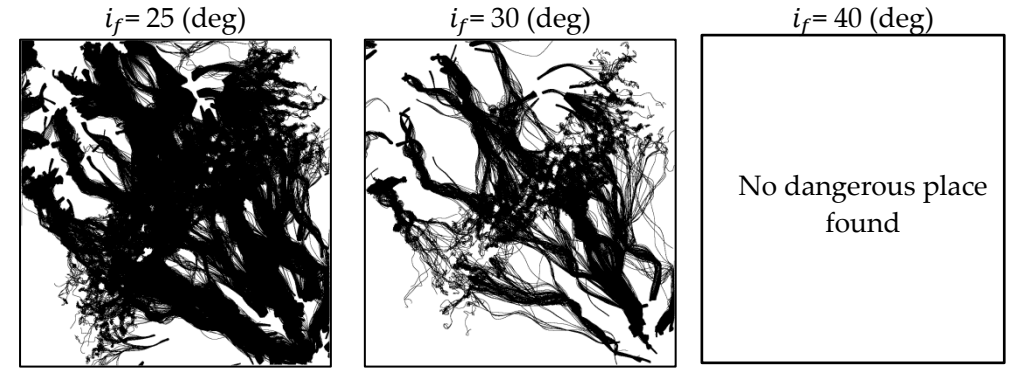

Figure 5.22 Flow behavior under different critical slope of failure in Area No. 2

5.5 Accuracy of the flow simulation

It has been demonstrated that the best optimal parameters for the entire region is 0.04, 0 (deg.) and 24 (deg.) for Manning coefficient, critical slope of depositioni_d and critical slope for failure i_f, respectively. As early mentioned, here we also use the Eq. 4.1 to calculate the agreement between the simulated damage area A_s and the actual damage area A_a. Prior to analyze the accuracy, a quantitative approach was employed to find the average of accuracy of

the flow simulation among the 2 small areas. Figure 5.23 presents the accuracy of the flow simulation for the total area according to the respective critical slope for failure. It is apparent from this data that the maximum average of the accuracy of the damaged area prediction is 31.72 (%) when the critical slope for failure is 24 (deg.). An over-estimation $i_f < 24$ (deg.) as well as an under-estimation of the damage area $i_f > 24$ (deg.) causes decrease in the accuracy of the simulation.

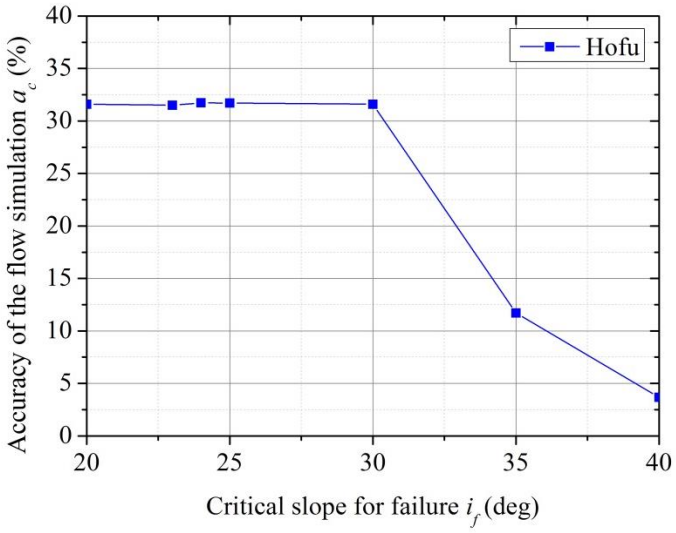

Figure 5.23 Relationship between the accuracy of the flow simulation and the critical slope angle for failure

The difference in the results found in the Rio de Janeiro's case study and in Hofu's case study is 3.9 (%).

In the previous item (5.4) we venture to find the optimal parameters for the entire region: 0.04 and 0 (deg.) for Manning coefficient and critical slope of deposition i_d, respectively. Finally, we tested the accuracy of the flow simulation with the optimal parameters. Eq. 4.1 was used to calculate the agreement between the simulated damage area A_s and the actual damage area A_a (item 4.2). Prior to analyze the accuracy, a quantitative approach was employed to find the average of accuracy of the flow simulation among the two areas.

Table 5.2 provides the results obtained from the analysis when the critical slope angle for failure are $20(\text{deg.}) \leq i_f \leq 40(\text{deg.})$. The average accuracy when $i_f = 20$ (deg) is about 31.59(%). This value falls drastically when $i_f = 40$ (deg). It can be seen in details from the Table

5.2 that the results reported when the critical slope angle for failure $i_f = 24$ (deg) revels that the best average accuracy of the flow simulation is about 31.72%. Results for the critical slope angle for failure $i_f > 24$ (deg.) present a decay in the accuracy until it reaches 3.68 % for $i_f = 40$ (deg.). For $i_f < 24$ (deg.), the accuracy also declines starting around 23 (deg.), when the accuracy is 31.50%. Overall, these results indicate a good agreement with our landslide simulation.

Table 5.2 Results of the accuracy of the flow simulation to respect critical slope angle for failure in the two areas

	A_a (m²)	A_s (m²)	$A_a \cup A_s$ (m²)	$A_a \cap A_s$ (m²)	$a_c(\%)$	$a_c(\%)$ (average)
LEFT (1), if 20	2,721,354.17	5,690,104.17	5,796,130.95	2,615,327.38	45.12195	31.59
RIGHT (2), if 20	1,095,610.12	5,831,473.21	5,866,815.48	1,060,267.86	18.07229	
LEFT (1), if 23	2,721,354.17	4,629,836.31	5,230,654.76	2,120,535.71	40.54054	31.50
RIGHT (2), if 23	1,095,610.12	4,877,232.14	4,877,232.14	1,095,610.12	22.46377	
LEFT (1), if 24	2,721,354.17	4,559,151.79	5,195,312.50	2,085,193.45	40.13605	31.72
RIGHT (2), if 24	1,095,610.12	4,700,520.83	4,700,520.83	1,095,610.12	23.30827	
LEFT (1), if 25	2,721,354.17	4,492,001.49	5,159,970.24	2,053,385.42	39.79452	31.71
RIGHT (2), if 25	1,095,610.12	4,672,247.02	4,665,178.57	1,102,678.57	23.63636	
LEFT (1), if 30	2,721,354.17	4,488,467.26	5,159,970.24	2,049,851.19	39.72603	31.60
RIGHT (2), if 30	1,095,610.12	4,665,178.57	4,665,178.57	1,095,610.12	23.48485	
LEFT (1), if 35	2,721,354.17	2,053,385.42	4,099,702.38	675,037.20	16.46552	11.71
RIGHT (2), if 35	1,095,610.12	1,701,729.91	2,615,327.38	182,012.65	6.959459	
LEFT (1), if 40	2,721,354.17	1,035,528.27	3,498,883.93	257,998.51	7.373737	3.68
RIGHT (2), if 40	1,095,610.12	4,841,889.88	5,937,500.00	0.00	0	

Taking into consideration the differences (e.g. soil type) between the two areas, we decide to analyze both areas separately to evaluate the best results independently. For Area No. 1, the accuracy of the damaged area prediction is 45.12% at maximum for i_f=20 (deg) (represents 1.8 m of the saturated soil height), while in Area No. 2 the best result found was 24.72% for i_f=30 (deg) (indicates 1.65 m of the saturated soil height). Therefore, the average between the two areas turns to 34.92%.

This case study seeks to examine the simulation result for each area. Just for illustration purposes, Figure 5.24-5.27 explore the variation of the flow simulation in cases when $i_f = 24$

(deg) , i_f = 30 (deg) and i_f = 40 (deg), with n=0.04, i_d=0 (deg), respectively for the entire area.

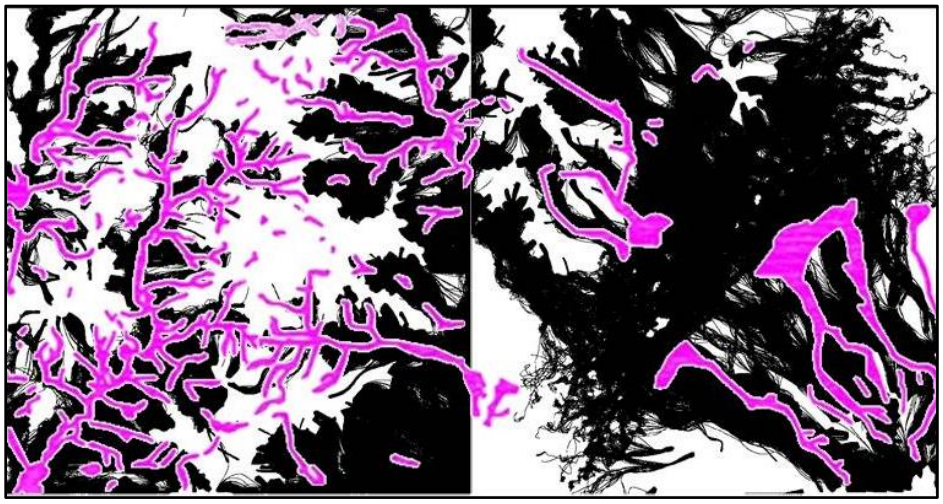

Figure 5.24 Result of the flow simulation in the entire area when if=24 (deg), id=0 and n=0.04

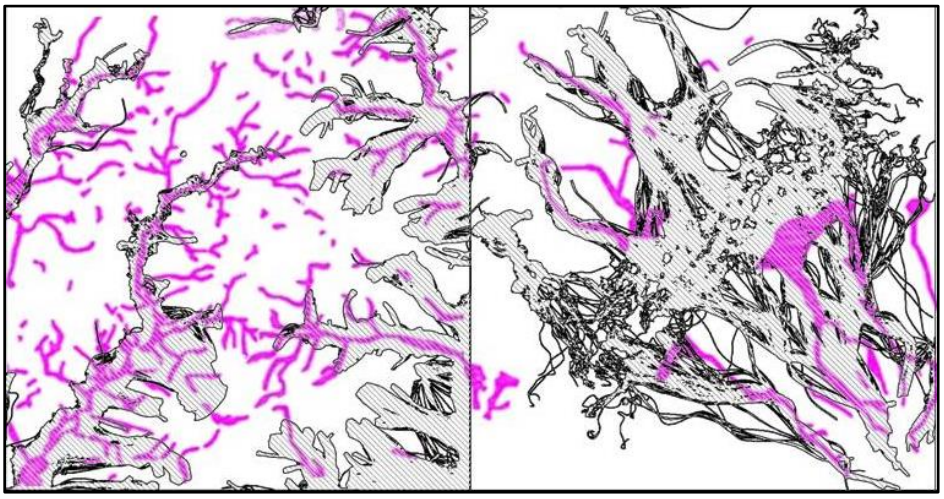

Figure 5.25 Result of the flow simulation in the entire area when if=30 (deg), id=0 and n=0.04

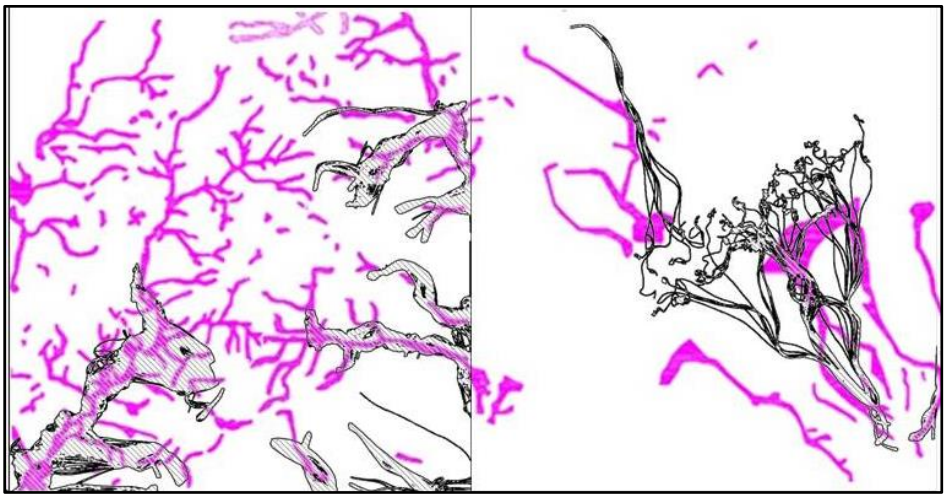

Figure 5.26 Result of the flow simulation in the entire area when if=35 (deg), id=0 and n=0.04

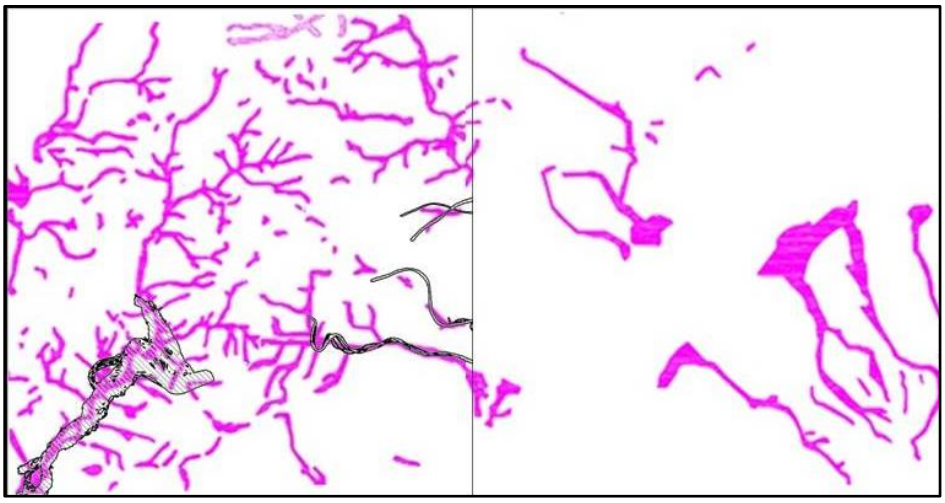

Figure 5.27 Result of the flow simulation in the entire area when if=40 (deg), id=0 and n=0.04

The actual damaged area A_a is represented by the magenta color in Figures 5.24 – 5.27. Hatched gray represents the area constructed by the flow simulation, or as we call in this research "Simulated affected area A_s". The case when i_f =40 (deg) presents an under-estimated area.

The average of the accuracy of the damaged area prediction is 31.72 (%) at maximum

when i_f =24 (deg), n==0.04, i_d=0 deg. As can be seen from the Figure 5.24, the previously set of parameters reported significantly a good balance between the intersections areas ($A_a \cap A_s$) and the simulated area A_s. The simulated affected area A_s, in black here, shows a good coverage of the areas marked in magenta (Actual damage area A_a).

In certain occasions, the key performance chosen to evaluate the efficiency of the flow simulation a_c needed a complementary analysis. Therefore, we define another key performance, called damage area ratio, which is defined as the damaged area divided by the total area. According to this new index, simulations with i_f<25 (deg) over-estimate the damage area, while simulations with i_f>30 (deg) under-estimate the damage area in Area No. 1. The same analysis was performed in Area No. 2. Under the results obtained, simulations with i_f>20 (deg) over-estimate the damage area. It turns out a tendency that the simulation over-estimates the damage, especially in low-damaged areas (Figure 5.28).

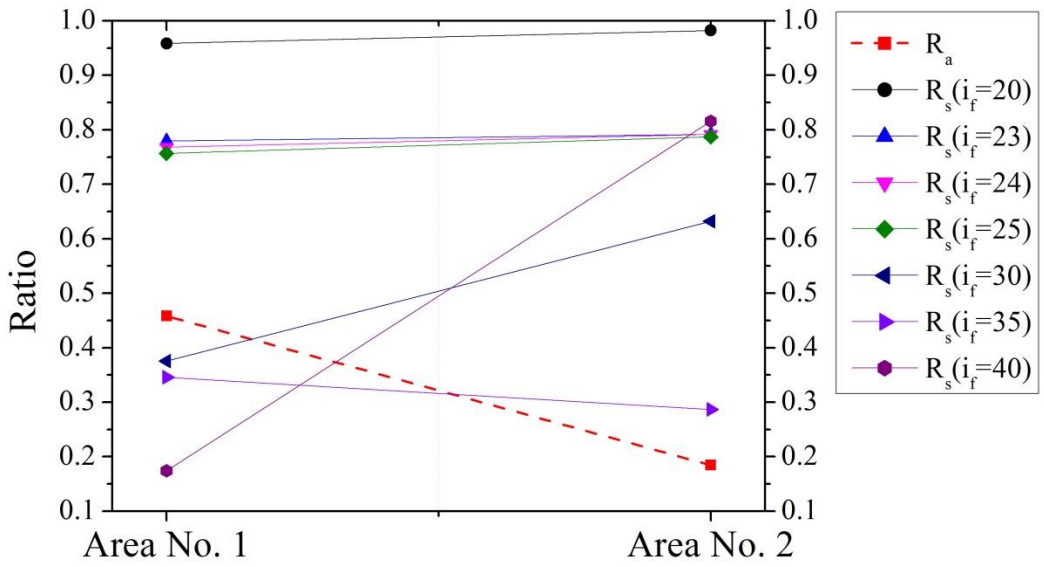

Figure 5.28 Damage area ratio for the simulation R_a for the actual damage, R_s for the simulation of damage area

6. CONCLUSIONS

Landslides happen in all over the World, however the hazard of rainfall-induced landslides likely to be much higher in tropical climate regions. The proportion of disaster varies according to the location of landslides. In Brazil, there are many residents living in mountainous area, better known as "favela". For this reason, this natural disaster is the one that most cause fatalities, representing 60% of the total in this category (Nobre, 2011). A combination of steep slopes and heavy tropical rains place populations in situations of risk.

On the basis of the evidence currently available, it seems important to have many projects related with the prediction of landslides. To do so, numerous simulation models have been proposed (e.g., Safeland project 2013). Geo-Rio foundation proposed an early warning system (d'Orsi et. al 2004) for the occurrences of landslides related to the rainfall intensities. This system performed a historical relation between landslides and precipitation of rain.

Nowadays, making use of the growing technological advance, numerical models are being used to study the behavior of landslides. To turn this simulation less complicated and makes much smaller in its computational cost, a particle method (SPH - Smooth Particles Hydrodynamics) was proposed: this method able to analyze the flow of water and sediment representing them through particles. Such an approach has been widely proposed (e.g.Pastor and Bonet).

We are the first to present the evaluation of wide-area landslide hazard using depth-integrated particle method and GIS. Hungr (1995) and Pastor et al. (2014) published the recent much-touted work on landslide simulation, however, differentiated by our research on the focus in only one side. Our study adopted mainly adopted two wide-areas as a case studies: Nova Friburgo (6,72 km by 4,5 km) and Hofu (4,75 km by 2,50 km).

Our numerical model focuses in the simplicity as many other alternative methods available: the meshless particle method proposed in our research is a simplification of the SPH (Smoothed Particle Hydrodynamics) method. The problem domain is represented by

generated particles unconnected in which interact with the neighboring particles by a pair-wise model. To avoid numerical problems such as the tensile instability, we decided not to consider the weighted average of variables that is connected to the second order derivative of the smoothing function. The reduced CPU time consummation is an important characteristic of our method. In case where the number of particles to represent the problem domain is too large it is possible to increase the grid size in order to discard some details in the topography. It could reduce CPU time and still present satisfactory results. The proposed method proved to perform suitable simultaneous simulations of landslides in wide-areas, as opposed to the many alternative depth integrated methods which considers a single landslide evaluation per time.

It is well-know that after a slope failure occurs, the flowing surface soil mass changes its state and consequently has different properties if compared to those before the failure, also these properties are very difficult to obtain by in-situ tests. In order to overcome such complexity, we perform a simple statistical analysis that was used to identify the saturation of the surface soil according to the maximum accuracy of the flow simulation given by the methodology presented in this study. To reproduce a landslide with a minimum number of parameters, it was explored three parameters: critical slope angle for failure i_f (solid fase), Manning coefficient n (flow fase) and critical slope angle of deposition i_d (flow fase).

In January 11-12th happened in Rio de Janeiro several landslides that destroyed around 10% of its mountainous region. The cause of this disaster was appointed as the intensive rainfall that happened during two days. A part of this region was chosen as a case study. After analysis of the landslide simulation method, the maximum average of the accuracy was 35.62% when the surface soil was with approximately 0.56 m saturated and the critical slope angle for failure was 32 (deg). Parameters such as Manning coefficient and critical slope angle for deposition, respectively, 0.1 and 0 (deg) were obtained by simple statistical analysis. Regarding the best value of Manning coefficient n, it corresponds to the values of water flow on the floodplains (0.07 to 0.10 for medium to dense brush and 0.15 for trees) and on the natural channels (0.060 to 0.075). Therefore, the simulated best value of n (0.1) may be reasonable.

On 2009, July 21th many debris flows and slope failures induced by torrential rain in

Hofu city, Yamaguchi Prefecture, were reported. This research focus in an area (4,75 km by 2,50 km) that is basically formed by two types of granitic rocks: granodiorite (Gd) and granite (Gr). Yamashita et al. (2013) proposed a relation between the granitic rocks and the shallow landslides in Hofu. Places with granodiorite (Gd) showed lower number of landslides with larger size, while places formed by Granite (Gr) had higher number of landslides with smaller size. After the statistical analysis to find the optimal parameters to the entire region in Hofu, we conclude the best average of the accuracy of the damaged area prediction is 31,72% for $i_f = 24$ (deg.), n=0.04 and $i_d = 0$ (deg.). Regarding the value of Manning coefficient, it is approximately the value suggested by Maeda et. al (n=0.03) and Nakatani et. al (n=0.03). The value of the critical slope of deposition is also in agreement with the disaster survey result in general., which is in accordance with the heavy rain that triggered the landslides. Overall, the adopted simulation procedure works reasonably well. Considering the differences between the two areas in Hofu and performing the analysis separately, we found the accuracy of the damage area prediction is 45,12% at maximum, while for Area No. 2 the best result found is 24.72%. Therefore, the average of the accuracy of the flow simulation is 34.92% for Hofu's case study.

The difference between the best average of the accuracy of the damaged area prediction, a_c =35,62(%) and a_c =34,92(%) for Rio de Janeiro and Yamaguchi's case studies respectively is minimum, however could be explained by seismic considerations. This hypothesis is reinforced by Hack et al. (2007) argumentation that an earthquake can make smaller the shear strength in the slope and add adverse forces to a slope.

A new key performance was introduced in this research: we called damage area ratio, which is defined as the damaged area divided by the total area. Therefore, according to this new index, simulations with i_f<25 (deg) over-estimate the damage area, while simulations with i_f>30 (deg) under-estimate the damage area in Hofu's Area No. 1. The same analysis was performed in Hofu's Area No. 2. Under the results obtained, simulations with i_f>20 (deg) over-estimate the damage area. It turns out a tendency that the simulation over-estimates the damage, especially in low-damaged areas.

Significance findings prompted us to take a wider attention to the effect of the grid size. This study has found that the maximum velocity of the flow is affected by the grid size. Grids with larger size dispense the details in the topography, which implies in a minor disturbance of the flow. The maximum velocity of the flow is an important feature to validate the proposed method: facing unrealistic results it is possible to discard some grid sizes. Also, by decreasing the grid size the percent of steeper slopes will increase.

It is apparent from this study that very few parameters resulted in a landslide simulation with a reasonable accuracy. Also, none of these values was needed to obtain by in-situ tests. Our methodology allowed us to investigate the sensibility of those parameters by using a numerical simulation. Overall, we recommend a value for Manning coefficient approximately to 0.1 in Nova Friburgo's area and 0.04 to Hofu's area. The value for critical angle of deposition i_d=0 (deg) is suggested for both areas. In fact, It was analyzed that for values $i_d < 5$ the accuracy for flow simulation does not present a significant difference. It was observed that the most sensitive parameters to the proposed simulation is the Manning Coefficient n.

What is interesting in this method is that it is easily and economically applicable in any place in the world. Such approach is extremely important to keep the evaluation of the accuracy of this simulation method and explore ways for the accuracy becomes higher.

7. APPENDIX

1) Satellite image parameters for Nova Friburgo

Details provided by the Japan Aerospace Exploration Agency (JAXA), when choosing the study area showed in this research acquired by ALOS satellite and PRISM sensor.

Table 7.1 Details for the satellite image in Nova Friburgo

	Generation Date and Time	2011-01-22T17:35:20Z
Scene Four Corners	UpperLeft Longitude	-42.775217043
	UpperLeft Latitude	-21.939514165
	UpperRight Longitude	-42.347106350
	UpperRight Latitude	-21.933158870
	LowerLeft Longitude	-42.768938972
	LowerLeft Latitude	-22.338441649
	LowerRight Longitude	-42.339623390
	LowerRight Latitude	-22.331958743
	Scene Center Longitude	-42.557721385
	Scene Center Latitude	-22.135911591
Map Projection:	Ellipsoid	WGS84(6378137.000000,6356752.314200,0.000000,0.000000,0.000000)
	Datum	WGS84
	Map	UTM
	Zone	23
PRISM Image Data	Pixels	17701
	Lines	17677
	Channel/File	1
	Pixel Spacing Size X (m)	2.5
	Pixel Spacing Size Y (m)	2.5
	Data Type	8-bit unsigned integer
Source Data Information	Platform Name	ALOS
	Sensor Name	PRISM
	Source Data ID	ALPSMN242504045
	Scene ID	D38340450
	Observation Date and Time	20100813 13:06:04.02

	Image Compression Rate	1/4.5
	Orbit Data Precision	Precision
	Attitude Data Precision	OnSitePrecision
	Gain Mode	2
	Radiance Conversion Coefficient Gain	0.501000
	Radiance Conversion Coefficient Offset	0.000000
	Pointing Angle	-1.4000
	Sun Angle Elevation	44.59
	Sun Angle Azimuth	38.49

2) Satellite image parameters for Hofu

Details provided by the Japan Aerospace Exploration Agency (JAXA), when choosing the study area showed in this research acquired by ALOS satellite and PRISM sensor.

Table 7.2 Details for the Satellite image for Hofu

	Generation Date and Time	2009-09-18T17:24:13Z
Scene Four Corners	UpperLeft Longitude	131.426495594
	UpperLeft Latitude	34.277035018
	UpperRight Longitude	131.898078437
	UpperRight Latitude	34.266783665
	LowerLeft Longitude	131.414951709
	LowerLeft Latitude	33.871461726
	LowerRight Longitude	131.884298011
	LowerRight Latitude	33.861364645
	Scene Center Longitude	131.655953794
	Scene Center Latitude	34.069389917
Map Projection:	Ellipsoid	WGS84(6378137.000000,6356752.314200,0.000000,0.000000,0.000000)
	Datum	WGS84
	Map	UTM
	Zone	52
PRI SM	Pixels	17384
	Lines	18005

	Channel/File	1
	Pixel Spacing Size X (m)	2.5
	Pixel Spacing Size Y (m)	2.5
	Data Type	8-bit unsigned integer
Source Data Information	Platform Name	ALOS
	Sensor Name	PRISM
	Source Data ID	ALPSMN180442915
	Scene ID	D08229150
	Observation Date and Time	20090614 02:05:53.46
	Image Compression Rate	1/4.5
	Orbit Data Precision	Precision
	Attitude Data Precision	OnSitePrecision
	Gain Mode	2
	Radiance Conversion Coefficient Gain	0.501000
	Radiance Conversion Coefficient Offset	0.000000
	Pointing Angle	-1.4000
	Sun Angle Elevation	71.68
	Sun Angle Azimuth	121.68

3) Other results

The standard approach to this Chapter is to present and describe the results for other areas that could not be inserted in the wide-area scope (e.g. Ilha Grande). Also, we would like to show alternative tentative of evaluation of Hofu's case study.

a) Ilha Grande

Ilha Grande is located about 150km from the capital of Rio de Janeiro. Ilha Grande suffered with intense rainfall that triggered landslides on the last day of 2009.

It was found that the maximum average of the accuracy of the damage area prediction is 48% for the set parameters (i_f, n, i_d), 23 (deg.), 0.1 and 0 (deg.), respectively.

Table 7.3 Mechanical Parameters

Parameters	Values
Manning Coefficient	0.1
Specific Gravity	2.650g/cm^3
Cohesion	6kPa
Friction Angle	42 (deg.)

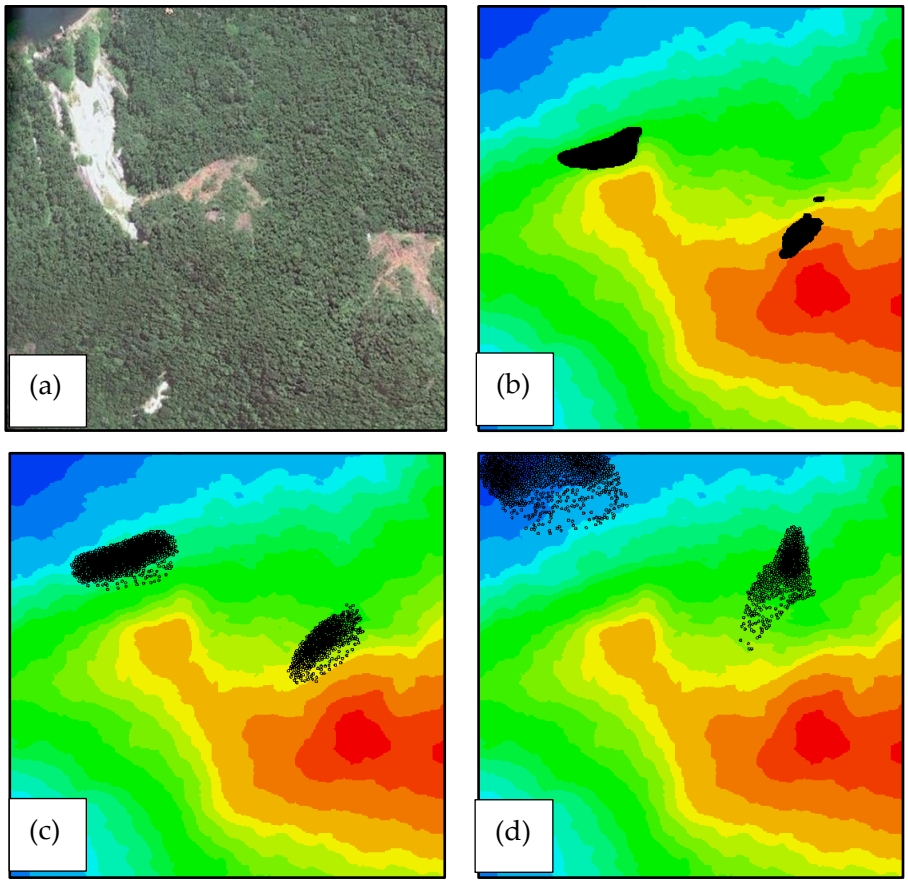

Fig. 7.1 Research area in Ilha Grande, (a) Actual damaged area, (b) Initial particle position, (c) Particles in motion, (d) Particles in motion

b) Hofu city

b.1) 64 small areas (1,25 km by 1,25 km each)

We applied the procedure to the wide area (10km by 10km) in Hofu city, Japan, which was severely damaged due to rainfall-induced landslides in 2009. Initially, we had divided the entire area affected in Hofu city in 64 small areas (Figure 7.2). Each area had 1,25 km of width by 1,25 km of length. Full parametric study shows that the average of the accuracy of the damaged area prediction is 11,83% at maximum, when $i_f = 28$ (deg.), n=0.04, i_d =0 (deg.). The initial particle spacing d_0 utilized in the interparticle pressure model used in this study (item 3.3) is set to the grid size of the DEM obtained from PRISM image, which is 5.0 meters.

The simulations were performed according to the procedure described beforehand. What is interesting in this data is that although apparently the simulations results are not quite out of context (Figure 7.3), the best average of the accuracy of the damaged area prediction is far from the 51% achieved in Rio de Janeiro's case study.

This is a consequence of the size chosen for the small areas, where the particles are not allowed to run out on their paths due to the small domain established. In the Figure 7.3, it is possible to visualize in Area No.22 an interruption of the flow simulation, which cannot be evaluated in Area No.30. Therefore, we decided to perform the simulation in a larger domain area (Chapter 5).

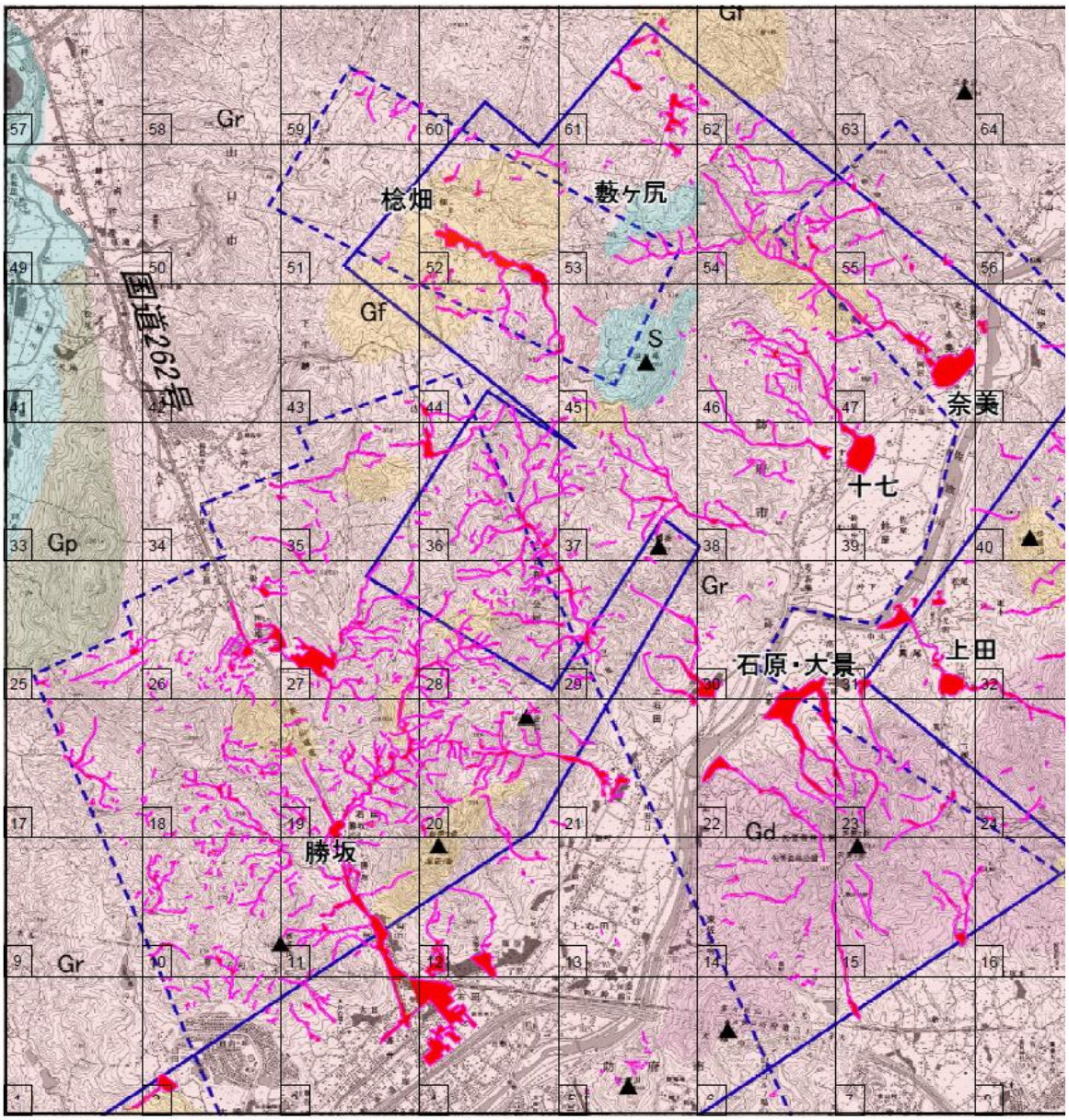

Fig. 7.2 Research area after the disaster. The grids show the discretized domain for flow simulation

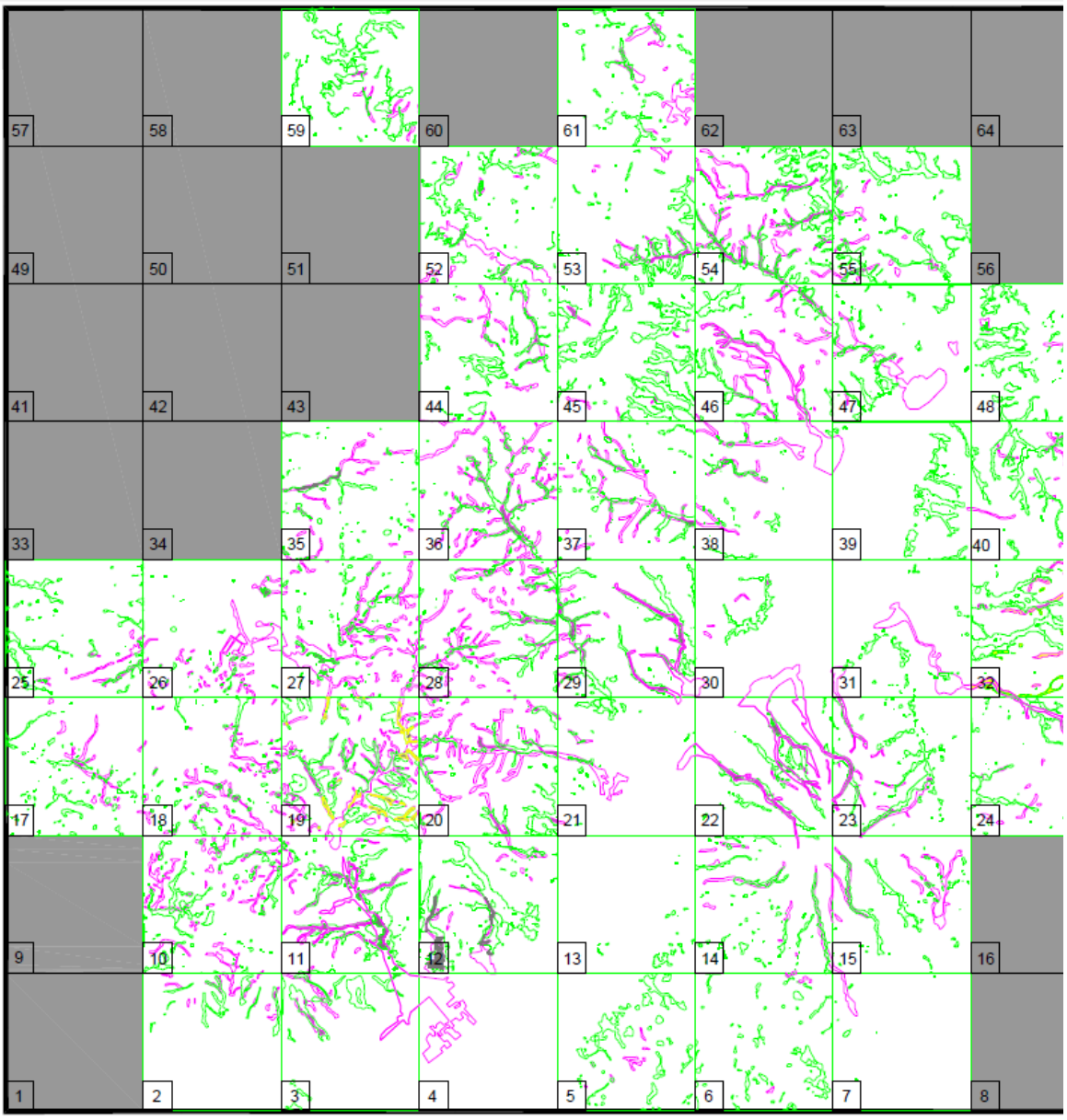

Fig. 7.3 Traces in green represent the simulated affected area. Traces in magenta represent the actual damaged area

b.2) Statement of the Study of Parameters in Hofu city

As mentioned in Chapter 5, a study of the sensibility of parameters were performed to

evaluate the simulation according to the best accuracy of the flow obtained. The results in numbers can be found in Table 7.4.

Table 7.4 Result of the analysis of the parameters in Hofu

Area	n	id	Aa (m²)	As (m²)	Aa U As (m²)	Aa ∩ As (m²)	Ac (%)	Ac Total
No. 1	0	0	2,721,354.17	3,569,568.45	4,523,809.52	1,767,113.10	39.0625	27.63935811
No. 2	0	0	1,095,610.12	4,983,258.93	5,230,654.76	848,214.29	16.21622	
No. 1	0	5	2,721,354.17	2,191,220.24	3,746,279.76	1,166,294.64	31.13208	22.91897891
No. 2	0	5	1,095,610.12	3,039,434.52	3,604,910.71	530,133.93	14.70588	
No. 1	0	10	2,721,354.17	1,378,348.21	3,251,488.10	848,214.29	26.08696	24.40711462
No. 2	0	10	1,095,610.12	812,872.02	1,555,059.52	353,422.62	22.72727	
No. 1	0.04	0	2,721,354.17	4,488,467.26	5,159,970.24	2,049,851.19	39.72603	31.60543794
No. 2	0.04	0	1,095,610.12	4,665,178.57	4,665,178.57	1,095,610.12	23.48485	
No. 1	0.04	5	2,721,354.17	1,943,824.40	3,604,910.71	1,060,267.86	29.41176	26.31302521
No. 2	0.04	5	1,095,610.12	1,343,005.95	1,979,166.67	459,449.40	23.21429	
No. 1	0.04	10	2,721,354.17	1,378,348.21	3,428,199.40	671,502.98	19.58763	15.74619539
No. 2	0.04	10	1,095,610.12	565,476.19	1,484,375.00	176,711.31	11.90476	
No. 1	0.08	0	2,721,354.17	459,449.40	2,403,273.81	777,529.76	32.35294	26.55382908
No. 2	0.08	0	1,095,610.12	1,166,294.64	1,873,139.88	388,764.88	20.75472	
No. 1	0.08	5	2,721,354.17	212,053.57	2,579,985.12	353,422.62	13.69863	11.19714116
No. 2	0.08	5	1,095,610.12	671,502.98	1,625,744.05	141,369.05	8.695652	
No. 1	0.08	10	2,650,669.64	671,502.98	3,074,776.79	247,395.83	8.045977	7.681525091
No. 2	0.08	10	1,095,610.12	459,449.40	1,449,032.74	106,026.79	7.317073	
No. 1	0.12	0	2,721,354.17	1,307,663.69	3,569,568.45	459,449.40	12.87129	10.88008801
No. 2	0.12	0	1,095,610.12	636,160.71	1,590,401.79	141,369.05	8.888889	
No. 1	0.12	5	2,721,354.17	848,214.29	3,357,514.88	212,053.57	6.315789	6.729323308
No. 2	0.12	5	1,095,610.12	494,791.67	1,484,375.00	106,026.79	7.142857	
No. 1	0.12	10	2,721,354.17	636,160.71	3,145,461.31	212,053.57	6.741573	5.934889081
No. 2	0.12	10	1,095,610.12	353,422.62	1,378,348.21	70,684.52	5.128205	

Samples of the simulation for n=0.0 constant and i_d=(0, 5, 10) degrees.

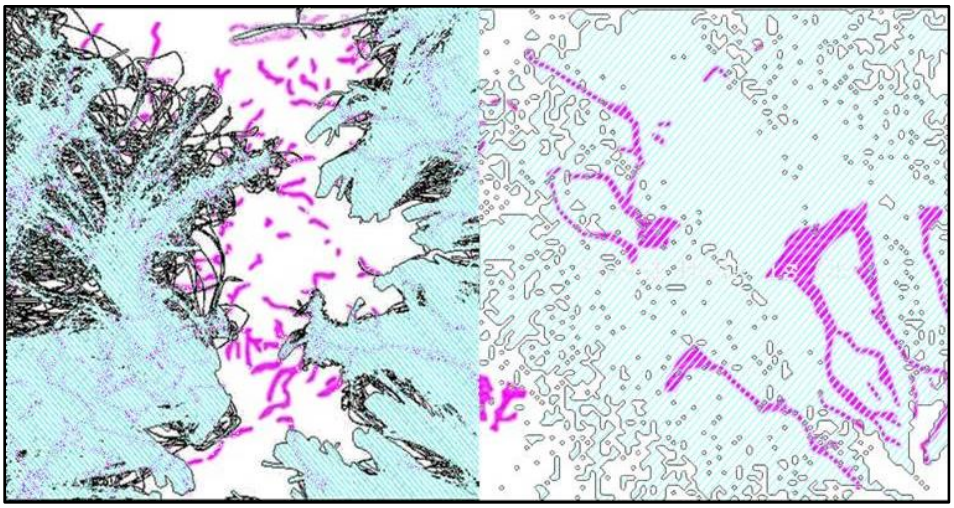

Fig. 7.4 Simulation result for i_f=30 (deg), n=0.0, i_d=0 (deg)

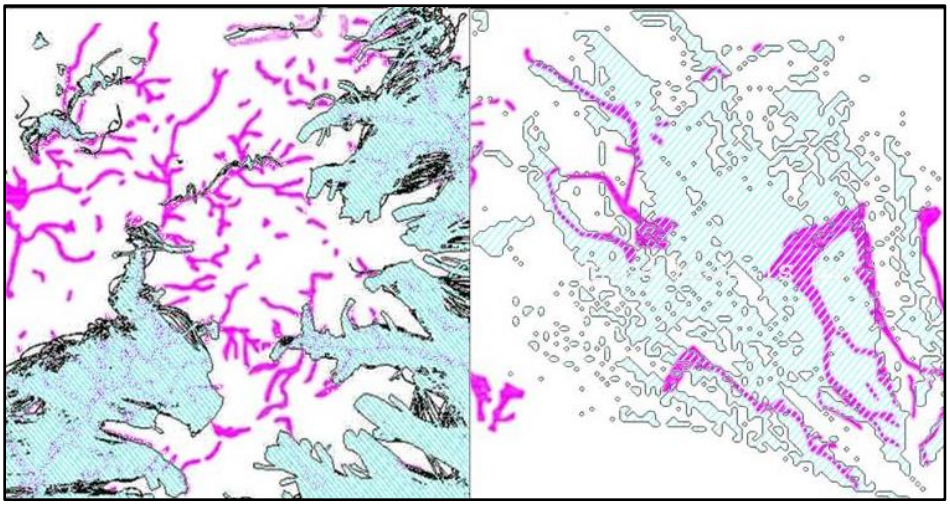

Fig. 7.5 Simulation result for i_f=30 (deg), n=0.0, i_d=5 (deg)

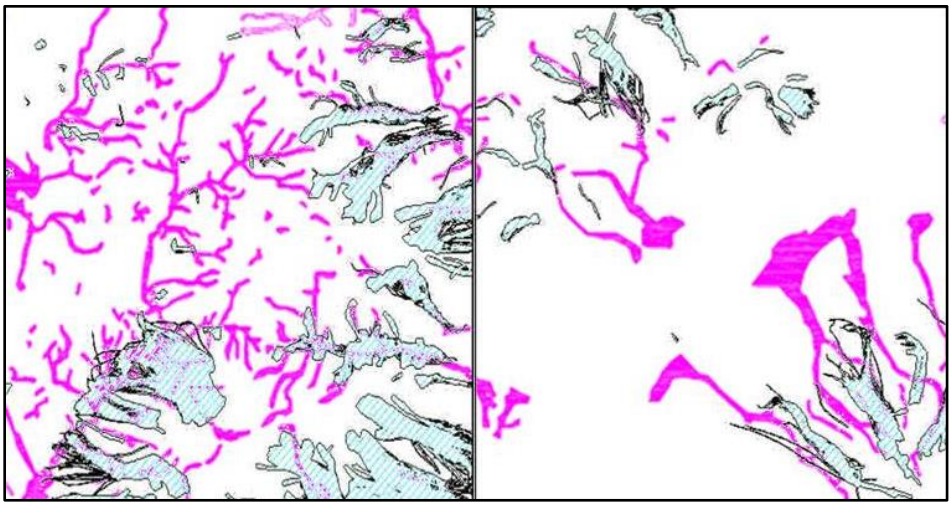

Fig. 7.6 Simulation result for i_f=30 (deg), n=0.0, i_d=10 (deg)

8. REFERENCES

1) ALOS project, Advanced Land Observing Satellite, http://www.jaxa.jp/projects/sat/alos/index_e.html, 2011.
2) Avelar, A. S. & Netto, A. L. C & Lacerda, W. A. & Becker, L. B. & Mendonça, M. B. :Mechanisms of the recent catastrophic landslides in the mountainous range of Rio de Janeiro, Brazil, Rome, The second world landslide forum, 2011.
3) Barnes H (1967) Roughness characteristics of natural channels. Technical report, USGS Water Supply Paper
4) BBC, BBC news, http://news.bbc.co.uk
5) Belytscko, T., Krongauz, Y., Organ, D., Fleming, M., Krysl, P., Meshless methods: An overview and recent developments, 1996
6) Blanc, T., Numerical simulation of debris flows with the 2D-SPH depth integrated model, 2008.
7) Brabb, E., Proposal for worldwide landslide hazard maps. 1993. Proceedings of 7th International Conference and field workshop on landslide in Czech and Slovak Republics; pp. 15–27.
8) Braja, M. D., Fundamentals of geotechnical engineering, ISBN 0534371140, 1999.
9) Calvello, M., d'Orsi, R. N., Piciullo, L., Paes, N., Magalhaes, M., Lacerda, W. A.: The Rio de Janeiro early warning system for rainfall-induced landslides: Analysis of permormance for the years 2010-2013, International Journal of disaster risk reduction, 2014.
10) CEPED UFSC, Atlas brasileiro de desastres naturais 1991 a 2010, volume Rio de Janeiro, 2011 (in Portuguese)
11) Chen, C. Y., Fujita, M., Tsutsumi, D., A study on mechanism of large-scale landslides and the prediction, Annuals of Disas. Prev. Res. Inst., Kyoto University, No. 56 B, 2013
12) Chow VT (1959) Open channel hydraulics. McGrawHill, New York.
13) Cleary, P. W., Ha, J., Modelling the high pressure die casting process using SPH

14) Clover, T. J., Pocket reference, Littleton, Colorado, Sequoia Publishing, Inc 1998.
15) Coelho, A. L. N, Sato, A. M., Avelar, A. S., Vianna, L. G. G., Araujo, I. S., Ferreira, D. L. C., Lima, P. H., Silva, A. P. A., Silva, R. P.: January 2011: the extreme landslide disaster in Brazil, Proceedings of the Second World Landslide Forum, Rome, 2011.
16) CRDB, Chugoku Regional Development Bureau, Yamaguchi Branch www.cgr.mlit.go.jp/yamaguchi.
17) CRISP, Centre for Remote Imaging, Sensing and Processing, Digital Image Chapter
18) d'Orsi, R. N., Feijo, R. L., Paes, N. M., 2,500 Operational Days of Alerta Rio System: History and Technical Improvements of Rio de Janeiro Warning System for Severe Weather
19) DRM-RJ, Departamento de recursos minerais, Servico geologico do estado do Rio de Janeiro, Megadesastres da Serra JAN 2011
20) e.g., Takahashi, T., Mechnism and countermeasure of debris flow, Kin-mirai-sha, pp. 432, 2004 (in Japanese)
21) Fernandes, N. F., Guimaraes, R. F., Gomes, R. A. T., Vieira, B. C., Montgomery, D. R., Greenberg, H., Topographic controls of landslides in Rio de Janeiro: field evidence and modeling, Catena 55, 2004, pp.163-181.
22) Gingold, R. A., Monaghan, J. J., Smoothed particle hydrodynamics: theory and application to non-spherical stars, Monthly notices of the royal astronomical society, 181, 375-389, 1977.
23) Hack, R., Alkema, D., Kruse, G. A. M., Leenders, N., Luzi, L., Influence of earthquakes on the stability of slopes, Engineering Geology 91, 2007, pp. 4-15
24) Hagen, T. R., Hjelmevik, J. M., Lie, K. A., Natvig, J. R, Ofstad Henriksen, M., Visual Simulation of Shallow water waves, SINTEF ICT, Applied Math, 2005
25) Hoang, G.Q. & Matsushima, T & Yamada, Y. :Debris flow simulation by particle method using PRISM-DSM, Proc. Geo-Kanto (in Japanese), 2009.
26) Hungr, O., A model for the runout analysis of rapid flow slides, debris flows, and avalanches, Canadian Geotechnical Journal, 1995, pp. 610-623
27) INMET, Instituto Nacional de Meteorologia, http://www.inmet.gov.br (in Portuguese).

28) Ishihara, Y., Kobatake, S., Runoff Model for Flood Forecasting, Bull. Disas. Prev. Res. Inst., Kyoto Univ., Vol. 29, Part 1, No260, July, 1979
29) Iwamoto, T., Slope stability evaluation using a wide-area ground database, Master Thesis, University of Tsukuba, 2011 (in Japanese).
30) Japan Society of Civil Engineers, China Branch, July 2013 Yamaguchi: Heavy rain disaster investigative report, 2013 (in japanese).
31) Japan Society of Civil Engineers, July 2009 Heavy rain disaster survey report in Yamaguchi, Geotechnical Engineering Committee, 2009 (in Japanese).
32) Jenson, S. K., Applications of hydrologic information automatically extracted from digital elevation models, Hydrol. Process., 5(1), pp.31-44, 1991
33) Kaiami, J., Erosion of river, terrain fluctuation due to sedimentation: model experiments and numerical analysis concerning, University of Tsukuba, Master thesis, 2011 (in Japanese).
34) King, M. D., Platnick, S., Menzel, W. P., Ackerman, S. A., Hubanks, P. A., Spatial and Temporal distribution of clouds observed by MODIS onboard the Terra and Aqua satellites, Geoscience and Remote Sensing, IEEE Transactions on, Vol. 51, Issue 7, pp.3826-3852, 2013
35) Lambe, T. W., Whitman, R. V., Soil Mechanics, SI version, Massachusetts Institute of Technology.
36) Liu, G. R., Gu, Y. T, An introduction to meshfree methods and their programming, Springer, ISBN 10-1-4020-3228-5
37) Liu, G. R., Liu, M. B., Smoothed particle hydrodynamics: a meshfree particle method, World Scientific, ISBN 3-540-22256-1
38) Lucy, L. B., A numerical approach to the testing of the fission hypothesis, The astronomical journal, volume 82, number 12, 1977; pp. 1013-1024
39) MCTI, Ministerio da Ciencia, Tecnologia e Inovacao, Nobre, 2011, http://www.mct.gov.br (in Portuguese)
40) Misumi, R., Meteorological situations of the Yamaguchi Heavy Rainfall on 21 July2009 – local front and orographic effects. Natural Disaster Research Report of the National

Research Institute for Earth Science and Disaster Prevention, 44, 1–9. (in Japanese with English abstract), 2010.

41) Monaghan, J. J., Simulating free surface flow with SPH, Journal of computational physics, volume 110, Issue 2, 1994; pp.399-406

42) Morris, J. P., Fox, P. J., Zhu, Y., Modeling low Reynolds number incompressible flows using SPH, Journal of Computational Physics, 136, 214-226, 1997.

43) Nakata, A.M., Matsushima, T., Evaluation of the landslide simulation's efficiency in Rio de Janeiro's case study, Proceedings of The Twenty-seventh KKHTCNN Symposium on Civil Engineering, 2014, Shanghai.

44) Nakata, A.M., Matsushima, T., Evaluation of wide-area landslide damage by depth-integrated particle method, submitted to Landslides, 2015

45) Nakata, A.M., Matsushima, T., Landslide simulation based on particle method: toward statistical risk evaluation, Proceedings of The 1st International Conference on Computational Engineering and Science for Safety and Environmental Problems, 2014, pp. 397-399

46) Nakata, A.M., Matsushima, T., Statistical evaluation of damage area due to heavy-rain-induced landslide, Computer Methods and Recent Advances in Geomechanics (IACMAG), Oka, Murakami, Uzuoka & Kimoto Eds., Taylor and Francis, 1523-1528, 2014.

47) OGLOBO, O Globo, http://oglobo.oglobo.com (in Portuguese)

48) Osanai, N., Shimizu, T., Kuramoto, K., Kojima, S., Noro, Japanese early-warning for debris flows and slope failures using rainfall índices with radial basis function network, Landslides, doi 10.1007/s10346-010-0229-5, 2010

49) Panuska, J. C., Moore, I. D., Kramer, L. A., Terrain analysis: Integration into the agriculture nonpoint source (AGNPS) pollution model, J. Soil Water Conservation, 46(1), pp.59-46, 1991

50) Pastor, M., Blanc, T., Haddad, B., Petrone, S., M, S. M., Drempetic, V., Issler, D., Crosta, G. B., Cascini, L., Sorbino, G., Cuomo, S., Application of a SPH depth-integrated model

to landslide run-out analysis, Landslides, doi 10.1007/s10346-014-0484-y, 2014

51) Roy, A., Ahmad, M. A., Sarkar, C., Keegan, B., Srivastava, J., The ones that got away: false negative estimation based approaches for gold farmer detection, IEEE, ISBN 978-1-4673-5638-1, pp. 328-337.

52) Safeland project report 2013, http://www.safeland-fp7.eu/

53) Sanchez, M. E., Pastor, M., Romana, M. G., Modelling of short runout propagation ;andslides and debris flow

54) Sekiguchi, S., Tanaka, Y., Kojima, I., Geo Grid: Federating Geospatial Data and Integrating Services, National Institute of Advanced Industrial Science and Technology, www.geogrid.org

55) Slater JC(1934), Electronic Energy Bands in Metals. Phys. Rev. 45, 794-801.

56) Teixeira, Toledo, Fairchild and Taioli, Decifrando a terra, Sao Paulo, Oficina de textos, 2000 (in Portuguese)

57) The Geospatial Information Authority of Japan (GIS), www.gsi.go.jp

58) The Japan Landslide Society, https://japan.landslide-soc.org/overview_index.html?lang=en

59) UNU, The newsletter of United Nations University and its international newtwork of research and training centres/programmes, Issue 40: November 2005- February 2006

60) USGS archives of landslide events, http://landslides.usgs.gov/recent/

61) Wakatsuki, T., Ishizawa, T., Uetake, M, Kawada, S., Characteristics of Debris Flow and Slope Failure on Granite Slopes Caused by Heavu Rainfall on July 2009 in Hofu and Yamaguchi Cities, Japan, 2010

62) Weiyan, T., Shallow water hydrodynamics, Mathematical theory and numerical solution for a two-dimensional system of shallow water equations, Elsevier Oceanography Series, 55, ISBN 0-444-55625-7

63) Yamashita, K., Condition of shallow landslides on granitic mountains in Hofu city, Yamaguchi Prefecture, Japan: A case study of debris flow disaster in 2009, Master thesis (in Japanese), 2013.

64) Yamashita, K., Stability analysis of slopes by granite and granodiorite in Hofu city, Yamaguchi Prefecture, Japan, Dissertation (in Japanese), 2011.

65) Yasuda, S., Yamada, Y., Katada, T., Soil Mechanics, ISBN 9784274216435 (in Japanese)

66) Zhang, N., Matsushima, T., Yamada, Y., Efficient numerical simulation of debris flow with erosion and sedimentation, Computer Methods and Recent Advances in Geomechanics (IACMAG), Oka, Murakami, Uzuoka & Kimoto Eds., Taylor and Francis, 1529-1534, 2014.

67) Zhang, N., Quantitative evaluation of debris flow hazard using depth-integrated particle method and satellite image, Doctor thesis, University of Tsukuba, 2015.

68) Zhang, W., Montgomery, D. R., Digital elevation model grid size, landscape representation, and hydrologic simulations, Water resources research, Vol. 30, No.4, pp. 1019-1028, 1994

9. PUBLICATIONS

[1]. Alessandra Mayumi Nakata, Takashi Matsushima: *Landslide simulation based on particle method: toward statistical risk evaluation,* Proceedings of The 1st International Conference on Computational Engineering and Science for Safety and Environmental Problems, 2014, pp. 397-399

[2]. Alessandra Mayumi Nakata, Takashi Matsushima: *Statistical evaluation of damage area due to heavy-rain induced landslide,* Computer Methods and Recent Advances in Geomechanics, 2014, pp. 1523-1528

[3]. Alessandra Mayumi Nakata, Takashi Matsushima: *Evaluation of the landslide simulation's efficiency in Rio de Janeiro's case study*, Proceedings of The Twenty-seventh KKHTCNN Symposium on Civil Engineering, 2014, Shanghai.

10. CONFERENCE PARTICIPATION

[1] Nakata Alessandra Mayumi, Takashi Matsushima: Comparison between landslide simulations from fully saturated to a completely dry condition, Tsukuba Global Science Week, Poster Presentation, 2014

[2] Nakata Alessandra Mayumi, Takashi Matsushima: Estimating the degree of saturation of the soil in a landslide simulation model in a tropical climate case study, JSCE Applied Mechanics Symposium, Kanazawa city, 2015

[3] Nakata Alessandra Mayumi, Takashi Matsushima: Estimate the importance of considering the degree of saturation of the soil in a landslide simulation model, Tsukuba Global Science Week, Poster Presentation, 2015